A STUDY OF SURFACE ROUGHNESS ISSUES IN MAGNETIC TUNNEL JUNCTIONS

HU JIANGFENG

(M.E, B.E, XI'AN JIAOTONG UNIV.)

A DISSERTATION SUBMITTED

FOR THE DEGREE OF PHILOSOPHY

DEPARTMENT OF ELECTRICAL AND COMPUTER ENGINEERING

NATIONAL UNIVERSITY OF SINGAPORE

2004

Acknowledgements

I would like to express my gratitude to my supervisors, Dr. Vivian, Prof. Chong Tow Chong and A/P Wang Jianping, for their invaluable guidance and support throughout all my research work done there. Their carefulness and enthusiasm towards research have inspired me greatly.

I am extremely grateful to Prof. Chong Tow Chong and Data Storage Institute for giving me financial support in the last few months.

I would like to express my thanks to Dr. Adekunle (NUS), A/P Wu Yihong (NUS), Dr. Han Guchang (DSI), and Dr. Qiu Jianjun (DSI) for their help on my research works.

Most of the experiments in this dissertation were done at the Information Storage Materials Lab (ISML), Microelectronics Lab and DSI. I am grateful to people in these labs who gave me access to their facilities and help. I especially thank the research engineers and lab technicians like Liu Ling and Fong Ling.

My thanks also goes to: All the other staff and fellow scholars of ISML and the Media and Materials Group (DSI), who have helped me in one way or another.

I also would like to thank National University of Singapore for the financial support of a scholarship.

Last but not least, I am especially grateful to my family for their encouragement, utmost carefulness and support.

Contents

Summary

Magnetic tunnel junction elements are considered a likely candidate for the next generation read head in hard disk drivers and the basic element of magnetic random access memories. The spin-dependent tunneling phenomenon in magnetic tunnel junction elements is investigated theoretically and experimentally in this dissertation.

Theory:

Based on the free-electron model, the TMR and the exchange coupling as the function of several parameters such as thickness of the tunnel barrier, thickness of the FM layers, spin polarization of two FM layers, Fermi wave vectors of two FM layers and interfacial roughness, in a ferromagnet/insulator/ferromagnet tunnel junction were investigated. For MTJ stacks with finite thickness of FM layers, both TMR and the exchange coupling oscillate periodically with the thickness of ferromagnetic layers. The TMR and the exchange coupling were correlated to each other and the maximum TMR occurred when ferromagnetic exchange coupling between two ferromagnetic layers reached the maximum value. Compared with the structure with perfect interface roughness, TMR ratio decreased and the exchange coupling increased as the interface roughness was introduced. The rough interface may introduce spin-flip scattering, therefore some of the majority electrons will change their spin direction and tunnel into the corresponding minority states. This causes a decay in the distribution asymmetry of density of states, resulting in a decrease of the TMR ratio. The increase of the exchange coupling may be attributed to the interfacial roughness induced exchange coupling between two FM layers via the insulator spacer. It is also found that the oscillation period of the TMR and the exchange coupling are changed after the introduction of the interfacial roughness. The difference of the oscillation

period of the TMR and the exchange coupling is attributed to the variation of the Fermi wave vectors induced by the interfacial scattering of the electrons.

Experimental:

The experimental work involved the investigation of the effects of experimental parameters (dc sputter power, film thickness and rf substrate bias) on the surface roughness and magnetic properties of $Ni_{80}Fe_{20}$ thin films. We found that the surface roughness of the thin films depended weakly on dc sputter power and film thickness, however, it could be well controlled by applying an rf substrate bias during the deposition. The average roughness and the coercivity were found to first increase and then decrease with increasing rf bias power. The rf bias induced surface roughness also has great influence on magnetic properties of Co films deposited on the rough surface, as well as, the switching properties of the entire magnetic tunnel junction stacks.

The magnetic tunnel junctions were fabricated by using a shadow mask technique. A two-stage, deposition/oxidation/deposition/oxidation, process for barrier layer formation was used in our studies. The effects of oxidation time and the Al metal deposition gas pressure on barrier layer properties and the electrical and magnetic performance of magnetic tunnel junction elements have been studied. We found that the barrier properties depended greatly on the oxidation time and the microstructure of the as-deposited Al thin film before oxidation. Magnetic tunnel junction elements with low junction resistance can be achieved by lowering the effective barrier height of tunnel barrier via controlling the microstructure of the as deposited Al thin films for barrier formation.

List of Figures

List of Table

Chapter 1

Introduction

1.1 Introduction

Magnetic thin films are commonly used in information storage and field sensors applications.[1] Generally, these applications are based on the large-scale magnetization arising from the collective behavior of electron spins. In most studies, spin transport differences of the electrons are neglected and both spin-up and spin-down electrons are expected to have identical behavior. However, recently the possibility of a new application, where the electric transport properties and the magnetic properties are affected by controlling the electronic spin, has become a reality. In magnetic metals, because of the exchange splitting effect, the density of states of spin-up and spin-down electrons are different near the Fermi surface. Thus the number of spin-up electrons is different from that of the spin-down electrons in the transport process. Furthermore, the scattering probability of spin-up and spin-down electrons during the transport is different. We expect the electron transport properties to be controlled by using these differences. During the past few years, electronics and magnetism have been converged towards a new field known as magneto-electronics, or spin-electronics, which focuses on making new devices, where both the spin and the charge of the electron play an active role.[2-4]

The era of spin electronics began with the discovery of the giant magnetoresistance (GMR) effect in 1998.[5,6] GMR effect arises from the change in resistance due to the change in relative orientations of adjacent magnetic thin-film layers.

It is found that the resistance of the magnetic multilayer is low when the magnetizations of all the magnetic layers are parallel but it becomes much higher when the magnetizations of the neighbouring magnetic layers are ordered antiparallel. The relative change of the resistance can be larger than 200%, and that is the reason why the effect is called GMR. The discovery of the GMR has created great excitement since the effect has important applications in magnetic data storage technology. Information is stored on a magnetic disk in the form of small magnetized regions (domains) arranged in concentric tracks. A conventional induction coil reading head senses the rate of change of the magnetic field as the disk rotates. The signal and the density of magnetized bits are thus limited by the rotation speed of the disk. Magnetoresistive sensors based on GMR effect do not suffer from this defect since they sense the strength of the field rather than its rate of change. Therefore, they are capable of reading disks with a much higher density of magnetic bits. Recently, the spin-valve (SV) GMR reading head was introduced for the current 30 Gbit/in^2 areal density used in commercial HDDs. Here the MR ratio is about 10%.

Although GMR sensors have achieved great success in magnetic data storage industry, one major limitation of GMR sensors is that high magnetoresistance has been obtained only in systems that require a high saturation field. That is to say, devices with high GMR often have the same sensitivity as devices with lower GMR and lower saturation fields. GMR read heads have been demonstrated with a room temperature MR of around 25% in low magnetic fields. As the magnetic recording density is closely related to the MR of the read sensors, it is obvious that either enhancing the MR of GMR sensor or using a new generation of sensors with higher sensitivity is required as the

magnetic recording density reaches the upper limit of the current GMR sensors. Read-Rite Corporation announced the achievement of a new areal density of 130 Gbit/in^2 on April 29, 2002.[7] It is very difficult to increase the MR ratio of an SV reading head to read out the recorded information from those extremely small recording areas. One alternate technology is the tunneling magnetoresistance (TMR) effect, discovered in magnetic tunnel junctions (MTJs). The difference between the GMR sensor and MTJs is that the resistance in GMR is based on the spin-dependent scattering effect, while in MTJs is based on the spin-dependent tunneling across a thin tunnel barrier. The basic structure of the MTJ has two ferromagnetic (FM) layers separated by a thin insulator layer (as shown in Fig. 1.1).

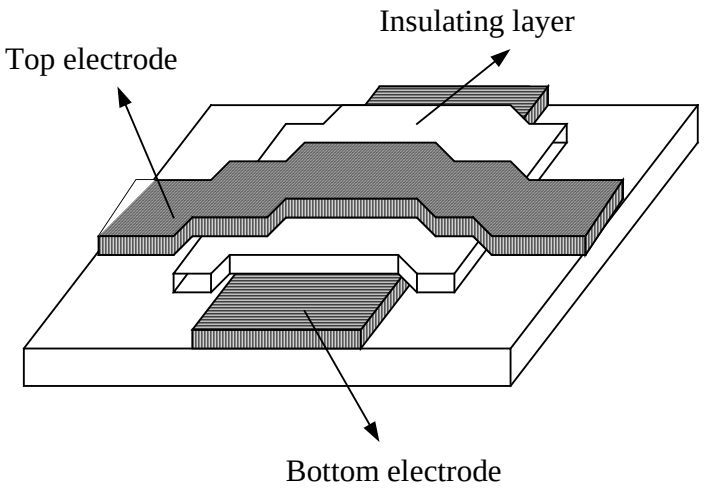

Figure 1.1 Basic structure of magnetic tunnel junction.

In 1975, Jullière[8] first demonstrated the spin-dependent tunneling on a Fe/Ge/Co junction. It was found that the spin-dependent tunneling probability in MTJs depends on the relative orientation of magnetization vectors in the two FM electrodes. For a parallel configuration, there is a maximum match between the number of the occupied states in one electrode and the available empty states in the other. Hence, the tunneling current is

at a maximum and the tunneling resistance at a minimum. In the case of antiparallel configuration, the tunneling is between the majority states in one of the electrodes and minority states in the other. This mismatch results in a minimum of current and a maximum of resistance. The magnitude of the change in resistance is expected to be dependent on the spin polarization of the conduction electron in the FM electrodes, since tunneling current is spin polarized in MTJs.

Julliere introduced a simple model to explain the TMR: Suppose *a* and *a′* are the fractions of tunneling electrons in Fe and Co respectively whose magnetic moments are parallel to the magnetization. The spin polarization of the two ferromagnets is defined as $P_1 = 2a - 1$ and $P_2 = 2a' - 1$. For magnetizations in Fe and Co films are in parallel configuration, the conductance $G_{\uparrow\uparrow}$ is proportional to:

$$aa' + (1-a)(1-a') \tag{1.1}$$

For antiparallel configuration, the conductance $G_{\uparrow\downarrow}$ is proportional to:

$$a(1-a') + a'(1-a) \tag{1.2}$$

At low voltages electrons tunnel without spin-flips during the tunneling process, the relative conductance variation is given by:

$$\Delta G / G_{\uparrow\uparrow} = \left(G_{\uparrow\uparrow} - G_{\uparrow\downarrow}\right) / G_{\uparrow\uparrow} = 2P_1P_2 / (1 + P_1P_2) \tag{1.3}$$

The magnetoresistive effect due to the variation of the spin-dependent tunneling is normally expressed by:

$$TMR = \Delta R / R_{AP} = \left(R_{AP} - R_P\right) / R_{AP} = 2P_1P_2 / (1 + P_1P_2) \tag{1.4}$$

or

$$TMR = \Delta R / R_P = \left(R_{AP} - R_P\right) / R_P = 2P_1P_2 / (1 - P_1P_2) \tag{1.5}$$

where R_{AP} and R_P are tunneling resistance for antiparallel and parallel alignments of the two FM layers. We will quote all the results on the definition of Eq. (1.5) in this thesis.

The variation of the tunneling conductance in Jullière's work is about 14%, measured at 4.2 K. More recently, a large magnetoresistance of 18% at room temperature was demonstrated by Miyazaki *et al.*[9] and Moodera.[10] From then on, a great deal of interest has been taken in MTJs. The advantage of TMR devices is that the larger change in resistance can be obtained in smaller fields and the resistance can be engineered over a large range while maintaining constant device geometry. In future, magnetic recording density further increases, magnetic tunnel junctions may replace GMR read heads, due to the higher MR of MTJs. Compared to the MR ratio of an SV reading head, the TMR ratio of MTJs are larger and more sensitive. TMR ratio over 40% has been achieved by using $Co_{74}Fe_{26}$ ferromagnetic layer and an annealing process.[11]

1.2 Motivation and objective

The requirements on MTJs for read head applications are stringent. In order to produce reproducible MTJs, the effect of tunnel barrier, ferromagnetic layers and roughness of bottom ferromagnetic layer should be understood and controllable. The most challenging requirement is a low junction resistance. MTJs normally show unreasonably high junction resistance in micrometer and sub-micrometer size elements and the junction resistance depends critically on the barrier thickness. MTJs with a 40% MR ratio have a large resistance area product (*RA*) more than 1 $k\Omega\cdot\mu m^2$,[12] which implies poor response time and high Johnson noise in magnetic playback transducers. Therefore, from an application view point, a low junction resistance is required.

Another key problem in the fabrication of MTJ devices with high MR ratio is related to the surface roughness of the bottom electrode on which the tunnel barrier and top electrode are formed. If the surface roughness exceeds a certain critical value, the MTJ will fail either magnetically or electrically or in both ways. The former is mainly caused by dipole or orange-peel coupling between the bottom and top FM electrodes, while the latter is caused by pinholes formed in the thin insulating barrier.

Our work was carried out based on the problems above-mentioned. The surface roughness of the bottom FM electrode and a possible approach to reduce the junction resistance of MTJs were investigated.

The objectives of our studies are as follows:

- on the basis of the free-electron model, simulate the tunneling magnetoresistance and the exchange coupling in MTJ stacks with the structure of Nonmagnet/Ferromagnet/Insulator/Ferromagnet/Nonmagnet, looking into the effects of the parameters such as,
    - the thickness of the FM layers and the tunnel barrier, the spin polarization of the FM layers, the barrier height of the tunnel barrier, etc. on TMR and the exchange coupling
    - the interfacial roughness on TMR and the exchange coupling
- investigate the surface roughness control of the bottom $Ni_{80}Fe_{20}$ layer and related issues such as
    - the surface roughness and the magnetic properties of the bottom $Ni_{80}Fe_{20}$ thin film

- the magnetic properties of Co layer and the switching properties of MTJ stacks deposited on top of the bottom $Ni_{80}Fe_{20}$ layer with different surface roughness

- fabricate MTJ devices using a shadow mask technique with emphasis on
  - the effects of oxidation time on barrier properties and the performance of the MTJs
  - the effects of the microstructure of as-deposited metallic Al thin film for barrier formation on barrier properties and the performance of the MTJs

1.3 Organization of the dissertation

The organization of the dissertation is as follows:

Chapter 2 introduces the current status of the technology. We review the past research efforts by other groups in the beginning, followed by the key factors and problems that exist in MTJs. Chapter 3 gives our simulation work based on the free electron approximation. The TMR and the exchange coupling in MTJs, as well as the surface roughness effect on the performance of MTJs were investigated. Chapter 4 gives a brief introduction of the experimental measurement technologies used in our experiment studies. Chapter 5 describes the experimental work focused on surface roughness control and the corresponding effects on the magnetic properties of the thin films and switching properties of MTJ stacks. Chapter 6 presents the characteristics of MTJs fabricated by using a shadow mask technique. Chapter 7 summarizes the findings and the results of the dissertation and gives suggestions for future work.

[1] S. X. Wang and A. Taratorin, *Magnetic Information Storage Technology* (1999).

[2] G. A. Prinz and K. Hathaway, *Physics Today*, **48**, Special Issue: Magnetoelectronics (1995).

[3] G. A. Prinz, *J. Magn. Magn. Mater*. **200**, 44 (1999).

[4] B. E. Kane. *Nature*. **393**, 133 (1998).

[5] M. N. Baibich, J. M. Broto, A. Fert, F. Nguyen Van Dau, F. Petroff, P. Etienne, G. Cruezet, A. Friederich, and J. Chazelas, *Phys. Rev. Lett.* **61**, 2472 (1988).

[6] G. Binasch, P. Grünberg, F. Saurenbach, and W. Zinn, *Phys. Rev. B* **39**, 4828 (1989).

[7] http://www.readrite.com/html/whatnew/042902.html

[8] M. Jullière, *Phys. Lett.* **54A**, 225 (1975).

[9] T. Miyazaki, N. Tezuka, *J. Magn. Magn. Mater.* **139**, L231 (1995).

[10] J. S. Moodera, L. R. Kinder, T. M. Wong, R. Meservey, *Phys. Rev. Lett.* **74**, 3273 (1995).

[11] H. Kikuchi, M. Sato, and K. Kobayashi, *J. Appl. Phys.* **87**, 6055 (2000).

[12] K. Shimazawa, O. Redon, N. Kasahara, J. J. Sun, K. Sato, T. Kagami, S. Saruki, T. Umehara, Y. Fujita, S. Yarimizu, S. Araki, H. Morita, and M. Matsuzaki, *IEEE Trans. Magn.* **36**, 2542 (2000).

Chapter 2

Literature Review

In this chapter, we will give a literature review, which mainly focuses on experimental works done by other research groups related to MTJs. We will then give a brief introduction of several issues in MTJs. These issues include the magnetics of MTJs, the tunnel barrier, the spin polarization of the FM electrodes and the surface roughness of the bottom electrode.

2.1 History of MTJs

In 1975, Jullière [1] made the first reported magnetoresistance measurement on a ferromagnet/insulator/ferromagnet (FM/I/FM) junction. A change in the conductance of 14% with zero bias at 4.2 K with Fe/Ge/Co tunnel junctions was observed.

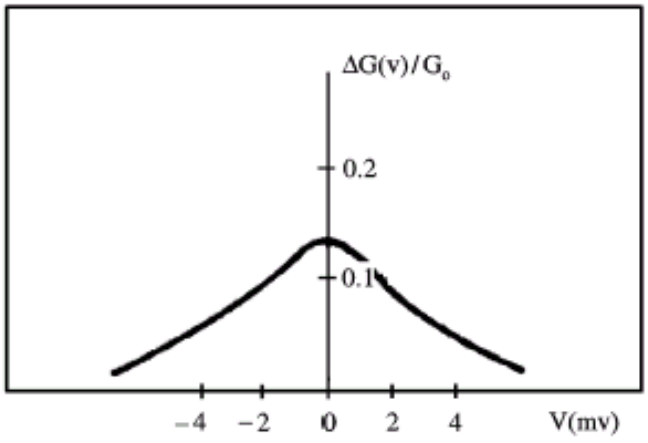

Figure 2.1 Relative conductances versus dc bias for Fe/Ge/Co junctions. (From Ref. 1)

However, the change in the conductance reduced rapidly with increasing applied dc bias, as shown in Fig. 2.1. Such a large dependence of TMR on bias was attributed to spin scattering at FM-I interfaces. After Jullière's work, several other groups also attempted to observe spin-dependent tunneling between two FM electrodes. Maekawa and Gafvert found a TMR of ~3% in Ni/NiO/Co at 4.2 K, supported by the M-H loops of the corresponding FM electrodes.[2] All the TMR measurements prior to 1995 were carried out at low temperature. That was because the TMR decreased rapidly as temperature increased and a much smaller value was observed even at 77 K. The experimental results were reproduced in other research groups by using NiO, CoO, GdO_x, and Al_2O_3 as the tunnel barrier, but only small changes were seen (no more than 7% at 4.2 K).[3-8] Miyazaki and Tezuka[9] improved the TMR at room temperature to 15.6% in 1995; however, these values were not reproducible and later found to be influenced by the geometrical nonlinear current flow effects, and the true values are much smaller. The real breakthrough happened in work by Moodera in 1995[10] when a larger TMR of over 10% could be obtained consistently and reproducibly at room temperature. From then on, TMR in FM/I/FM structures have attracted increasing attention. In order to understand the TMR in MTJs, it is necessary to give an introduction of the magnetics of MTJs.

2.2 Magnetics of MTJs

The MTJs has a current–perpendicular-to-plane (CPP) geometry and the current transport path is perpendicular to the planes of the two electrodes. The magnetoresistance effect in MTJs depends on the relative orientation of magnetization directions in two ferromagnetic layers. There are two ways to alter the relative alignment of magnetization

directions in two ferromagnetic layers. One way is choosing two magnetic layers with different coercivity (hard-pinned) and the second way is using an antiferromagnetic layer to exchange bias one of the ferromagnetic layers.

The basic magnetic hysteresis loops of two FM layers for the two cases and the corresponding magnetoresistance curves are given below. Figure 2.2 (a) is based on the two magnetic layers with different coercivity (hard-pinned) and Fig. 2.2 (b) is the exchange-biased structure. The solid line (dashed line) represents the MR curve when the magnetic field direction is changed from negative to positive (positive to negative direction).

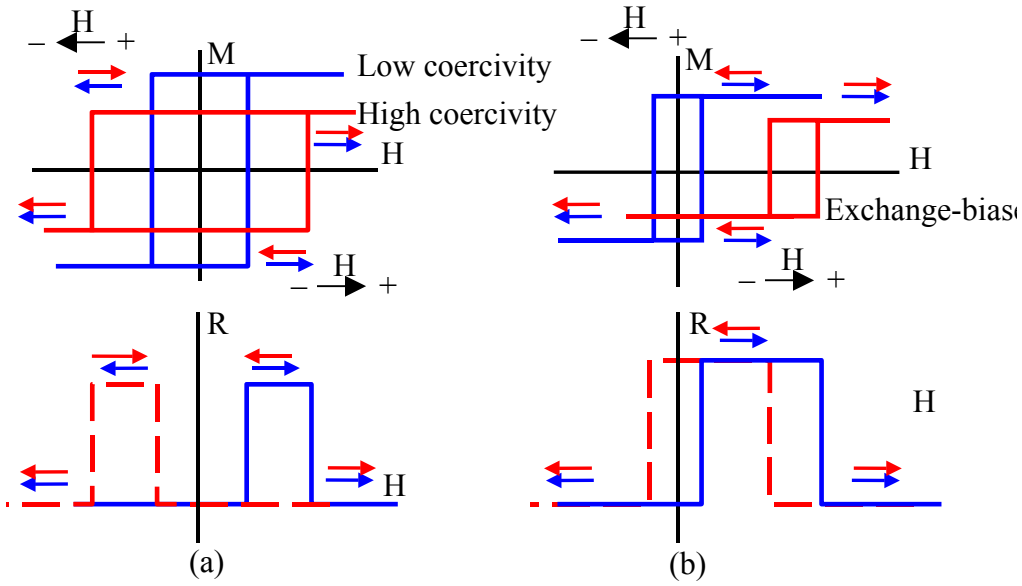

Figure 2.2 Magnetics of MTJs. (a) The hysteresis loops of two FM layers in a hard-pinned structure and the corresponding magnetoresistance (MR) curve. (b) The hysteresis loops of two FM layers in an exchange-biased structure and the corresponding MR curve.

In the hard-pinned structure, two ferromagnetic layers have different coercivities. When a magnetic field is applied and slowly changed from one direction to the other, the two layers switch over at different fields (corresponding to their coercivity values). In some regions, the layers have their magnetizations aligned parallel to each other and in other regions they are antiparallel (as indicated by the small arrows in the figures). The

measured resistance of the tunnel junction then changes as the relative orientation of magnetization direction in two ferromagnetic layers changes (as shown in Fig. 2.2 (a)). In an exchange-biased structure, one of the layers is placed in proximity to an antiferromagnetic layer. This antiferromagnetic layer can give rise to a net exchange coupling field to the ferromagnetic layer and shifts its hysteresis loop. The other ferromagnetic layer for such a structure is usually a soft magnetic material (low-coercivity) and works as a free layer (as shown in Fig. 2.2 (b)).

2.3 Some phenomena in MTJs

Although a relative high TMR ratio was obtained at room temperature, some phenomena in MTJs are still not clear, such as the bias and temperature dependence of TMR. At the same time, the thermal annealing process shows some interesting results. We will give a brief summary of these phenomena in following sections.

2.3.1 Bias voltage dependence of TMR

The current-voltage (I-V) characteristics of the non-magnetic metal/insulator/metal tunnel junctions are ohmic at low bias (compared with the barrier height), whereas at higher bias they have nonlinear characteristics. The dynamic conductance versus dc bias voltage has nearly a parabolic dependence. However, if one of the metal electrodes is ferromagnetic, such dependence will have a noticeable deviation. That is because the presence of magnons, magnetic impurities, and the interfacial states of barrier can affect the spin polarization of the FM electrode by causing spin flip scattering. One of the surprising

features exhibited in MTJs is the dc bias dependence of TMR. Even for MTJs with a high quality tunnel barrier, TMR shows a significant decrease with increasing bias voltage at all temperatures.[11, 12]

Many theories have been put forward to explain the dc bias dependence of the TMR; however, this phenomenon is not well understood yet. The possible reasons were attributed to several factors such as increase in the conductance with bias, excitation of magnons, and energy dependence of spin polarization due to the band structure effects.[13] Some calculations show that a significant part of the decrease of TMR can be attributed to magnon excitation,[14] which can also be seen from the inelastic electron tunneling (IET) spectra.[15] Figure 2.3 (a) shows the bias dependence of TMR at 295, 77 and 1 K. The TMR decreases monotonically as the dc bias increases. The normalized data in Fig. 2.3 (b) show the temperature independence of TMR variation with bias voltage.

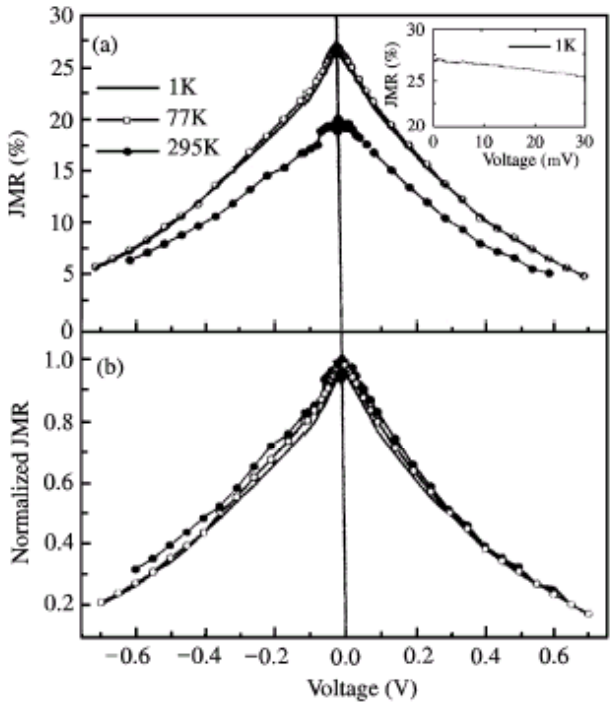

Figure 2.3 TMR versus dc bias at three temperatures for $Co/Al_2O_3/Ni_{80}Fe_{20}$ junction. Data shown are (a) the actual percentages and (b) normalized at zero bias. (From Ref. 14 and 15)

Although the dc bias dependence of TMR is a common phenomenon in MTJs, the magnitude of the decrease depends on the quality of the interfaces, barrier type and the FM electrodes. Junctions with a contaminated interface or which have a lower barrier height (MgO) will result in larger dependence on the bias. It was also observed that the junctions with Ni or NiFe electrodes showed a stronger decrease in TMR than junctions with Co or CoFe electrodes.

2.3.2 Temperature dependence of TMR

At low temperature, the observed TMR in MTJs has reached nearly the optimum values expected from Jullière's model;[3] however, there is a significant decrease in TMR at room temperature compared with the values at lower temperatures (4.2 or 77 K). The decrease of TMR occurs for all types of tunnel barriers and FM electrodes. The temperature (T) dependence of measured junction resistance (R_J) is not only found for MTJs, but also for a standard junction with nonmagnetic electrodes. This suggests a nonmagnetic origin of the R_J versus T behavior. That means in addition to the conductance due to direct elastic tunneling, there is a second conductance, which is unpolarized and hence independent of the relative orientations of the magnetization in FM layers. When we take into account the contributions from this part of the conductance, Jullière's model can be modified and written as: [16]

$$G(\theta) = G_T\left[1 + P_1 P_2 \cos(\theta)\right] + G_{SI} \tag{2.1}$$

where θ is the angle between the magnetization directions of two FM layers, G_T is the pre-factor for direct elastic tunneling, and G_{SI} is the unpolarized conductance. The

temperature dependence of this part may arise from the broadening of the Fermi distributions in FM electrodes, and the dependence of G_{SI} on temperature.

Besides the contribution of measured junction resistance, the spin polarization P of the FM layer is also a function of temperature. For alloys, it is established that P scales approximately with the magnetic moment of the alloy.[17] The magnetization versus temperature is described well by thermal excitation of spin waves for T far below the Curie temperature, leading to $T^{3/2}$ dependence of magnetization. Thus P can be expressed as:[18]

$$P(T) = P_0\left(1 - \alpha T^{3/2}\right) \tag{2.2}$$

The change in the conductance for parallel and antiparallel configurations is

$$\Delta G = 2G_T P_1 P_2 \tag{2.3}$$

In the case where G_T is not a function of temperature, the change of the conductance will directly reflect the temperature dependence of P_1 and P_2.

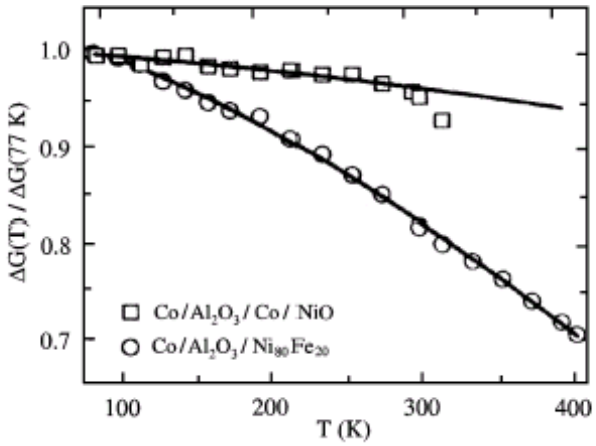

Figure 2.4 Temperature dependence of the normalized ΔG for two ferromagnetic junctions. The solid lines are the fits to the theory based on thermal spin-wave excitations. (From Ref. 19)

Shang *et al.* has studied the ΔG versus T for $Co/Al_2O_3/Ni_{80}Fe_{20}$ and $Co/Al_2O_3/Co/NiO$ junctions,[19] their results are shown in Fig. 2.4. The Al_2O_3 tunnel barrier in their studies

was a glow discharge oxidized Al layer (1.2~1.6 nm). It is clear that ΔG decreases as T increases in both structures. However, if we look at the slope of these two curves, Co-Co junction shows a much weaker decay compared with the junctions with $Ni_{80}Fe_{20}$ as one electrode. This difference may result from the different Curie temperatures of Co and $Ni_{80}Fe_{20}$. The origin of the unpolarized conductance may arise from some localized states due to the amorphous character of the Al_2O_3 insulator.

2.3.3 Annealing effect

A good thermal stability for MTJs is required for applications such as magnetic random access memory (MRAM). That is because standard processes such as sintering and plasma enhanced chemical vapor deposition (PECVD) for MRAM fabrication need to be performed at high temperature. Furthermore, it is known that one of the FM electrodes is usually exchanged biased by using an antiferromagnetic layer in MTJs structures for the purpose of obtaining a good antiparallel alignment of magnetization in MTJs. When annealing, one has to consider that the antiferromagnetic coupling induced biasing field has the possibility to be destroyed after the annealing process. Sato and Kobayashi[20] reported one of the cases where a FeMn layer was used to exchange bias the top FM layer in NiFe/Co/Al_2O_3/Co/NiFe/FeMn junctions. A TMR of 19% was achieved after annealing the junctions at 300°C for 1 h. They also studied the effect of annealing on performance of the junctions; the junctions survived and the TMR values were improved when the annealing temperature was higher than 200°C. Sousa *et al.* studied the effect of annealing on the junction resistance, TMR and barrier parameters of MTJs.[21] The optimum annealing temperature they found was around 230°C to obtain the maximum

TMR. Recently, Zhang *et al.*[22] studied the MTJs with one interposed Fe-FeO_x layer between the Al_2O_3 barrier and the top CoFe pinned electrode. Results show a large TMR of 40% for annealing up to 380°C. They found that the annealing temperature for maximum TMR occurence increases with the inserted Fe-FeO_x layer thickness. For junctions with a thicker inserted layer, the pinned layer moment increases with the annealing temperature up to 380°C and remains at a maximum until 450°C. This is highly encouraging from the application point of view. The explanations of TMR enhancement will be discussed more in the section on the barrier doping effect.

2.4 Key factors in MTJs

2.4.1 Tunnel barrier

A tunneling barrier with good properties, such as continuity, smoothness, homogeneity and absence of pinhole, is one of the most critical factors in determining the performance of MTJs. Jullière use α-Ge as the tunnel barrier, barrier materials tried subsequently by other research groups were mostly magnetic oxides such as NiO, CoO, or GdO_x. In all these studies, only a small TMR was observed at low temperature. The breakthrough occurred with Al_2O_3 barrier formed by oxidizing a thin Al layer, which is largely attributed to the excellent wetting properties of Al and the self-limiting effect during the oxidation. The self-limiting effect refers to the oxide films growing at a rate decreasing with thickness. Such a property has the desirable consequence of producing uniform film thickness. For thinner regions, the oxide will grow faster, thus tending to correct the thickness deficiency in different regions. For the TMR effect to be appreciable, the tunnel

barrier must be 2 nm or less in thickness. This is because the tunneling current is exponentially dependent on the barrier thickness. Due to the surface sensitivity of the tunneling process, especially for spin-dependent tunneling with magnetic electrodes, the interaction of the barrier material with the adjacent metal electrodes is also important. The presence of impurities, defects or metal inclusions in the barrier region will reduce the TMR effect dramatically by reducing the spin-polarized component of the tunneling current.

Only a few materials are suitable to form good tunnel barriers for spin-polarized tunneling, such as Al_2O_3, AlN,[23] Gd_2O_3, ZrO_x,[24] NiO,[25] MgO,[26, 27] HfO_2, [28] TaO_x,[29] BN,[30] $ZrAlO_x$,[31] ZrS[32] and $SrTiO_3$. The most successful barrier materials for MTJs are Al_2O_3, AlN, and MgO, whereas other barrier materials that have been tried are in general non-stoichiometric or magnetic.[28, 33] In the next section, we will specially discuss the Al_2O_3 barrier properties effect on TMR ratio in MTJs.

2.4.1.1 Barrier thickness

In the case of Al_2O_3, extensive studies have been carried out to determine the optimum Al film thickness for barrier formation. In general, most of the research groups have used Al thickness values in the range from a few Å to about 30 Å, and mostly in the upper range. However, from an application view point, an even thinner Al film is needed to satisfy the requirement of lower junction resistance. One approach to achieve the low junction resistance MTJs is to decrease the barrier thickness in the case of Al oxide. TMR ratio as a function of Al film thickness was studied by Moodera *et al.*[34] and the result was plotted

in Fig. 2.5. It is clear that the optimal thickness of Al film ranges from 7 to 18 Å according to the type of FM electrodes.

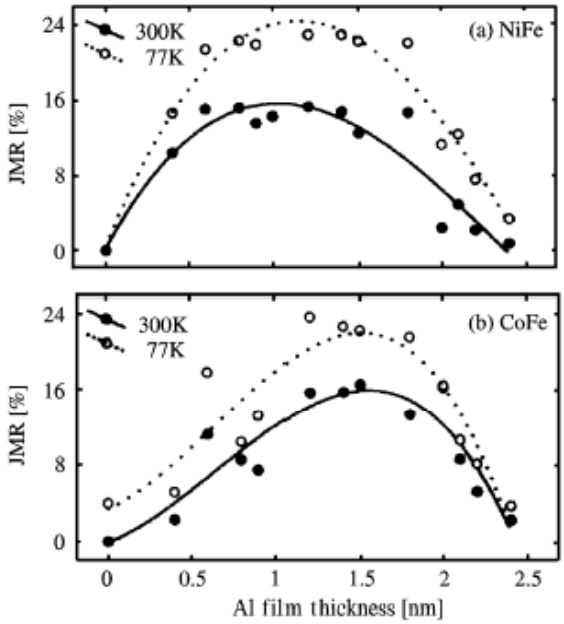

Figure 2.5 TMR plotted as a function of the thickness of Al metal overlayer used to form the Al_2O_3 barrier in (a) $Co/Al_2O_3/Ni_{80}Fe_{20}$ and (b) $Co/Al_2O_3/Co_{50}Fe_{50}$ tunnel junctions. (From Ref. 34)

Besides the barrier thickness, barrier properties also depend greatly on its quality. The existence of states in the barrier due to nonstoichiometry, impurity atoms and defects may give rise to excitations such as magnons and phonons, thereby destroying the I-V characteristics of junctions. The quality of the barrier can be evaluated by I-V characteristics of MTJs and the effective barrier parameters obtained by I-V curve fitting.

2.4.1.2 Barrier doping effect

When different types of foreign elements were introduced into the tunnel barrier in magnetic tunnel junctions, dopants induced electron spin scattering could be investigated in a systematic and controlled manner. Generally, tunneling electrons originate from

states in a narrow energy interval around the Fermi level. Therefore, the scattering at the Fermi energy is very important.

When a spin-flip event occurs in the barrier, it means that a spin-up electron changes its spin direction during the tunneling process from one FM layer (FM1) to another (FM2). This is equivalent to the magnetization of FM2 having been reversed. If we denote the fraction of tunneling electrons undergoing a spin flip by *f*, the conductance for the parallel magnetization configuration becomes $(1-f)G_P + fG_{AP}$ and a similar expression can be obtained for the antiparallel case. Consequently, the TMR can be written as,

$$TMR = \frac{(1-2f)\cdot TMR^0}{1-f\cdot TMR^0} \tag{2.4}$$

where TMR^0 represents the magnetoresistance in the case of no spin-flip scattering ($f = 0$). The TMR is thus expected to decrease as the fraction *f* increases.

The barrier doping effect on magnetoresistance of MTJs was investigated in $Co/Al_2O_3/NiFe$ junctions with submonolayer amounts of dopants incorporated into the middle of the insulating oxide.[35] The submonolayer of dopant was sandwiched between two 7 Å thick Al layers. Subsequently the Al and the dopants were completely transformed into oxides by plasma oxidation. The oxidation states of tunnel barrier in their studies were confirmed by XPS. Dopants of Ni, Co, Pd, Au, and Cu were investigated at the submonolayer level. Figure 2.6 shows the TMR as a function of thickness at 77K for various dopants, normalized to the TMR of the corresponding control junctions. Results indicate that the TMR decreases almost linearly as the dopants thickness increases.

The thickness of the Al layer for barrier formation in their studies is 1.4 nm, which is the optimal value to obtain the highest TMR for MTJs with NiFe as one of the FM layers.[34] We can see from their results (From Ref. 34) that even the increase of the thickness of the Al layer, TMR will decrease. However, this work does not take into account the influences of the barrier thickness on TMR ratio of MTJs. At least, a set of control sample with Al as the layer of impurities (with the same thickness as that of other impurities) should be fabricated and the reduction of the TMR induced by the impurities layer should be evaluated carefully.

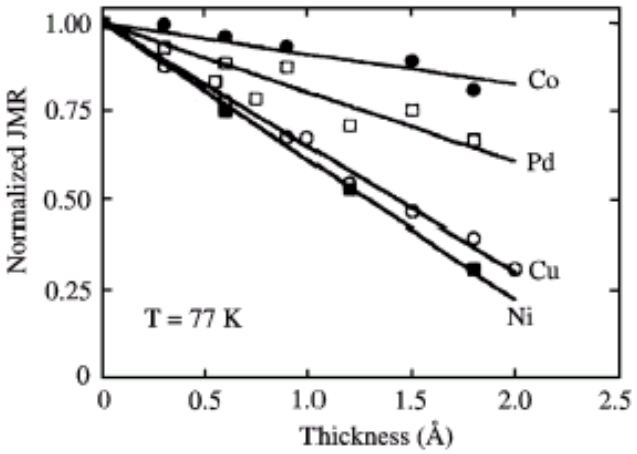

Figure 2.6 Normalized TMR vs. thickness of the layer of impurities present in the tunnel barrier (measured at 77 K), for Co, Pd, Cu, and Ni, together with a linear fit (solid lines). (From Ref. 35)

The linear dependence attributed to the spin-flip event occurs at the dopant submonolayer, and the possibility of spin-flip event occurrence was proportional to thickness of the dopants. Other elements like Au and Si were also found to produce a reduction of TMR. However, when the Fe dopant layer was introduced to the middle of two Al films, an enhancement of TMR occurs. Jansen *et al.*[36] studied the thickness of Fe dopant layer dependence of TMR and they found that the TMR enhancement occurs for all Fe thickness up to 1.8Å, with a maximum roughly between 0.5 and 1Å of Fe. The

effect not only occurs at low temperature, but also is still significant even at room temperature.

They put forward several possible explanations for the enhancement effect. The most interesting possibility is that an ultra-thin layer of Fe_3O_4 was formed in the barrier. Fe_3O_4 is a half-metallic ferromagnet, and such a layer may create states near the Fermi level for one spin exclusively, thus resulting in a spin asymmetry near the Fermi level. Such a spin asymmetry will give rise to the enhancement of the TMR. A second explanation may be that the wave functions of the Fe dopants mix with the electrode wave functions in such a way that the tunneling electron polarization is enhanced. It means that the orbits of the Fe-ions should couple preferentially to the highest spin-polarized wave functions of the electrodes. A third explanation relates to the inherent defects and disorder formed during the formation of the Al_2O_3 barrier. These defects, when present in significant density, can cause the TMR to be less than the ideal value. Therefore, a possible reason would be that the presence of Fe in the barrier modifies the structural properties of the barrier, thereby reducing disorder and the negative effect associated with it.

Although several possible explanations have been put forward, further studies are required to uncover the physical origins behind the phenomenon. As we mentioned in section 2.3.3, TMR ratio of 40% for MTJs with the inserted Fe-FeOx layer between the tunnel barrier and top FM layer was achieved even with the annealing temperature up to 380^0C. It is worthwhile to elucidate the origin of the TMR enhancement, in particular to relate the observed effect of the Fe dopants to the precise structural and electronic properties of the dopants.

2.4.1.3 MTJs with low resistance

As we mentioned before, MTJs with a 40% MR ratio have a large resistance area product (*RA*) more than 1 kΩ·μm^2.[37] A low resistance junction with *RA* less than 10 Ω·μm^2 is required for application purpose. In order to achieve this, there are two approaches; one is to decrease the barrier thickness of Al oxide and the other is to select the barrier material with lower barrier height. A lot of work has been done on these approaches and some useful results have been obtained. Later we will give a brief summary of the work focused on investigating MTJs with a lower *RA* and a high TMR ratio.

For low resistance junctions by reducing the barrier thickness, naturally oxidized AlO_x barrier (5~7 Å Al) was used by various research groups. Results demonstrated a junction *RA* in the range of 10~20 Ω·μm^2, but with TMR decreased to 10%~20%.[38-42] Zhang *et al.* [43] studied the junctions with AlO_x barrier, which was fabricated by using in situ natural oxidation of a 7Å thick Al thin film. Junction *RA* as low as 10~12 Ω·μm^2 was achieved with corresponding TMR ratio ranging from 14%~17%. Fujikata *et al.* [44]studied the stacked top-type and bottom-type MTJs structures with the top and the bottom antiferromagnetic (AF) layers prepared on Ta seed layers exposed to O_2 surfactant gas to improve the roughness of the bottom ferromagnetic layer and the Al coverage. A TMR ratio of 12%~17% with RA products of 6~7 Ω·μm^2 were obtained.

The low resistance MTJs has been achieved by reducing Al film thickness down to 5 to 7 Å. However, low resistance MTJs structures with ultra-thin barriers have a lower TMR ratio compared with thick barriers, which is due to the incomplete barrier oxidation and/or pinhole formation in the barrier region. Besides the drop of the TMR ratio, such thin barriers can even introduce other problems. First, fabrication of such a thin barrier is

very difficult. Secondly, for such thin barriers, the exchange coupling between two ferromagnetic layers will affect the magnetic response of the device. Finally, the current distribution in the barrier is very sensitive to the thickness fluctuation of the barrier.

Considering all these disadvantages of ultra-thin AlO_x barrier, one solution is to use low height tunnel barrier. For the same junction resistance, it is clear that MTJs with lower barrier height will have thicker barrier thickness. If we assume that the roughness of high and low height barriers to be the same, thicker barrier will reduce the orange peel coupling between two ferromagnetic layers. At the same time, the current distribution will be less sensitive to the barrier thickness fluctuation, and the barrier will be easier to fabricate.

Some research groups have fabricated MTJs with lower barrier height, such as HfO_x[28], MgO[45], AlN, and AlO_xN_y. Only AlN and AlO_xN_y[46] have shown TMR ratios near 20% with lower junction resistance. TaO_x barrier has been studied by Rottiander *et al.* [47] and the TMR ratio of 2.5% at room temperature is obtained by using proper Ta film thickness and oxidation conditions. Compared to the barrier height of AlO_x (1~1.5 eV), a lower barrier heights of 0.3~0.4 eV are achieved. Wang *et al.* [48] fabricated the MTJs with $ZrAlO_x$ barriers and TMR ratio of 15.3% with RA products 5~9 $\Omega\cdot\mu m^2$ is obtained. Although some exciting results have been obtained, further work is still needed for the application of low resistance MTJs to become a reality.

2.4.1.4 The effect of inert gas in the oxidation process

Besides the barrier thickness and barrier materials, the methods used for barrier formation affect the properties of tunnel barrier as well. Various oxidation methods have been used

to form the tunnel barrier in MTJs. In the plasma oxidation method, an Ar and O_2 mixture is usually used. For the purpose of achieving the optimal oxidation condition, the experimental parameters such as the mixing ratio of Ar and O_2, the applied power density to the discharge plasma, and the oxidation time generally need to be considered. In most of the previous work, little attention was paid to the role of the inert gas in the oxidation process. In the field of metal-oxide-semiconductor fabrication, it is well known that the electric properties of a thin gate insulating layer fabricated by plasma oxidation of Si depends greatly on the inert gas mixed in the oxygen plasma. The gate insulating layer plasma oxidized in the Kr and O_2 mixture shows excellent electric properties (lower interface trap density at the SiO_2/Si interface) compared to the case in which the Ar and O_2 mixture is used. Kr-O_2 plasma also gives a very uniform gate oxidation layer even on a shallow trench isolation edge. The reason is that a homogeneous oxidation rate is obtained irrespective of the crystallographic orientation of the Si Surface.[49, 50]

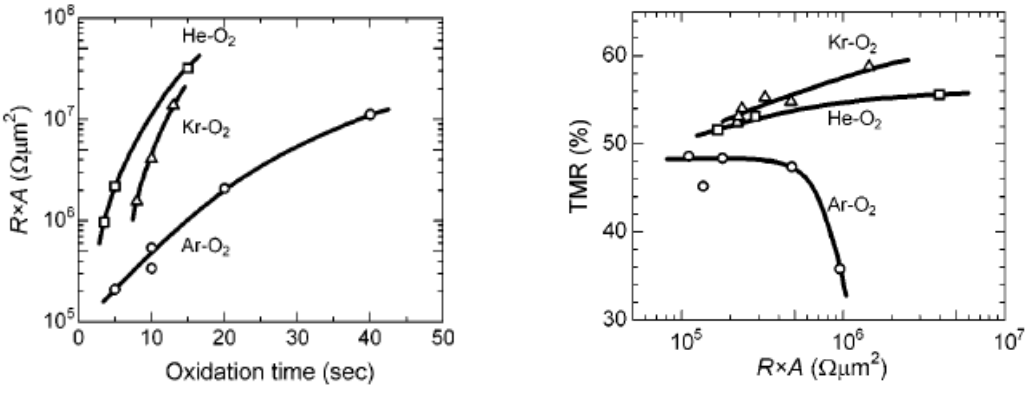

(a) (b)

Figure 2.7 (a) RA product of as-deposited MTJs vs. oxidation time and (b) TMR ratio obtained during the annealing process vs. the corresponding RA product, for the tunnel junction oxidized with different species of inert gas mixed plasma, respectively. (From Ref. 51)

Recently, a study of the effect of inert gas on the properties of the tunnel barrier has been carried out by Tsunoda *et al.*[51] The influence of the inert gas species mixed in the plasma

for oxidation of metallic Al films on the TMR ratio of MTJs was investigated. He, Ar, and Kr were used as the inert gas mixed with O_2 gas for the plasma oxidation in their studies, respectively. Figure 2.7 (a), from Ref. 51, shows the changes of the *RA* of as-prepared junctions as a function of the plasma oxidization time. In the case of the junctions fabricated with He–O_2 and Kr–O_2 plasma, *RA* increases more rapidly than in the case of the junctions fabricated with Ar–O_2 plasma, as the oxidization time increases. It means that the mixing inert gas species affects the oxidization rate of the metallic Al layer. Figure 2.7 (b), from Ref. 51, shows the maximum TMR ratio obtained after annealing processes for MTJs oxidized with different species of inert gas mixed plasma. We can see very clearly from the figure that in the case of He-O_2 and Kr-O_2 plasma, a large TMR excess of 50% was achieved for MTJs after annealing at 270^0C~300^0C. The maximum TMR ratio in their studies is 58.8% in Kr-O_2 plasma and annealed at 300^0C.

If we look at the relationship between the TMR ratio and the junction *RA*, it can be found that the behavior of TMR in Ar-O_2 case is different from the other two cases. The TMR of MTJs fabricated with Ar-O_2 plasma maintains a value of about 48% when the *RA* is less than 5×10^5 $\Omega\cdot\mu m^2$, then decreases to 36% when *RA* reaches 10^6 $\Omega\cdot\mu m^2$. However, in the cases of He-O_2 and Kr-O_2, the TMR can exceed 50% for $RA \approx 2\times10^5$ $\Omega\cdot\mu m^2$ and continues to increase for *RA* to be larger than 10^6 $\Omega\cdot\mu m^2$. The reason of the TMR drop in higher resistance region in the case of Ar-O_2 plasma is attributed to the over oxidation mechanism.[52-54] MTJs fabricated with He-O_2 and Kr-O_2 plasma show larger TMR ratio even through they have higher resistance than the over oxidized MTJs in the Ar-O_2 case. That means the over oxidation is not significant for MTJs fabricated with He-O_2 and Kr-O_2 plasma. The authors attributed this to the difference of the oxidation

process of metallic Al films by using various mixing inert gases. The oxygen will permeate to the underlayer surface through the grain boundaries rather than the interior of the grain of the metallic Al layer because the diffusing mobility of oxygen is generally larger at the grain boundaries than the bulk of the grain. Thus, the distribution of the oxygen in MTJs along the film thickness direction will spread as the oxidization time increases, and the underlying ferromagnetic electrode surface will be easily oxidized. Taking into account the oxidization rate shown in Fig. 2.7 (a), one says that a faster oxidization rate for the Kr–O_2 or He–O_2 cases than the Ar–O_2 case was favorable to prevent the oxidization of the underlying ferromagnetic electrode surface and this resulted in the large TMR even in the high resistance MTJs.

2.4.2 Ferromagnetic electrodes

The ferromagnetic electrodes play a critical role in MTJs. According to Jullière's model, the maximum TMR ratio could be achieved depends on the spin polarization of two FM layers. Furthermore, the surface roughness of the bottom FM layers can affect both the reproductivities and the magnetic responses of the MTJs. The descriptions related to these two issues will be given in the following sections.

2.4.2.1 Spin polarization of the FM electrodes

The other key factor is the spin polarization (P) of the FM electrode. For a transition metal ferromagnet, the value of P is mainly dependent on the spin-dependent density of states at the Fermi surface. It can be expressed by the formula below:

$$P = \frac{[D^{\uparrow}(E_F) - D^{\downarrow}(E_F)]}{[D^{\uparrow}(E_F) + D^{\downarrow}(E_F)]} \tag{2.5}$$

where the $D^{\uparrow}(E_F)$ and $D^{\uparrow}(E_F)$ are the density of states of spin-up and spin-down electron, respectively. According to the previous theoretical model, a higher TMR ratio could be achieved by using the ferromagnetic materials with large spin polarization. The values of *P* for some ferromagnetic materials measured by using different techniques are listed in Table 2.1.[55-57]

Table 2.1 Spin polarizations obtained in experiments by different techniques.

Electrode Material	Spin polarization *P* (%) old values [from ref 55]	Spin polarization *P* (%) new values [from ref 56,57]
Ni	23	33
Co	35	42
Fe	40	45
$Ni_{80}Fe_{20}$	32	48
$Co_{84}Fe_{16}$	--	55

In real situations, the polarization of some ferromagnetic materials not only varies in magnitude when different tunnel barrier materials are used but they are even known to change sign.[58] That is thought to be due to the fact that the tunnel current emerges from the thin layer of metallic electrode with a band structure unlike the bulk metal owing to hybridization with the insulating material. Therefore, for spin tunneling processes, it is inappropriate to attempt to assign a given spin polarization to a particular ferromagnetic material. It is proper to assign polarizations to combinations of the ferromagnetic and insulator materials.[59]

2.4.2.2 Surface roughness of the bottom FM electrode

A bottom FM electrode with a smooth surface is very important to the performance of the MTJs devices. First, the surface roughness of the bottom FM electrode can lead to dipolar or orange-peel coupling[60] between the bottom and top FM electrodes. Such a coupling will not allow independent switching of the magnetization of the two magnetic layers. It has been shown experimentally that interface roughness may affect the interlayer magnetic coupling between thin films in multilayer structures.[61] Accordingly, the dynamic magnetic response of multilayer structures to an external field can also be altered by surface roughness. Néel derived equation (2.6) for the coupling energy, *J*, between two ferromagnetic films.

$$J = \frac{\pi^2}{\sqrt{2}} \frac{h^2}{\lambda} (\mu_0 M M') \exp\left(\frac{-2\pi t \sqrt{2}}{\lambda} \right) \tag{2.6}$$

M and *M′* are the saturation magnetization of the films, which are separated by a barrier thickness *t*. The interface roughness is described by a two-dimensional sinusoidal function with amplitude *h* and wavelength λ.

Second, growing a thin insulator as a tunnel barrier over a rough surface is nearly impossible due to non-uniform coverage of the insulator. Even if one were to succeed in obtaining a working junction using a thick insulator, the results will be unstable because the tunneling will take place at only a few hot spots. This also will give rise to enormously high current densities in these regions, thus leading to premature breakdown. Furthermore, due to the surface sensitivity of the tunneling process, the interfacial roughness induced by surface roughness of the bottom FM layer will cause spin

scattering at the interfaces, thus affecting the performance of MTJs. Therefore, reducing the spin scattering at the interface also requires a smooth bottom ferromagnetic layer.

Because of the application potential on magnetic recording devices, the magnetic properties of ferromagnetic surfaces and interfaces have been extensively investigated.[62] Due to the reduction of dimensionality and coordination of surface atoms, it was reported in some studies that there should be a large enhancement of magnetic moments at the surface of ferromagnetic materials.[63-66] It is also known that the dead layer may exist in ultra-thin films and induce the reduction of the magnetic moment somehow. Most of the previous studies on surface magnetism are based on the assumption that the film surface of ferromagnetic materials is perfectly smooth. However, real films have a finite roughness. The atomic height of surface atoms can fluctuate by a few atomic lattice spacings because of the formation of different types of defects, such as steps, vacancies, and islands. The rearrangement of the surface atoms is expected to affect the magnetic properties of very thin films. Therefore, establishing the relationship between surface roughness and magnetic properties of thin films is essential to develop new magnetic devices using magnetic multilayer structures.

Extensive studies have been made on the relationship between surface roughness and magnetic properties of thin and ultra-thin films. Li *et al.* [67] investigated magnetic and morphological properties of Co films deposited on Si substrates after plasma-etching for different times. The smoother films showed uniaxial magnetic anisotropy, which decreased with the increase of the surface roughness and disappeared for the roughest films. Investigation by Ebothe *et al.* [68] on a 2 μm thick electrodeposited NiCo alloy film showed a nonlinear dependence of coercivity on surface roughness. The microstructure

and the magnetic properties of Co/Pt multilayer thin films deposited on various pre-treated substrates have been studied by Chang and Kryder.[69] They found that the roughness lowered uniaxial anisotropy and raised the coercivity of Co/Pt multilayers. Choe and Steinback[70] studied the surface roughness dependence of magnetoresistive and magnetic properties of $Ni_{81.5}Fe_{18.5}$ thin films deposited on substrates that were pre-treated by Ar ion etching to induce different surface roughness. They found that strongly textured $Ni_{80}Fe_{20}$ (111) deposited onto smooth substrate yields higher anisotropy and lower coercivity than those grown onto rough substrates over a wide range of $Ni_{80}Fe_{20}$ thicknesses. Besides the magnetic properties of $Ni_{80}Fe_{20}$ thin films, using $Ni_{80}Fe_{20}$ as an underlayer can also have a great influence on the crystallography of successively deposited layers, leading to different switching properties.[71]

Most of the work mentioned thus far utilized substrates with pre-treatment before film deposition in order to produce different surface roughness. It would be useful to develop an in-situ method that may improve the surface roughness of the multilayer structure during film deposition. In our studies, we investigated the dependency of the surface roughness of $Ni_{80}Fe_{20}$ thin films on experimental conditions. An in-situ control of surface roughness of ferromagnetic thin films was proposed. $Ni_{80}Fe_{20}$ was chosen because it could be used as an underlayer to control the crystallography of successively deposited layers, which has been demonstrated experimentally by Choe *et al.*[71] in spin valves. Besides the experimental works, the effect of the interfacial roughness induced by bottom FM layer on TMR and exchange coupling in MTJs were investigated theoretically and the simulation results were presented in Chapter 3.

[1] M. Jullière, *Phys. Lett.* **54A**, 225 (1975).

[2] S. Maekawa, U. Gafvert. *IEEE, Trans. Magn.* **MAG-18**, 707 (1982).

[3] Y. Suezawa, Y. Gondo, *Proc. Int. Symp. Phys. Magn. Mater.*, 303 (1987).

[4] J. Nowak, J. Rauluszkiewicz, *J. Magn. Magn. Mater.* **109**, 79 (1992).

[5] Y. Suezawa, F. Takahashi, Y. Gondo, *Jpn. J. Appl. Phys.* **31**, L1415 (1992).

[6] T. Yaoi, S. Ishio, T. Miyazaki, *J. Magn. Magn. Mater.* **126**, 430 (1993).

[7] T. S. Plaskett, P. P. Freitas, N. P. Barradas, M. F. da Silva, and J. C. Soares, *J. Appl. Phys.* **76**, 6104 (1994).

[8] P. LeClair, J. S. Moodera, R. Meservey, *J. Appl. Phys.* **76**, 6546 (1994).

[9] T. Miyazaki, N. Tezuka, *J. Magn. Magn. Mater.* **139**, L231 (1995).

[10] J. S. Moodera, L. R. Kinder, T. M. Wong, and R. Meservey, *Phys. Rev. Lett.* **74**, 3273 (1995).

[11] J. Zhang and R. M. White, *J. Appl. Phys.* **83**, 6512 (1998).

[12] Y. Lu, X. W. Li, X. Gang, R. A. Altman, W. J. Gallagher, C. Marley, K. Roche, and S. S. P. Parkin, *J. Appl. Phys.* **83**, 6515 (1998).

[13] J. S. Moodera and L. R. Kinder, *J. Appl. Phys.* **79**, 4724 (1996).

[14] A. M. Bratkovsky, *Phys. Rev. B.* **56**, 2344 (1997).

[15] J. S. Moodera, J. Nowak, and J. M. van de Veerdonk, *Phys. Rev. Lett.* **80**, 2941 (1998).

[16] C. H. Shang, J. Nowak, R. Jansen, J. S. Moodera, *Phys. Rev. B.* **58**, R2917 (1998).

[17] D. Paraskevopoulos, R. Meservey, P. M. Tedrow, *Phys. Rev. B.* **16**, 4907 (1977).

[18] R. Meservey, D. Pereskevopoulos, P. M. Tedrow, *Phys. Rev. Lett.* **37**, 858 (1976).

[19] C. H. Shang, J. Nowak, R. Jansen, and J. S. Moodera*, Phys. Rev. B.* **58**, R2917 (1998).

[20] M. Sato, K. Kobayashi, *IEEE, Trans. Magn.* **33**, 3553 (1997).

[21] R. C. Sousa, J. J. Sun, V. Soares, P. P. Freitas, A. Kling, M. F. da Silva, and. J. C. Soares, *Appl. Phys. Lett.* **73**, 3288 (1998).

[22] Z. Z. Zhang, S. Cardoso, P. P. Freitas, X.Batlle, P. Wei, N. Barradas, and J. C. Soares, *J. Appl. Phys.* **89**, 6665 (2001).

[23] J. R. Childress, M. M. Schwickert, R. A. Fontana, M. Ho, and B. A. Gurney, *J. Appl. Phys.* **89**, 7353 (2001).

[24] J. G. Wang, P. P. Freitas, E. Snoeck, P. Wei, and J. C. Soares, *Appl. Phys. Lett.* **79**, 4387 (2001).

[25] J. Nowa and J. Rauluszkiewicz, *J. Magn. Magn. Mater.* **109**, 79 (1992).

[26] J. S. Moodera and L. R. Kinder, *J. Appl. Phys.* **79**, 4724 (1996).

[27] C. L. Platt, B. Dieny, and A. E. Berkowitz, *J. Appl. Phys.* **81**, 5523 (1997).

[28] C. L. Platt, B. Dieny, A. E. Berkowitz, *Appl. Phys. Lett.* **69**, 2291 (1996).

[29] P. Rottlander, M. Hehn, O. Lenoble and A. Schuhl, *Appl. Phys. Lett.* **78**, 3274 (2001).

[30] R. A. Lukazew,Y. Sheng, C. Uher, R. Charke, *Appl. Phys. Lett.* **75**, 1941(1999).

[31] J. G. Wang, P. P. Freitas, E. Snoek, *Appl. Phys. Lett.* **79**, 4553 (2001).

[32] M. Guth, A. Dinia, G. Schneba, and H. A. M. Van Den Berg, *Appl. Phys. Lett.* **78**, 3487 (2001).

[33] J. Nowak, J. Rauluszkiewicz, *J. Magn. Magn. Mater.* **109**, 79 (1992).

[34] J. S. Moodera, E. F. Gallagher, K. Robinson, and J. Nowak, *Appl. Phys. Lett.* **70**, 3050 (1997).

[35] R. Jansen and J. S. Moodera, *J. Appl. Phys.* **83**, 6682 (1998).

[36] R. Jansen and J. S. Moodera, *Appl. Phys. Lett.* **75**, 400 (1999).

[37] K. Shimazawa, O. Redon, N. Kasahara, J. J. Sun, K. Sato, T. Kagami, S. Saruki, T. Umehara, Y. Fujita, S. Yarimizu, S. Araki, H. Morita, and M. Matsuzaki, *IEEE Trans. Magn.* **36**, 2542 (2000).

[38] D. Song, J. Nowak, R. Larson, P. Kolbo, and R. Chellew, *IEEE Trans. Magn.* **36**, 2545 (2000).

[39] K. Ohashi, K. Hayashi, K. Nagahara, K. Ishihara, E. Fukami, J. Fujikata, S. Mori, M. Nakada, T. Mitsuzuka, K. Matsuda, H. Mori, A. Kamijo, and H. Tsuge, *IEEE Trans. Magn.* **36**, 2549 (2000).

[40] P. P. Freitas, S. Cardoso, R. C. Sousa, W. J. Ku, R. Ferreira, V. Chu, and J. P. Conde, *IEEE Trans. Magn.* **36**, 2796 (2000).

[41] J. J. Sun, K. Shimazaw, N. Kasahara, K. Sato, T. Kagami, S. Saruki, S. Araki, and M. Matsuzaki, *J. Appl. Phys.* **89**, 6653 (2001).

[42] J. R. Childress, M. M. Schwickert, R. A. Fontana, M. Ho, and B. A. Gurney, *J. Appl. Phys.* **89**, 7353 (2001).

[43] Z. G. Zhang, P. P. Freitas, A. R. Ramos, N. P. Barradas, and J. C. Soares, *Appl. Phys. Lett.* **79**, 2219 (2001).

[44] J. Fujikata, T. Ishi, S. Mori, K. Matsuda, K. Mori, H. Yokota, K. Hayashi, M. Nakada, A. Kamijo, and K. Ohashi, *J. Appl. Phys.* **89**, 7558 (2001).

[45] E. Popova, J. Faure-Vincent, C. Tiusan, C. Bellouard, H. Fischer, M. Hehn, F. Montaigne, M. Alnot, S. Andrieu, and A. Schuhl, *Appl. Phys. Lett.* **81**, 1035 (2002).

[46] P. Shang, K. Amanda, Janice H. Nickel, Manish Sharma, and Thomas C. Anthony, *J. Appl. Phys.* **89**, 6874 (2001)

[47] P. Rottiander, M. Hehn, O. Lenoble and A. Schuhl, *Appl. Phys. Lett.* **78**, 3247 (2001).

[48] J. G. Wang, P. P. Freitas and E. Snoeck, *Appl. Phys. Lett.* **79**, 4553 (2001).

[49] N. Ueda, Y. Saito, M. Hirayama, Y. Yamauchi, S. Sugawa, and T. Ohmi, *Jpn. Soc. Appl. Phys.*, 164 (2001).

[50] T. Hamada, Y. Saito, M. Hirayama, H. Aharoni, and T. Ohmi, *IEEE Trans. Electron Devices* **22**, 423 (2001).

[51] M. Tsunoda, K. Nishikawa, S. Ogata, and M. Takahashi, *Appl. Phys. Lett.* **80**, 3135 (2002).

[52] M. Sato, H. kikuchi, and K. Kobayashi, *J. Appl. Phys.* **83**, 6691 (1998).

[53] J. J. Sun, V. Soares, and P. P. Freitas, *Appl. Phys. Lett.* **74**, 448 (1999).

[54] D. Song, J. Nowak, and M. Covington, *J. Appl. Phys.* **87**, 5197 (2000).

[55] P. M. Tedrow and R. Meservey. *Phys. Rev. Lett.* **26**, 192 (1973).

[56] J. S. Moodera, J. Nassar and G. Mathon, *Annu. Rev. Mater. Sci.* **29**, 381 (1999).

[57] D. J. Monsma and S. S. P. Parkin, *Appl. Phys. Lett.* **77**, 720 (2000).

[58] J. M. de Teresa, A. Barthelemy, A. Fert, J. P. Contour, F. Montaigne and P. Seneor, *Science* **286**, 507 (1999).

[59] P. LeClair, H. J. M. Swagten, J. T. Kohlhepp, R. J. M. van de Veerdonk, and W. J. M. de Jonge, Phys. Rev. Lett., **84**, 2933 (2000).

[60] L. Nèel, C. R. Acad. *Sci. A* **122**, 521 (1963).

[61] D. T. Pierce, J. A. Stroscio, and J. Unguris, *Phys. Rev. B* **49**, 14564 (1994).

[62] L. M. Falicov *et al.*, *J. Mater. Res.* **5**, 1299 (1990).

[63] C. S. Wang and A. J. Freeman, *Phys. Rev. B* **24**, 4364 (1981).

[64] H. Krakauer, A. J. Freeman, and E. Wimmer, *Phys. Rev. B* **28**, 610 (1983).

[65] O. Jepsen, J. Madsen, and O. K. Andersen, *Phys. Rev. B* **26**, 2790 (1982).

[66] F. Liu, M. R. Press, S. N. Khanna, and P. Jena, *Phys. Rev. B* **39**, 6914 (1989).

[67] M. Li, G. C. Wang, and H. G. Min, *J. Appl. Phys.* **83**, 5313 (1998).

[68] J. Ebothe, S. Vilain, and M. Troyon, *J. Magn. Magn. Mater.* **157**, 274 (1996).

[69] C. Chang and M. H. Kryder, *J. Appl. Phys.* **75**, 6864 (1994).

[70] G. Choe and M. Steinback, *J. Appl. Phys.* **85**, 5777 (1999).

[71] G. Choe, A.Tsoukatos, and S. Gupta, *IEEE Trans. Magn.* **34**, 867 (1998).

Chapter 3

Simulation of Magnetoresistance and Exchange Coupling in MTJs

As mentioned in last two chapters, the tunnel magnetoresistance depends greatly on several factors, e.g., the spin polarization of the ferromagnetic layers, the tunnel barrier and the surface roughness of the interface. At the same time, the exchange coupling of the two ferromagnetic layers in MTJ stacks due to the very thin tunnel barrier would influence the switching properties of MTJ. Therefore, it is important to investigate theoretically the dependence of the tunnel magnetoresistance and the exchange coupling on these factors. This will help us understand the physics of the spin-dependent tunneling.

3.1 Introduction

Since the first observation by Grünberg *et al.*[1] of antiferromagnetic coupling of Fe films separated by Cr spacer, the interlayer exchange coupling between ferromagnetic layers separated by a nonmagnetic layer has been a subject of intense research. The most important stimulus was discovered by Parkin *et al.*,[2] which was the oscillations of the interlayer exchange coupling in Fe/Cr/Fe and Co/Ru/Co multilayers, as a function of the thickness of nonmagnetic layer. Furthermore, Parkin[3] showed that this phenomenon occurs with almost any transition metal as an inserted layer. For the case of metal

spacers, a lot of theoretical studies have been performed to investigate the oscillations of the coupling. Various models have been used to obtain insight to the mechanism of the interlayer coupling. These include the Ruderman-Kittel-Kasuya-Yosida (RKKY) model,[4-6] in which the magnetic layers are treated as arrays of localized spins interacting with conduction electrons by a contact exchange potential; the free-electron model;[7-10] the tight-bonding model[11] and the Anderson model.[12] The simplicity of these models allows one to obtain the analytical results, thus making the physics transparent. The oscillation periods for noble metal spacers have been predicted by RKKY theory and the predictions were found in good quantitative agreement with the numerous experimental observations.[13 - 15] However, due to the drastic idealization of these models, no quantitative predictions about the strength of the coupling for a realistic system have been given so far.

Recently, TMR and the exchange coupling in MTJ composed of two ferromagnetic layers separated by an insulator layer has attracted more attention due to the potential application in read heads and magnetic sensors. Jullière[16] first reported tunnel magnetoresistance measurements on a ferromagnet/insulator/ferromagnet (FM/I/FM) tri-layer junction and put forth a quantitative model showing that tunneling in FM/I/FM junctions should lead to a large tunnel magnetoresistance, which is proportional to the spin polarization of the two FM layers. Slonczewski[17] studied the conductance and the exchange coupling in MTJ based on the free-electron model. He predicted that the tunneling conductance varies with angle θ between the magnetization vectors of the two FM layers. The exchange coupling in his study is obtained through analyzing the charge and spin current through a rectangular barrier in a FM/I/FM structure. The exchange

coupling in an FM/I/FM structure has also been extensively investigated both experimentally[18,19] and theoretically.[20, 21] Most of the previous theoretical work about TMR and the exchange coupling in MTJ treated the thickness of the FM layers to be infinitely large so that the effect of FM layer thickness was neglected. Zhang *et al.* studied the magnetoresistance and the exchange coupling of MTJ with a finite thickness of FM layers,[22] as well as MTJ with nonmagnetic (NM) spacers inserted between the FM layers and the tunnel barrier.[23] They found that both the TMR ratio and the bilinear exchange coupling oscillate with the thickness of the FM layers. In the case of the MTJ with NM spacers, the exchange coupling can even change sign as the NM layer thickness changes due to the formation of quantum well states. These studies were carried out based on the mathematical simplification by approximating the solution to the order of $e^{-\kappa t}$, where $i\kappa$ is the imaginary electron momentum in barrier region and t is the barrier thickness.

Our studies were carried out based on a full numerical calculation without any simplification. First, the TMR and the exchange coupling with finite thickness of FM layers in structure of NM/FM/I/FM/NM will be presented. Second, the interface roughness effect on TMR and the exchange coupling will be discussed based on the same structure. Our simulation work was performed on the basis of Slonczewski's free-electron model. According to Stearns' theory of spin-polarized tunneling between iron-group ferromagnetic metals and superconductors[24], tunneling through Al_2O_3 film barriers originates or terminates in strongly conducting bands which are partially polarized by exchange coupling to weakly conducting strongly polarized 3D bands. Stearns pointed out that the transmission probability depends on the effective mass of electron which is

different for different bands. The localized electrons have a large effective mass and therefore decay very rapidly into the barrier region, whereas the dispersive s-like electrons decay slowly. According to this argument, the nearly free-electron should provide essentially all the tunneling current. Therefore, the free-electron model can provide some useful information for understanding the tunneling occurred in real systems. Several features can be captured by using our model, such as the TMR dependence on barrier properties; TMR dependence on spin polarization of the FM layers and the angular dependence of TMR.

The differences between our one-dimensional model and the real system include: (1) the tunnel barrier in the real system has a very complex band structure, while in our simulation we simplify using a rectangular potential barrier; (2) the electron density of states (DOS) near the interface in the real system depend greatly on the condition of the interfaces between the ferromagnetic layers and the tunnel barrier, while in our simulation the DOS is simply represented by the Fermi wavevector of the FM layers; (3) the ferromagnetic layer has a multiband electronic structure, and the exchange splitting of the electron bands is very complex, while in our model only the free electron bands were taken into account and the exchange splitting of the bands was treated by considering different potentials for spin-up and spin-down electrons; (4) the potential barrier height and the barrier thickness are very sensitive to the interfacial roughness, impurity states in the barrier and other types of disorder whereas we consider the relatively perfect rectangular potential barrier. A brief introduction of the theoretical model used in our studies is given in the next section.

3.2 Theoretical model

TMR and the exchange coupling computations as a function of spin polarization of FM layers, barrier height of the tunnel barrier, the thickness and surface roughness of FM layer are carried out with the basic NM/FM/I/FM/NM structure. The potential for the structure is given in Fig. 3.1. The barrier is a thin insulator.

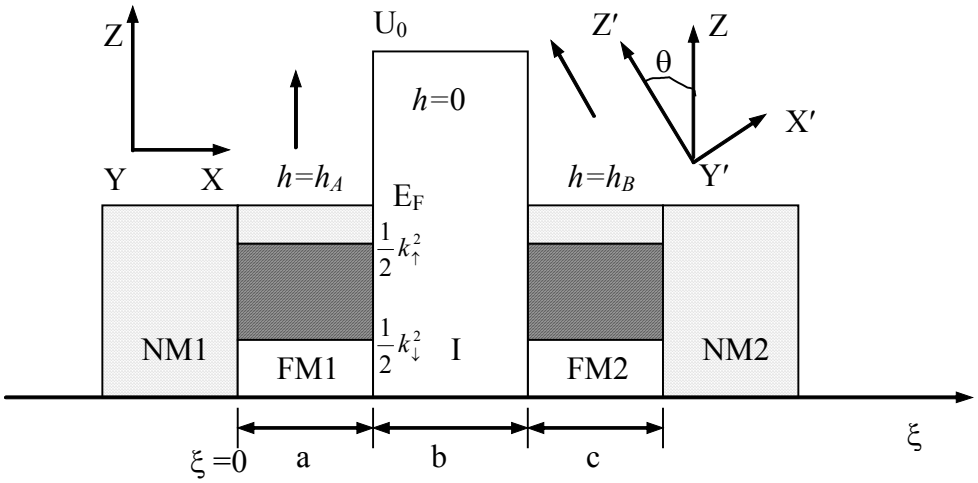

Figure 3.1 Schematic of multilayer structure.

On the basis of a free-electron approximation of the spin-polarized conduction electrons, the longitudinal part of the effective one-electron Hamiltonian (in natural units) may be written as:

$$H_{\xi} = -\frac{1}{2}\left(\frac{d^2}{d\xi^2}\right) + U(\xi) - h(\xi)\cdot\sigma \tag{3.1}$$

where σ is the conventional Pauli spin operator, while

$$U(\xi) = \begin{cases} 0, & in\,both\ NM\ layers \\ V1, & in\,FM1\ layer \\ U_0, & in\,tunnel\,barrier \\ V2, & in\,FM2\ layer \end{cases} \tag{3.2}$$

and

$$h(\xi)=\begin{cases} h_A, & in\ FM1\ layer \\ h_B, & in\ FM2\ layer \\ 0, & otherwise \end{cases} \tag{3.3}$$

where $U(\xi)$ represents the potential with U_0 denoting the barrier height of the classical forbidden insulator region and V_1 and V_2 are the contact potential between the NM/FM1 and FM2/NM, respectively; h_A and h_B are the molecular fields in two magnetic layers. a, b, and c are the thickness of FM1, tunnel barrier and FM2, respectively. The two FM layers are assumed to have identical material properties except when explicitly noted. However, the molecular fields h_A and h_B with the ferromagnetic layers, as well as the corresponding spin quantization axes z and z′, are at angle θ with respect to each other. Shading in Fig. 3.1 indicates that the occupation of the spin-dependent free-electron bands has edges corresponding to the Fermi wave vector $\frac{1}{2}k_\sigma^2$ in the FM layers and 0 in the NM layers. E_F is the Fermi energy. Our simulation model is one dimensional and only the longitudinal component of the momentum is considered whereas the transverse momentum $k_{B//}$ is omitted.

We first consider a spin-up incident plane wave from left to right having a unit incident particle flux in the NM layer. The eigenfunctions of the Hamiltonian with eigenvalue E in all five regions shown in Fig. 3.1 can be expressed as:

$$\begin{aligned}
\varphi_{1\uparrow} &= k^{-1/2}e^{ik\xi} + R_\uparrow e^{-ik\xi} & k &= (2E)^{1/2} \\
\varphi_{1\downarrow} &= R_\downarrow e^{-ikz} & & \\
\varphi_{2\sigma} &= A_{2\sigma}e^{ik_{2\sigma}\xi} + B_{2\sigma}e^{-ik_{2\sigma}\xi} & k_{2\sigma} &= \left[2(E-V1\pm h_A)\right]^{1/2} \\
\varphi_{3\sigma} &= A_{3\sigma}e^{-\gamma(\xi-a)} + B_{3\sigma}e^{\gamma(\xi-a)} & \gamma &= \left[2(U_0-E)\right]^{1/2} \\
\varphi_{4\sigma} &= A_{4\sigma}e^{ik_{4\sigma}(\xi-(a+b))} + B_{4\sigma}e^{-ik_{4\sigma}(\xi-(a+b))} & k_{4\sigma} &= \left[2(E-V2\pm h_B)\right]^{1/2} \\
\varphi_{5\sigma} &= A_{5\sigma}e^{ik(\xi-(a+b+c))} & &
\end{aligned} \tag{3.4}$$

The change in quantization axis at I/FM2 interface requires the spinor transformation:

$$\begin{aligned}\varphi_{3\uparrow} &= \varphi_{4\uparrow}\cos\left(\theta/2\right)+\varphi_{4\downarrow}\sin\left(\theta/2\right)\\ \varphi_{3\downarrow} &= -\varphi_{4\uparrow}\sin\left(\theta/2\right)+\varphi_{4\downarrow}\cos\left(\theta/2\right)\end{aligned} \text{ and } \begin{aligned}\varphi'_{3\uparrow} &= \varphi'_{4\uparrow}\cos\left(\theta/2\right)+\varphi'_{4\downarrow}\sin\left(\theta/2\right)\\ \varphi'_{3\downarrow} &= -\varphi'_{4\uparrow}\sin\left(\theta/2\right)+\varphi'_{4\downarrow}\cos\left(\theta/2\right)\end{aligned} \tag{3.5}$$

where θ is the angle between molecular fields in FM1 and FM2 layers.

Applying the continuity of wave functions and their derivatives at the interfaces, we can work out all the unknown coefficients in the wave functions. The spin transmissivity can be expressed as:

$$T_z = \mathrm{Im}\sum_{\sigma}\sigma\psi_{\sigma}^{*}\left[\frac{d\psi}{d\xi}\right] \tag{3.6}$$

$$T_{+} = T_x + iT_y = i\left[\frac{d\psi_{\uparrow}^{*}}{d\xi}\psi_{\downarrow} - \psi_{\uparrow}^{*}\frac{d\psi_{\downarrow}}{d\xi}\right] \tag{3.7}$$

where T = (T_x, T_y, T_z) is the expected value of Pauli spin transmitted through the plane with give ξ. When the factor σ is removed from the Eq. (3.6), the expression for T_z becomes the conventional particle transmissivity.

$$T_p = \mathrm{Im}\sum_{\sigma}\varphi_{\sigma}^{*}\left(\frac{d\varphi_{\sigma}}{d\xi}\right) \tag{3.8}$$

Therefore, the tunneling transmissivity can be calculated within the classical forbidden region. Our calculation is performed on the basis of zero temperature and small external voltage, so that electrons near the Fermi level carry most of the current. Hence $\gamma(E_{\xi})$ and $k_{\sigma}(E_{\xi})$ are replaced by $\gamma(E_F)$ and $k_{\sigma}(E_F)$ respectively in the calculation. The longitudinal component of k determines the tunneling transmissivity and the transversal component of k will be used to calculate the exchange coupling between two FM layers.

By assuming that the component of k parallel to the plane of the junction and the total energy of the tunneling electron is conserved during the tunneling process,[25] one obtains the conventional expression of conductance

$$G(\theta) = \left(e^2 / 8\pi^2 \hbar\right)\left[\gamma T_p(\theta)/b\right] \tag{3.9}$$

The TMR is calculated according to:

$$TMR = \frac{G(\theta = 0) - G(\theta = \pi)}{G(\theta = 0)} \tag{3.10}$$

The exchange coupling is calculated on the basis of the torque produced by rotation of magnetization of one ferromagnetic layer relative to another. This method actually works by constructing a spin current to calculate the probability that an incident electron will undergo a change of spin states on transmission through the tunnel barrier. For the two-band case, the spin current includes both spin-up and spin-down electrons.

In the case with no external applied voltage, there is no current flowing through the barrier. Assume the spinor rate $d\sigma_A/dt$ combine FM1→FM2 transmission originating from one incident ↑ (z-axis quantization) wave in FM1 with the corresponding FM2→FM1 transmission originating from one ↑ (z′-axis quantization) wave with the same E_ξ in FM2. The spinor rate could be obtained via appropriate transformation connecting frames x, y, z and x′, y′, z′. The spin current due to a spin-up electron of energy E incident from the left FM layer can be expressed as:

$$j_e^{\uparrow} = \frac{1}{2} \cdot \mathrm{Re}\left[\frac{d\varphi_{\uparrow}^{*}}{d\xi}\varphi_{\downarrow} - \varphi_{\uparrow}^{*}\frac{d\varphi_{\downarrow}}{d\xi}\right] \tag{3.11}$$

Similarly, we can obtain the current due to the spin-down electron incident from the left FM layer, $j_e^{\downarrow}$ by applying this equation with $k_{\uparrow}$ and $k_{\downarrow}$ interchanged. The net current j_T is calculated by summing both $j_e^{\uparrow}$ and $j_e^{\downarrow}$ over all occupied states.

For spin-up electron:

$$j^{\uparrow} = 2\sum_{0<k_{\uparrow}<k_0} j_e^{\uparrow} = \int_0^{k_0} \frac{1}{2} \cdot \mathrm{Re}\left[\frac{d\varphi_{\uparrow}^*}{d\xi}\varphi_{\downarrow} - \varphi_{\uparrow}^* \frac{d\varphi_{\downarrow}}{d\xi}\right] dk_{\uparrow} \tag{3.12}$$

where $k_0 = \sqrt{k_{\uparrow}^2 - k_{\downarrow}^2} = 2\sqrt{h}$ (h is the molecular field in FM layers)

For spin-down electron:

$$j^{\downarrow} = 2\sum_{0<k_{\downarrow}<k_F^{\downarrow}} j_e^{\downarrow} = \int_0^{\sqrt{k_F^{\downarrow 2} - k_{\downarrow}^2}} \frac{1}{2} \cdot \mathrm{Re}\left[\frac{d\varphi_{\downarrow}^*}{d\xi}\varphi_{\uparrow} - \varphi_{\downarrow}^* \frac{d\varphi\uparrow}{d\xi}\right] dk_{\downarrow} \tag{3. 13}$$

where $k_F^{\downarrow}$ represented the Fermi wavevecctor of spin-down electrons at the Fermi surface.

Considering the contribution of electrons incident from the right side, the total spin current can be expressed as:

$$j_T = j^{\uparrow} + j^{\downarrow} \tag{3.14}$$

The Heisenberg term of coupling is given by

$$J = -\hbar j_T / \left[2\sin(\theta)\right] \tag{3.15}$$

The TMR ratio and the exchange coupling can thus be calculated by using Eq. (3.10) and Eq. (3.15). The program for the TMR and the exchange coupling calculation will be given in the appendix.

3.3 TMR and exchange coupling in MTJs with finite thickness of FM layers

In Slonczewski's model, the FM layer is taken as infinite so that the effect of the thickness of the FM layer is neglected. In fact, the thickness of FM layers is finite in the practical case and the finite thickness of the FM layers may lead to a dramatic difference from the infinite thickness case. In our simulation work, the NM/FM/I/FM/NM structure with a finite FM layer thickness has been studied. The simulation work investigates the dependence of the TMR and the exchange coupling on the thickness of the FM layer and the tunnel barrier. The relationship between the TMR performance and the exchange coupling is evaluated. At the same time, the spin polarization of FM layers and the barrier height effect on TMR ratio will be presented.

3.3.1 Simulation results and discussion

In this part of the simulations, TMR and the exchange coupling calculations are based upon the tunnel junction structure shown in Fig. 3.1. The FM layers are assumed to be Fe and the respective Fermi wave vectors in Fe are $k_{\uparrow} \approx 1.09$ Å^{-1} and $k_{\downarrow} \approx 0.42$ Å^{-1}, corresponding to $V_1=V_2=0$ and $h_A=h_B=0.25$ eV. The reason we choose Fe as the FM layer is due to the fact that the band structure of Fe has been well established both via the first-principles band calculations and the band-theory analysis of polarization in magnet-to-semiconductor tunneling. The Fermi vectors in Fe have been evaluated by Stearns in the magnet-to-superconductor tunneling experiment.[26]

Figure 3.2 illustrates the FM layer thickness dependence of TMR. The solid line represents the case where the thickness of both FM layers is changed simultaneously and the dashed line corresponds to the case where the thickness of one FM layer is fixed (a=20Å) while the other is varied. The barrier thickness and the barrier height are fixed (U_0=1.2 eV and b=20Å).

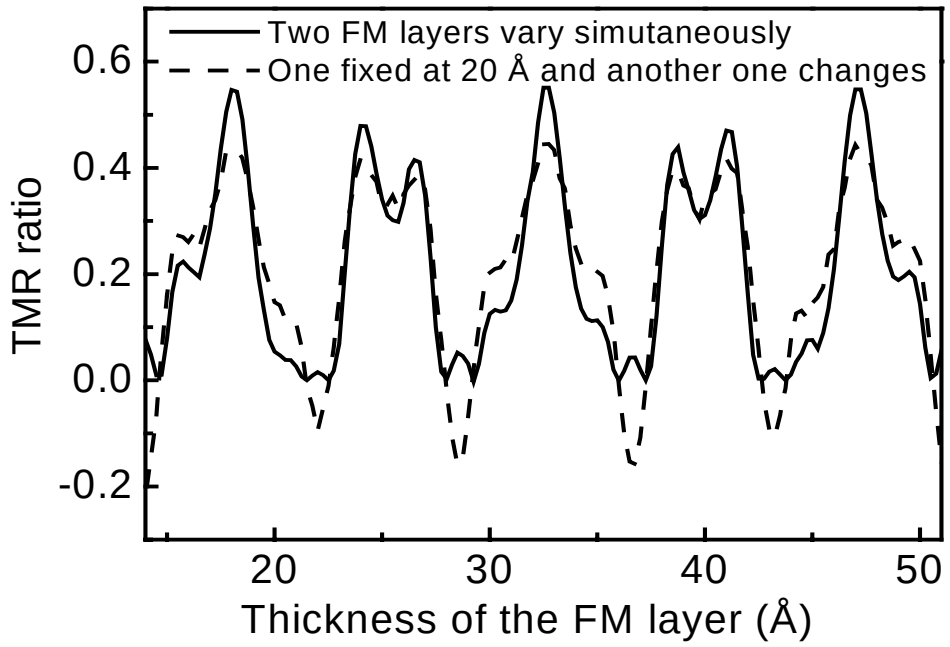

Figure 3.2 TMR as a function of the thickness of FM layers in NM/FM/I/FM/NM junction. Solid line: a and c are changed simultaneously. Dashed line: a=20Å and c is varied.

We find that the TMR oscillates with the thickness of FM layers and the oscillation behavior of the TMR in these two cases is different. Since the TMR depends on the density states of spin up and spin down electrons, the oscillation of the TMR suggests that the density of states of the electrons is a function of the thickness of FM layers. By considering the fact that the thickness of FM layer in our studies is less than the electron mean free path, we attribute the oscillation of TMR to the quantum-size effect induced

asymmetry in density of states of the electrons. It is this asymmetry that leads to the oscillation of the TMR and in certain cases the TMR can even change sign.[22]

We present a comparison between the oscillation behavior of TMR and the exchange coupling with the thickness of the FM layers in Fig. 3.3. It is clearly seen that the TMR and the exchange coupling oscillate with the same period and the maximum value of the TMR correspond to the maximum value of the exchange coupling (ferromagnetic). A theoretical study in magnetic multilayer structures with the nonmagnetic metal spacers has pointed out the oscillations of the exchange coupling and GMR with the spacer thickness are correlated.[27] Our results show that such a correlation also exists in magnetic tunnel junctions with the nonmagnetic insulator spacers.

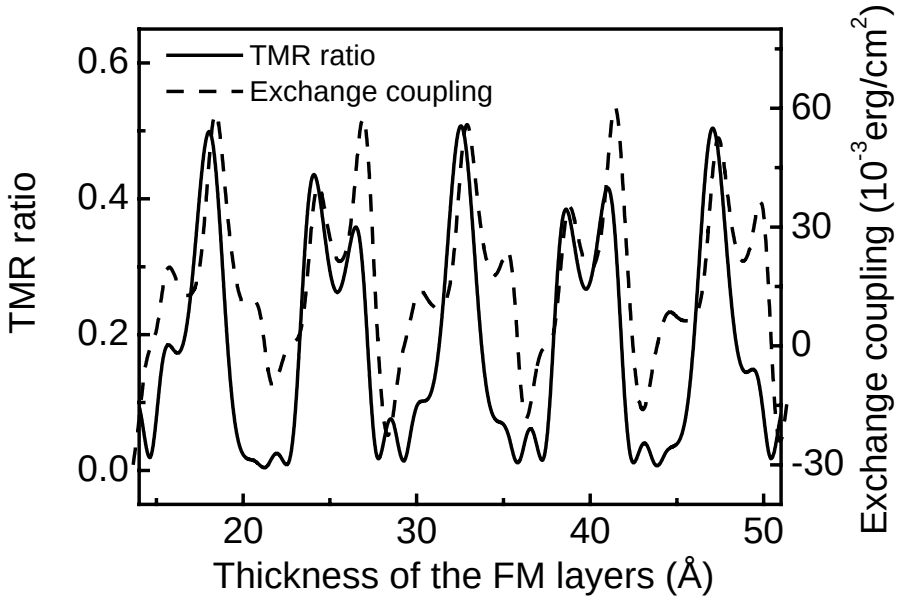

Figure 3.3 TMR and the exchange coupling as a function of the thickness of FM layers (varied simultaneously) in NM/FM/I/FM/NM junction. The thickness of tunnel barrier is 5Å.

It is known that the TMR depends on the relative orientation of the magnetization directions in two FM layers. The TMR varies with the angle θ between the magnetization vectors of two FM layers. The angular dependence of TMR with different barrier heights

in NM/FM/I/FM/NM junction with b=20Å and a=c=50Å is shown in Fig. 3.4. The change of TMR with θ is similar in trend to that in FM/I/FM with infinitely thick FM layers. The result is consistent with the experimental measurements of Moodera *et al*.[28] Comparison of the TMR ratio of junctions with different barrier heights shows that the TMR ratio increases as the barrier height increases, which is consistent with the experimental results.[29]

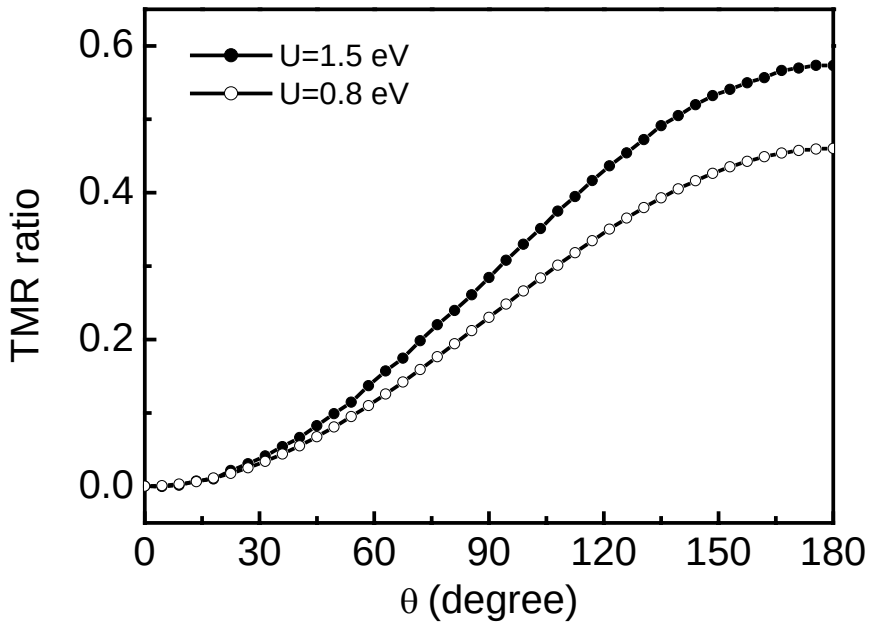

Figure 3.4 The angular dependence of TMR with different barrier height in NM/Fe/I/Fe/NM junction.

The TMR of NM/FM/I/FM/NM junction as a function of the effective spin polarization of the FM layers is illustrated in Fig. 3.5. The calculation of TMR is performed with the barrier thickness b=20Å and the thickness of two FM layers varies simultaneously. The effective spin polarization of FM layers is calculated based on Slonczewski's model.

$$P_{eff} = \frac{\left(k_{\uparrow} - k_{\downarrow}\right)}{\left(k_{\uparrow} + k_{\downarrow}\right)} \cdot \frac{\left(\kappa^2 - k_{\uparrow}k_{\downarrow}\right)}{\left(\kappa^2 + k_{\uparrow}k_{\downarrow}\right)} \tag{3.16}$$

The first factor in the formula represents the fractional spin polarization of the state densities of spin-up and spin-down electrons at the Fermi energy of the FM layer in the free-electron approximation. The interfacial second factor in the formula is introduced by considering the spin direction dependence of the penetration of electrons from the FM layer to the barrier, where $i\kappa$ is the imaginary electron momentum in barrier region. We find that the maximal value of TMR is dependent on the spin polarization of FM layers. Higher spin polarization results in a higher TMR maximum. The fact is in agreement with Jullière's model.

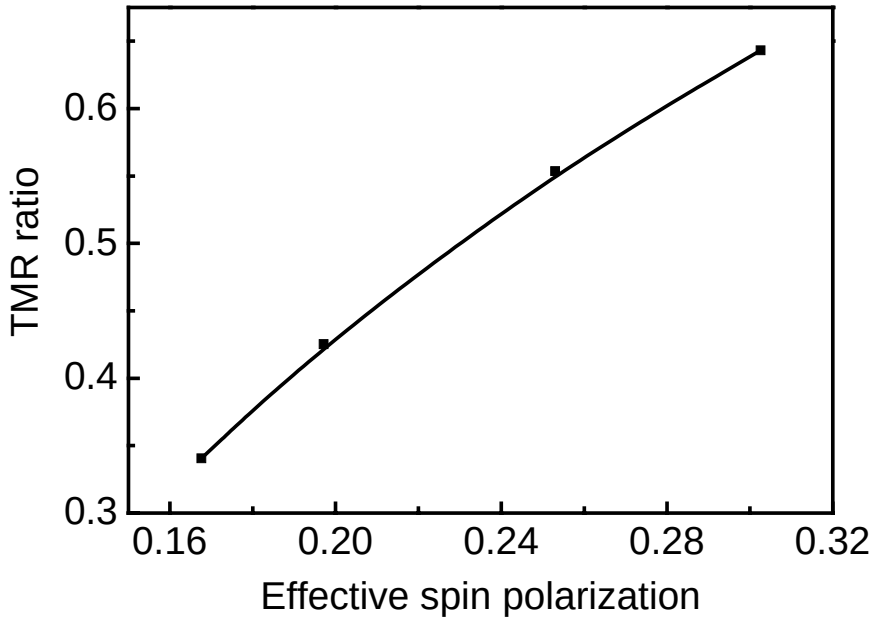

Figure 3.5 The spin polarization dependence of TMR.

The effect of the thickness of the tunnel barrier on the exchange coupling of the NM/FM/I/FM/NM junction is illustrated in Fig. 3.6. From the curve we can see that the exchange coupling decays rapidly and reaches to a very low level as the thickness of the tunnel barrier increases within a small region. According to the definition of the exchange

coupling energy from Nèel,[30] the exchange coupling energy decays exponentially with the thickness of the spacer. Our results are consistent with previous theoretical work.

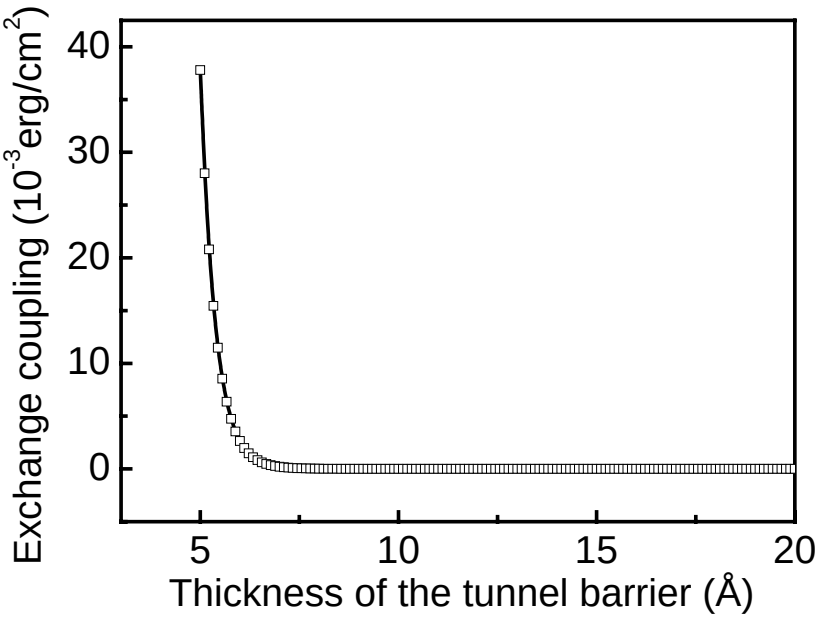

Figure 3.6 The tunnel barrier thickness dependence of exchange coupling.

From the simulation results obtained above, we find that the oscillation period, phase and amplitude of the TMR are directly related to the Fermi wave vectors. From the formula (3.4), the wave vectors are determined by E_F, V_1, V_2, h_A *and* h_B. For a given magnetic material, the Fermi wave vectors are mainly determined by the contact potential between NM, FM and insulator layers.

Figure 3.7 shows the TMR as a function of the thickness of the FM layers, which vary simultaneously, in NM/FM/I/FM/NM junctions with different Fermi wave vectors. The solid line corresponds to V_1=V_2=0, whereas the dashed and dotted lines correspond to V_1=V_2=0.03 and 0.06 eV respectively. The results indicate that the period, phase and magnitude of the TMR can be varied by changing the Fermi wave vectors, thus suggesting a way to obtain large TMR in MTJ.

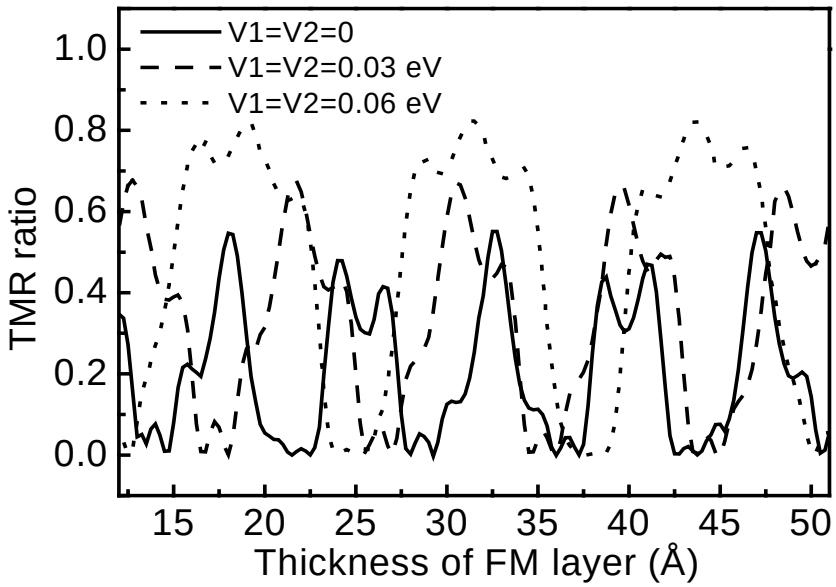

Figure 3.7 TMR as a function of the thickness of two FM layers and different Fermi wave vectors

In real systems, the Fermi wavevector of a transition metal can be controlled by doping paramagnetic elements into the transition metal to form an alloy. It also depends on the interface condition in a multilayer structure, crystalline structure, interface roughness, etc.

3.4 Surface roughness effect on TMR and exchange coupling in MTJs

The surface roughness of the bottom FM layer is one of the key issues in MTJ. It can lead to exchange coupling between the bottom and top FM layers, thus making the independent switching of the magnetizations of the two magnetic layers difficult. Therefore, it is worthwhile to investigate the effect of surface roughness on the performance of MTJs, especially on the exchange coupling in MTJ. This part of our work will concentrate on the bottom FM layer surface roughness effect on TMR and the exchange coupling in MTJs. In a real situation, the state of the interface roughness of thin films is more complicated. For simplicity, we use a sinusoidal function to represent the

states of interfacial roughness. According to Néel's theory,[30] the interface roughness could be described by a sinusoidal function with amplitude h and wavelength λ as two independent parameters. The coupling energy J between two ferromagnetic films could be represented by equation:

$$J = \frac{\pi^2}{\sqrt{2}} \frac{h^2}{\lambda} (\mu_0 MM') \exp\left(\frac{-2\pi t\sqrt{2}}{\lambda} \right) \tag{3.17}$$

where M and M′ are the saturation magnetizations of two FM layers and t is the barrier thickness.

Figure 3.8 gives the interface of MTJ with the basic structure of the type NM/FM/I/FM/NM. I1~I4 represent all the interfaces in the multi-layer structure. The potential of this basic structure is the same as that in section 3.1, the only difference being that the interface between NM, FM and Insulator are treated as perfect there. Here we introduce a sinusoidal function to represent the interface between FM layer and Insulator layer. The thickness of FM layers and insulator layer are determined by the interface.

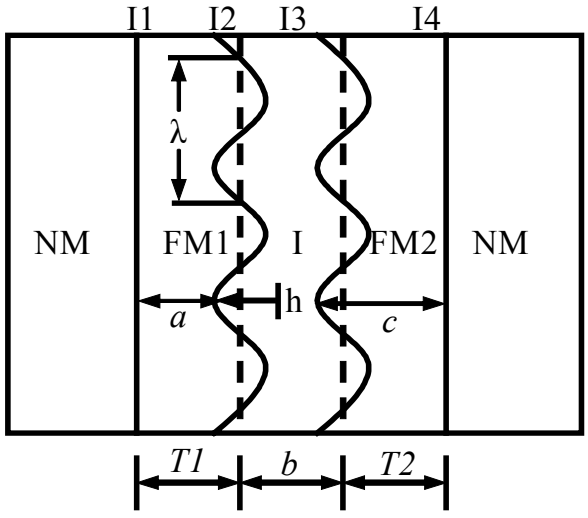

Figure 3.8 Interface configurations of MTJ with the structure of NM/FM/I/FM/NM.

It can be seen from Fig. 3.8 that the thickness of two FM layers at any location is $a = T1 - h * \sin 2\pi x/\lambda$ and $c = T2 + h * \sin 2\pi x/\lambda$, where h is the roughness amplitude and λ is the roughness wavelength. The thickness of the tunnel barrier b is constant in this case. T1 and T2 are the thickness of two FM layers when there is no interface roughness introduced.

It is known that the interfacial scattering occurs when the interface becomes rougher. The scattering will modify the wave vectors of the incident electrons. In our simulation work, the interfacial roughness induced exchange coupling energy is introduced into the equation 3.1 as a small perturbation. Therefore, the Fermi wave vectors of the FM layers will vary accordingly, thus affect the behavior of the TMR and the exchange coupling. Besides the variation of the Fermi wave vectors, the thickness of the two FM layers will be changed accordingly. Due to the periodical properties of the sinusoidal function, we just need to perform our calculation in the region where the angle of the sinusoidal function varied from -π/4 to π/4. We take 10 points for each case (step = π/20) and the TMR and the exchange coupling are calculated accordingly.

3.4.1 Simulation results and discussion

Figure 3.9 gives the surface roughness effect on TMR and the exchange coupling of multi-layer structure with the basic structure shown in Fig. 3.8. The parameters used in the calculation are as follows: the barrier height and the barrier thickness are U_0=1.2 eV and 10 Å, respectively. V_1=V_2=0; h_A=h_B=0.25 eV. The amplitude and wavelength of the interfacial roughness are h=5 Å and λ=90 nm, respectively.

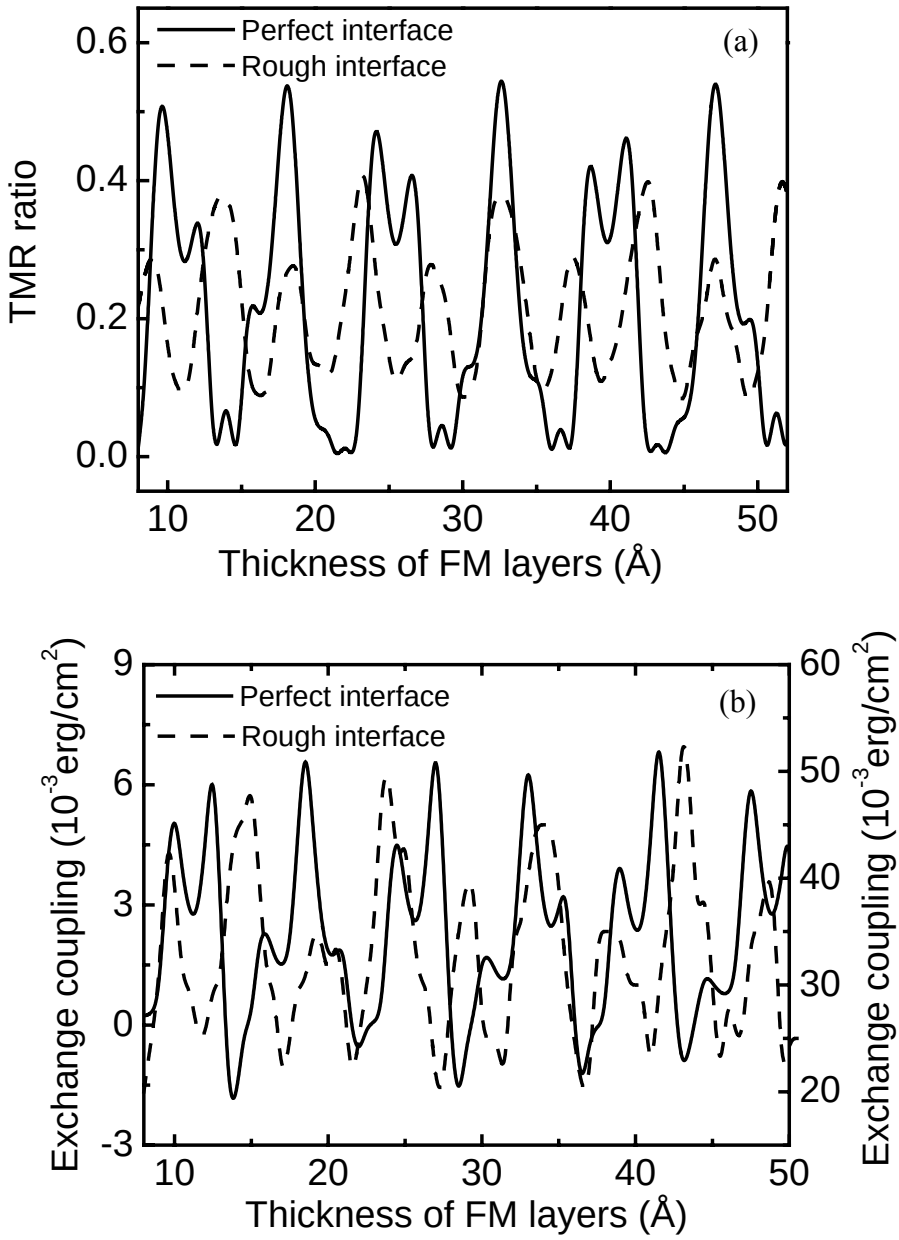

Figure 3.9 Interface roughness effects on (a) TMR; and (b) the exchange coupling.

We can see from Fig. 3.9 (a) that the TMR ratio changes periodically as the thickness of one FM layer is changed. The solid line in Fig. 3.9 (a) is for the case with perfect interfaces, while the dashed line represents the case with rough interfaces. After introducing the interface roughness, both the value and the period of the TMR ratio dependence on thickness of FM layer are changed. The TMR became more sensitive to

the thickness of the FM layer in the case of the multi-layer structure with rough interface. The rough interface may induce spin-flip scattering, therefore some of the majority electrons will change their spin direction and tunnel into the corresponding minority states. This causes a decay in the distribution asymmetry of density of states, resulting in a decrease of the TMR ratio. This only provides a qualitative explanation, since the model used in our studies does not provide enough information to predict the effect of the interface roughness on the density of states. The difference of the oscillation period is due to the interfacial scattering induced variation of the Fermi wave vectors in two FM layers.

Fig. 3.9 (b) gives the corresponding exchange coupling dependence on the interface roughness states in the multi-layer structure. The solid line represents the exchange coupling of the multi-layer structure with perfect interface while the dash line shows the case with interface roughness. The amplitude of the exchange coupling increases as the interface becomes rough. If we compare the TMR ratio and the exchange coupling of the multi-layer structure with the interface roughness, it is found that the TMR and the exchange coupling are not correlated to each other as that observed in junction with prefect interfaces. The variation is due to the interfacial roughness induced spin scattering destroying the coherence of the spin electrons during the tunneling process.

Figure 3.10 shows the exchange coupling as a function of the interface roughness amplitude. The intensity of the exchange coupling increases as the interface roughness amplitude h changes from 1 Å to 6 Å. The thickness of the tunnel barrier is 10 Å and the roughness wavelength is 90 nm in this case. It can be seen from Fig. 3.9 that the exchange coupling increases as the interfacial roughness increases.

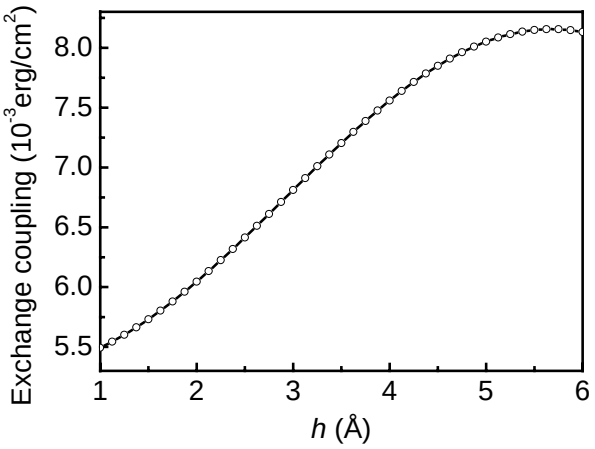

Figure 3.10 The exchange coupling as a function of the interface roughness amplitude.

The dependency of the exchange coupling on the roughness wavelength is shown in Fig. 3.11. The interface roughness amplitude h for this calculation is 5 Å and the roughness wavelength λ changes from 90 Å to 270 Å. It can be seen that the value of the exchange coupling decreases almost linearly as the λ increases.

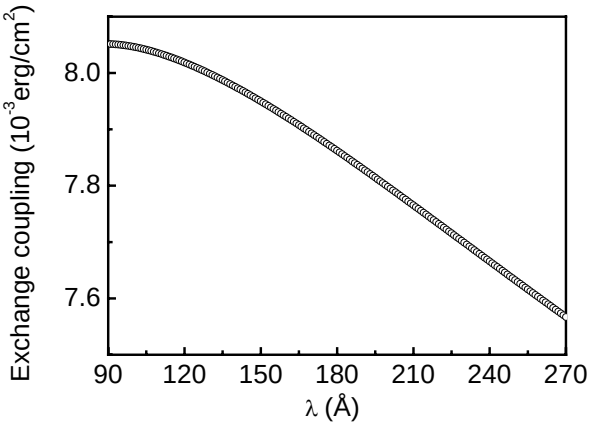

Figure 3.11 The exchange coupling as a function of the interface roughness wavelength.

The exchange coupling as a function of the amplitude and wavelength of the interfacial roughness could be understood based on equation 3.17. The exchange coupling energy will increase (decrease) as the amplitude (wavelength) of the interfacial roughness increases.

3.5 Summary

Based on the free-electron model, the TMR and the exchange coupling as the function of several parameters such as the thickness of the tunnel barrier, the thickness of the FM layers, the spin polarization of two FM layers, the Fermi wave vectors of two FM layers and the interfacial roughness, were investigated theoretically.

For MTJ stacks with finite thickness of two FM layers, both TMR and the exchange coupling oscillated periodically with the thickness of the ferromagnetic layer. The TMR and the exchange coupling were correlated to each other and the maximum TMR occurred when ferromagnetic the exchange coupling between two ferromagnetic layers reached the maximum value.

Our simulation results show that the maximum value of TMR achieved depends on the spin polarization of two FM layers. The exchange coupling demonstrates an exponential dependence on the thickness of the tunnel barrier. All these results agree with previous theoretical works.

The oscillation period of the TMR and the exchange coupling is found to be a function of the Fermi wave vectors of two FM layers. Our results suggest that the interfacial contact potential between the FM layer and the nonmagnetic metal contact layer may affect the performance of the MTJ devices.

Compared with the structure with no interface roughness, TMR ratio decreased and the exchange coupling increased as the interface roughness was introduced. The oscillation period of the TMR and the exchange coupling in the structure with interfacial roughness is different from that in the structure with perfect interfaces. The decrease of the TMR with a rough FM layer is attributed to the decrease of spin polarization of FM

layers, which results from the spin scattering induced decay of the distribution asymmetry of density of states in FM layers. The increase of the exchange coupling may be attributed to the interfacial roughness induced the exchange coupling between two FM layers via the insulator spacer. The difference of the oscillation period of the TMR and the exchange coupling is attributed to the variation of the Fermi wave vectors induced by the interfacial scattering of the electrons.

It had been shown in our study that the TMR ratio and the exchange coupling depend on the properties of the FM layers (spin polarization, thickness and Fermi wave vectors) and the tunnel barrier (barrier height and thickness). It is worthwhile to discuss the effect of these parameters on TMR and exchange coupling.

The effect of the spin polarization on TMR and exchange coupling is quite straight forward, according to both Julliere and Slonczewski's theory, higher spin polarization results in higher TMR ratio. Our simulation results show that the maximum TMR ratio obtained increases as the increase of the spin polarization, which is consistent with both theories.

As to the effect of the Fermi wave vectors, on one hand, the variation of the Fermi wave vectors will change the propagation of the electrons and the wave function as well. On the other hand, it can be clearly seen from the Eq. 3.16 that the values of the Fermi wave vectors determine the spin polarization of the electrons in FM layers. That is to say, Fermi wave vectors affect the TMR and the exchange coupling via varying wave function and the spin polarization of the electrons.

In our study, TMR ratio and the exchange coupling show oscillation with the variation of the FM layer thickness. Since the reflection of the free-electron waves will

occur at the FM/I interface, in the case of a FM layer with finite thickness, the reflection coefficients in Eq. (3.4) is determined by all the waves associated with the multiple reflections inside the FM layer. In the other words, the coefficients of the wave functions of the electrons become a function of the FM layer thickness. Thus, we can observe oscillations of the TMR versus FM layer thickness. The oscillation is due to the quantum interferences inside the FM layers. When the thickness of the FM varies, the interferences can be either constructive or destructive, the magnitude of the TMR ratio and the exchange coupling will change accordingly. Moreover, in the oscillation the TMR can change the sign if two FM layers are not identical in thickness, that is to say, the quantum-size effect can also result in the inverse TMR.

The quality of the tunnel barrier affects the magnitude and stability of the MR effect, the junction resistance and the interlayer exchange coupling. In our study, the exchange coupling showed an exponential decay as the barrier thickness increases, while the TMR ratio does not show such dependence. As the increase of the barrier thickness, the transmission possibility of the electrons from one FM layer to another decays exponentially. Since the exchange coupling originates from the sum of the interactions of electrons between two FM layers, a rapid decrease of exchange coupling is observed. However, the TMR is determined by the relative variation of the resistance when the alignment of the magnetization directions in two FM layers changes. Although the transmission possibility of the electrons for both parallel and antiparallel alignment decays, the relative variation of the resistance does not change too much.

The effects of the barrier height on TMR ratio and the exchange coupling are mainly reflected from their influences on the spin polarization of the tunneling electrons,

as expressed in Eq. 3.16. If we assume the electron momentum parallel to the junction is conserved in tunneling. The polarization of the tunneling electrons now depends on the barrier height through an imaginary wave vector $i\kappa$ in the barrier defined by:

$$\hbar\kappa = [2m(U_0 - E)]^{1/2} \tag{3.18}$$

here, the $k^{\uparrow}$, $k^{\downarrow}$ are the Fermi wave vectors in the spin up and spin down bands. For parabolic bands used in our study, $k^{\uparrow} \propto D^{\uparrow}(E_F)$, $k^{\downarrow} \propto D^{\downarrow}(E_F)$, it is easy to see that the first factor, $(k^{\uparrow} - k^{\downarrow})/(k^{\uparrow} + k^{\downarrow})$, is the polarization obtained in the classical theory of tunneling. Since the κ ranges from 0 (low barrier) to ∞ (high barrier), it follows that, for a high barrier, the spin polarization P is reduces to classical theory but P can even change sign when the barrier height is low.

In our simulation work, TMR and the exchange coupling were investigated within a free-electron model by assuming a rectangular potential barrier for tunneling. Although the free-electron model captures some important features of SDT, they cannot be used for the quantitative description of TMR and the exchange coupling. In particular, results of the free-electron consideration are very sensitive to the profile of the potential barrier. Moreover, the free electron model ignores the multi-band electronic structure of the ferromagnetic electrodes and the ferromagnet/insulator interfaces. Finally, the free-electron model does not take into account the complex band structure of the insulator. Therefore, our simulation has limitations on quantitatively evaluating the TMR and the exchange coupling. The comparison of the important features of spin-dependent tunneling between the free-electron model and a real system, with the corresponding limitations, is given in the table 3.1.

Table 3.1 Comparison of our simulation model and a real system.

Real system	Our model	Comments and Limitations
The tunnel probability of electron depends on barrier properties and the interface conditions of barrier and FM layers.	The tunnel magnetoresistance (TMR) depends on the barrier height and thickness.	The complex band structure of the tunnel barrier, the impurity and other types of disorder in the tunnel barrier were not taken into account in our model.
The tunnel magnetoresistance (TMR) depends on the spin polarization of the FM layers. Higher spin polarization normally result in higher TMR.	The TMR depends on the spin polarization of two FM layers, higher spin polarization resulting in higher TMR.	Simulations are consistent with experimental results.[31]
The TMR depends on the relative orientation of the magnetizations in two FM layers.	The dependence of the TMR on relative orientation of the magnetizations in two FM layers in our simulations was consistent with the experimental results.	Simulations are consistent with experimental results.[28,32]
The spin polarization of FM layers depends on the type of materials and interface conditions of the FM layer and tunnel barrier.	The spin polarization of FM layer and the TMR are not determined by characteristics of FM material alone, they also depend on the properties of the tunnel barrier.	The dependence of the spin polarization of FM layer on tunnel barrier is more complex in the real system. In some cases, the spin polarization can even change the sign, which has been observed experimentally.[33] The interactions between FM layer and barrier were not taken into account in our simulation.
The TMR depends on the temperature and the voltage applied during the measurements.	Our simulations were carried out based on zero temperature and very small external voltage.	The dependence of TMR on the temperature and the voltage was not evaluated in our simulations.

In order to reach the quantitative evaluation about the TMR and the exchange coupling, a more accurate description of the electronic structure of the entire MTJ should be used. Nevertheless, our simulation has highlighted the important effects that surface roughness may induce in a MTJ system.

[1] P. Grünberg, R. Schreiber, Y. Pang, M. B. Brodsky, and H. Sowers, *Phys. Rev. Lett.* **57**, 2442 (1986).

[2] S. S. P. Parkin, N. More, and K. P. Roche, *Phys. Rev. Lett.* **64**, 2304 (1990).

[3] S. S. P. Parkin, *Phys. Rev. Lett.* **67**, 3598 (1991).

[4] Y. Yafet, *Phys. Rev. B* **36**, 3948 (1987).

[5] P. Bruno and C. Chappert, *Phys. Rev. Lett.* **67**, 1602 (1991).

[6] R. Coehoorn, *Phys. Rev. B* **44**, 9331 (1991).

[7] J. Barnaś, *J. Magn. Magn. Mater.* **111**, L215 (1992).

[8] R. P. Erickson, K. B. Hathaway, and J. R. Cullen, *Phys. Rev. B* **47**, 2626 (1993).

[9] J. C. Slonczewski, *J. Magn. Magn. Mater.* **126**, 374 (1993).

[10] E. Bruno and B. L. Gyorffy, *Phys. Rev. Lett.* **71**, 181 (1993).

[11] D. M. Edwards, J. Mathon, R. B. Muniz, and M. S, Phan, *Phys. Rev. Lett.* **67**, 493 (1991).

[12] Y. Wang, P. M. Levy, and J. L. Fry, *Phys. Rev. Lett.* **65**, 2732 (1990).

[13] A. Fuss, S. Demokritov, P. Grünberg, and W. Zinn, *J. Magn. Magn. Mater.* **103**, L221 (1992).

[14] M. T. Johnson, S. T. Purcell, N. W. E. McGee, R. Coehoorn, J. aan de Stegge, and W. Hoving, *Phys. Rev. Lett.* **68**, 2688 (1992).

[15] J. Unguris, R. J. Celotta, and D. T. Pierce, *J. Magn. Magn. Mater.* **127**, 205 (1993).

[16] M. Jullière, *Phys. Lett.* **54A**, 225 (1975).

[17] J. C. Slonczewski, *Phys. Rev. B* **39**, 6995 (1989).

[18] S. Toscano, B. Briner, H. Hipster, and M. Landolt, *J. Magn. Magn. Mater.* **114**, L6 (1992).

[19] B. Briner, U. Ramsperger, and M. Landolt, *Phys. Rev. B* **51**, 7303 (1995).

[20] P. Bruno, *Phys. Rev. B* **52**, 411 (1995).

[21] Z. P. Shi, P. M. Levy, and J. L. Fry, *Europhys. Lett.* **26**, 473 (1994).

[22] X. D. Zhang, B. Z. Li, W. S. Zhang, *Phys. Rev. B* **57**, 1090 (1998).

[23] A. Vedyayev, N. Ryzhanova, C. Lacroix, L. Giacomoni, and B. Dieny, *Europhys. Lett.* **39**, 219 (1997).

[24] E. L. Wolf, *Principles of electronic tunneling spectroscopy*, Oxford University Press, New York, 1985.

[25] A. B. Duke, Tunneling in solids, in: E. Burstein, S. Lundquist (Eds.), *Tunneling Phenomena in Solids*, Plenum, New York, 1969.

[26] M. B. Stearns, *J. Magn. Magn. Mater.* **5**, 167 (1977).

[27] J. Barnas and Y. Bruynseraede, *Phys. Rev. B.* **53**, R2956 (1977).

[28] J. S. Moodera and L. R. Kinder, *J. Appl. Phys.* **79**, 4274 (1996).

[29] N. Tezuka and T. Miyazaki, *J. Appl. Phys.* **79**, 6262 (1996).

[30] L. Nèel, C. R. Acad. *Sci. A* **122**, 521 (1963).

[31] R. C. Sousa, J. J. Sun, V. Soares, and P. P. Freitas, *Appl. Phys. Lett.* **73**, 3288 (1998).

[32] H. Jaffre`s, D. Lacour, and F. Nguyen Van Dau, *Phys. Rev. B* **64**, 064427 (2001).

[33] J. M. de Teresa, A. Barthelemy, A. Fert, and J. P. Contour, *Phys. Rev. Lett.* **82**, 4288 (1999).

Chapter 4

Experimental Techniques

In this chapter, a brief introduction of some technologies used in our experimental studies will be given. These technologies include thin film deposition, vibrating sample magnetometer (VSM), atomic force microscope (AFM) and four-probe measurement setup.

4.1 Thin film deposition technologies

The basic structure of MTJs consists of ferromagnetic and insulating thin films. Thin film deposition is very important in our experimental part of work.

Thin film deposition is normally composed of three steps: (1) selection of the appropriate species of materials one would like to deposit; (2) transport of these species to the substrate (usually in a vacuum); and (3) condensation and growth of thin film on the substrate. The properties of the deposited films significantly depend on the deposition conditions such as deposition rate, substrate temperature, substrate materials, deposition atmosphere, and so on. In order to investigate the thin film materials, it is worthwhile to measure the different thin film properties. Generally, the chemical composition, crystalline structure, optical properties, electrical properties, and mechanical properties are evaluated. Figure 4.1 below gives the conceptual correlation between growth conditions and the properties of the resultant thin films.

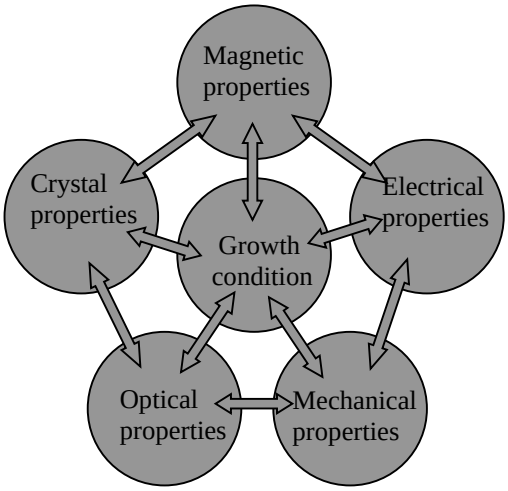

Figure 4.1 Conceptual correlation between growth condition and thin film properties.

The most common deposition methods can be classified as the chemical vapor deposition (CVD) and the physical vapor deposition (PVD) process. In our studies, we mainly use the PVD process. The PVD process is divided into two categories: (1) thermal evaporation and (2) sputtering.[1]

Thermal evaporation process requires the evaporation of source materials in a high vacuum chamber so that the vapor can be condensed on the substrate. It is conventionally called “vacuum deposition” and includes Molecular beam epitaxy (MBE), laser deposition, electron beam melting and resistive heating technologies.[2] These techniques are performed typically under high (10^{-6} Torr) to ultrahigh (10^{-9} Torr) vacuum. Sputtering is a phenomenon that when a solid surface is bombarded with energetic particles such as accelerated ions, surface atoms of the solid are scattered backward due to collisions between the surface atoms and the energetic particles.[3-5] The sputtering is performed under moderate to low vacuum (10^{-4} to 10^{-1} Torr). Apart from the film deposition, sputtering is also valuable for etching patterns, obtaining depth profiles by surface analysis techniques or surface preparation for study.

In some instances, sputter deposition has some advantages compared to evaporation. First, the kinetic energy of sputtered particles is much higher than the typical evaporated particles. Therefore, the sputtered particles have a higher surface mobility during the condensing process and this consequently is helpful to obtain dense, smooth and conformal film morphologies. Second, sputtering has a relatively large source area, which aids to achieve uniform film thickness and conformable coverage. Finally, under similar conditions the difference of sputter yields for various metals is normally less than a factor of 10. However, in the case of the evaporation, the vapor pressures of different metals can vary by many orders of magnitude at the same source temperature. In order to know more about the sputter deposition, a brief introduction will be given in the next section.

4.1.1 Sputter deposition

There are numerous variants of sputter deposition in use today. They can be classified as DC diode, RF diode, Magnetron, and Ion beam deposition. Various sputter systems may have different sputtering configuration, geometry, target type, substrate position, and gas type or gas pressure. The basic sputtering process is the same for all these systems, but the differences of the design will result in different fluxes and energies of sputtered particles and other atomic and/or ion species impacting the substrate.

In order to master the sputter deposition system, the understanding of glow discharge is very important, since all energetic incident particles originate in the plasma (generated in a self-sustained glow discharge that is created by the breakdown of an inert gas such as argon). There are several factors that influence the operation of a glow

discharge for sputter deposition of thin film. We will give a more detailed description of these factors below.

Pressure

In order to maintain the discharge, the working gas pressure cannot go below a certain value. With this precondition, the discharge current and the number of working gas ions increase but their energies decrease, as the working gas pressure increases. Since the sputter yield increases with the number of ions and ion energy, the total number of atoms ejected from the target will depend on the working pressure. When the pressure is low, the mean free path between collisions is large compared to the sputtered atom to substrate distance. At higher pressures, the sputtered atoms have a relative small mean free path. Therefore, they suffer more collisions as they move from the target to the substrate. The sputtered atoms are scattered and arrive at the substrate from all directions by diffusion. As a result of the diffuse nature of material transport, the atoms at high working pressure deposit at places not necessarily in the line of sight of the target.

Power

Power is one of the key parameters in the sputtering process, since the deposition rate is proportional to the ion current incident on the target. For a constant voltage, the deposition rate is therefore proportional to the input power. The sputter power induced deposition rate difference can even affect the growth and the surface morphology of thin films.

Cathode

In order to obtain a uniform deposition thickness, the area of cathode (target) must be much larger than the area of anode (substrate) and the separation distance must be a small

fraction of the anode diameter. The cathode materials can be in various forms, such as a plate, cylinder, or foil, and can be electroplated onto a suitable target support material. Because of intense ion bombardment during the sputtering process, the working gas ions will transfer part of their energies to the cathode, leading to the temperature increase of the cathode. The temperature usually increases rapidly and finally will approach an equilibrium value.[2] Both the rate of temperature rise and the maximum temperature attained depend on the power dissipated at the cathode, the thermal characteristics (thermal conductivity and emissivity) of the target, cooling system and the gas pressure.[2]

Contamination

Even if a sputtering system is initially pumped down to a low pressure and then a sputtering gas of high purity is introduced, contamination may still result from out-gassing as a result of plasma discharge heating of chamber walls. In some of the sputter systems, the contamination can also come from the sputtering process performed on nearby targets due to the poor design of the targets configuration.

Among different sputtering systems, the simplest model is the dc diode sputtering system. The dc sputtering system is composed of a pair of planar electrodes. One of the electrodes is cold cathode and the other is anode. The front surface of the cathode is covered with target materials to be deposited. The substrates are placed on the anode. The sputtering chamber is filled in working gas, typically Ar gas at certain pressure. The glow discharge is maintained under the application of dc voltage between the electrodes. In the dc sputtering system the target is composed of metal, since dc current must flow to maintain the glow discharge between the metallic electrodes.

In the case of sputtering, an insulator target in the dc sputtering system does not work. The sputtering discharge cannot be sustained because of the build-up of a surface charge of positive ions on the front side of the insulator. In order to sustain the glow discharge with the insulator target, an rf-voltage is supplied to the target. This is called rf-diode sputtering. In this type of sputtering system, the thin films of an insulator are directly deposited from the insulator target.

Magnetron sputtering is now extensively used in industry and research institutes. In the experimental part of this work, we use the magnetron sputtering to deposit the thin films. In the following section we will give a detailed introduction of the magnetron sputtering technique.

4.1.2 Magnetron sputtering

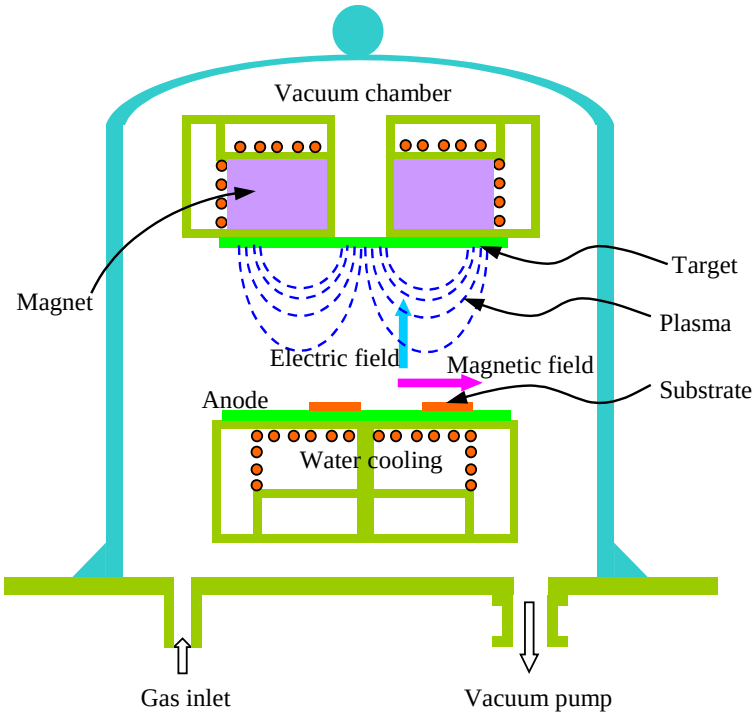

Figure 4.2 Schematic configuration of magnetron sputtering system.

Figure 4.2 gives the schematic configuration of a magnetron sputter system. Compared to the conventional diode sputter system, there is an applied magnetic field parallel to the target surface in a magnetron sputter system (the magnetic field is normally perpendicular to the electrical field). Therefore, the electrons in the glow discharge show cycloidal motion and the center of the orbit drifts along the direction of $E \times B$, where E and B denote the electric field and magnetic field, respectively. The magnetic field is oriented such that drift paths for electrons form a closed loop near the target surface. This electron trapping effect increases the collision rate between the electrons and the working gas molecules. Since the impact efficiency of the available electrons with the working gas is increased, this enables one to maintain a glow discharge at a lower working gas pressure. The magnetic field in a magnetron sputter system increases the plasma density, which leads to an increase of the current density at the target, thus effectively increasing the sputtering rate at the target. The geometry of a simple circular planar magnetron sputtering system is similar to DC and RF diode sputtering systems, but the applied magnetic field makes its behavior quite different.[4]

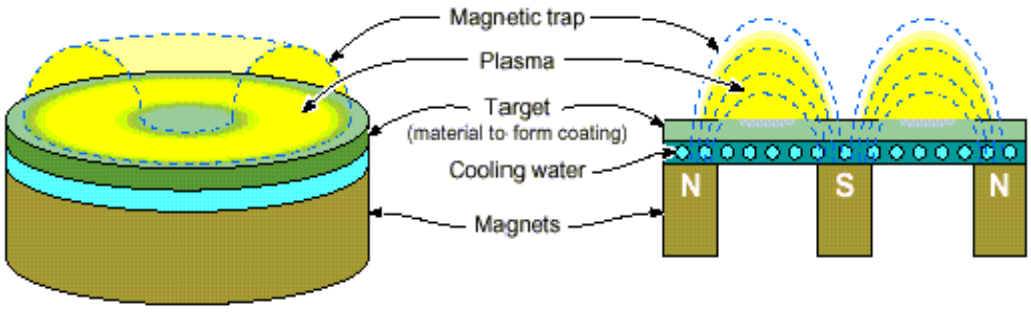

Figure 4.3 Arrangement of target and magnets for a magnetron sputtering system.

A magnetron, consisting of a plate of target with magnets arranged behind it which create a magnetic trap for the plasma electrons, is shown in Figure 4.3. As we mentioned before,

the sputtering process leads to the heating of the target, so the magnetron usually incorporates channels for water-cooling it during operation. A magnetron sputtering system can operate at pressures of around 1mTorr,[4] more typically in the few milli-Torr range. Because of the higher ionization and plasma densities, higher deposition rates are therefore possible in a magnetron sputtering system than in a diode system.[4] When magnetron sputtering sources are used for magnetic material targets, the magnetic field lines are confined within the target materials unless very thin targets are used where magnetic saturation of the target can be achieved. In this case, normally a relatively strong magnetic field will be used. In a magnetron sputtering system, obtaining a uniform magnetic field over a large or complex surface is difficult and usually results in a non-uniform plasma density which causes non-uniform target erosion.

4.2 Magnetic characterization: The vibrating sample magnetometer

The vibrating sample magnetometer (VSM) is a basic instrument for characterizing magnetic materials. Figure 4.4 gives a schematic of the VSM.[6]

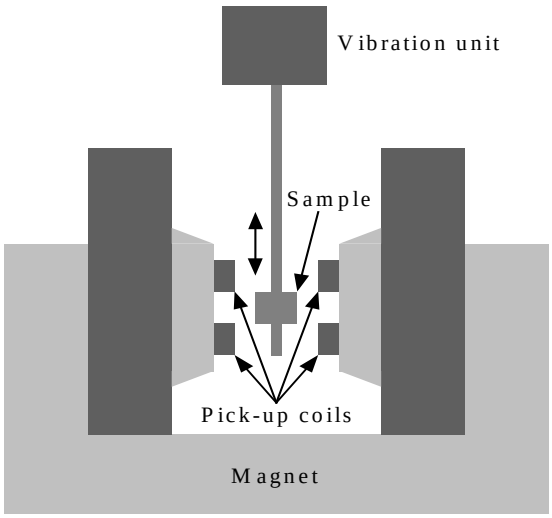

Figure 4.4 Schematic of a VSM.

A VSM operates on Faraday's Law of Induction, which tells us that a changing magnetic field will produce an electric field. This electric field can be measured and can tell us information about the changing magnetic field. A VSM operates by first placing the sample to be studied in an applied magnetic field. If the sample is magnetic, this applied magnetic field will magnetize the sample by aligning the magnetic domains, or the individual magnetic spins, with the field. The stronger the applied field, the larger the magnetic moment until the sample is saturated. The magnetic dipole moment of the sample will create a magnetic field around the sample, sometimes called the magnetic stray field. As the sample is moved up and down, this magnetic stray field position is changing as a function of time and can be sensed by a set of pick-up coils. It works by sensing an induction voltage across the terminals of the pick-up coils, which results from the change of the magnetic flux by the moving magnetic sample.

The induction voltage is proportional to the magnetization of the sample:

$$V(t) = C\, d(fi)/dt \qquad (4.1)$$

where fi(t) represents the (changing) flux in the pick-up coils that results from the moving magnetic sample. From the measured voltage, the system can tell how much the sample is magnetized and how its magnetization depends on the strength of the applied magnetic field.

A typical measurement of a sample is taken in the following manner:

- The strength of the applied magnetic field is set.
- The sample begins to vibrate
- The signal received from the probe is translated into a value for the magnetic moment of the sample

- The strength of the applied magnetic field is changed to a new value. No data is taken during this transition
- The strength of the applied magnetic field reaches its new value
- The signal from the probe again gets translated into a value for the magnetization of the sample
- The applied magnetic field varies over a given range, and a plot of magnetization (M) versus magnetic field strength (H) is generated.

The VSM is extensively used to study the properties of magnetic materials, thin films and multilayer structures. Some VSM measurement results of magnetic thin films and multilayer structures will be given in following chapters.

4.3 The surface measurements: The atomic force microscope

The Atomic Force Microscope (AFM tip/probe)[7] is like a very small phonograph needle. Normally, the AFM tip made of silicon nitride is fabricated by lithographic techniques. As the tip moves across a surface, its position is measured by the deflection of a small laser beam bounced off the reflective back of the tip. Figure 4.5 shows a schematic representation of the AFM instrument. The AFM is based on the detection of small forces (down to 10^{-11} N) acting between a sharp tip and an object. The 'interaction volume' depends on the range of the force, but extends usually a few nm laterally and vertically from the apex of the tip. Accordingly the tip will respond to components of force or force gradients in all three dimensions; the response of the tip is then transferred to the lever stimulating one or more deformation modes. The AFM is therefore in principle capable of quantifiable mapping 3-D contours of strength of interaction.

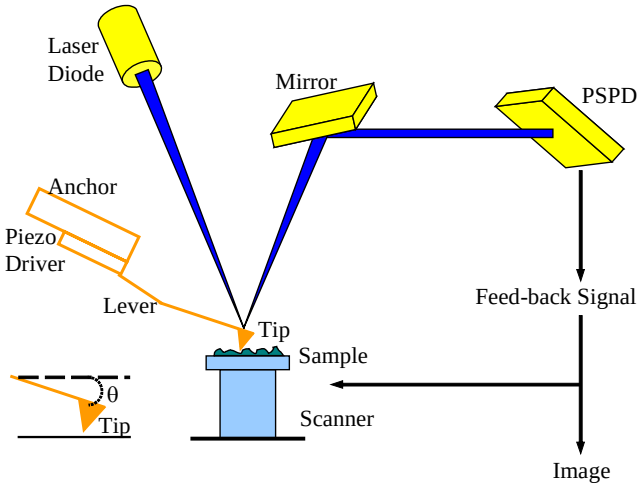

Figure 4.5 Schematic of atomic force microscopy.

The AFM works for most materials. It can image down to atomic dimensions (about 1 Å) but is best for larger features and is usually limited by the tip sharpness. AFM images show critical information about surface features with unprecedented clarity. The AFM can examine any rigid surface, either in air or with the specimen immersed in a liquid. "Minor" (and major) differences between "smooth" surfaces are shown dramatically. On one hand, the AFM can resolve very tiny features, even single atoms, which were previously unseen. On the other hand, the same AFM instrument can examine a field of view larger than 125 microns, so that we can make comparisons with other information, e.g., features seen by the light microscope. The AFM can also examine rough surfaces, since its vertical range can be more than 5 microns. The analytical reports of AFM results include three-dimensional images and quantitative data analysis (such as feature sizes, surface roughness and area, and cross-section plots).

The AFM branch can be sub-divided into its various operational modes. These are commonly referred to as: Contact (when the net force is repulsive); non-contact (when the net interaction is attractive); and tapping (when the tip is in intermittent contact with

the surface being scanned). It should be borne in mind that the reference to 'net' forces implies that effects of adhesive, electrostatic and magnetic interactions can reverse the sign of the force in either contact or non-contact modes. The operating region for different modes is indicated in Fig. 4.6.

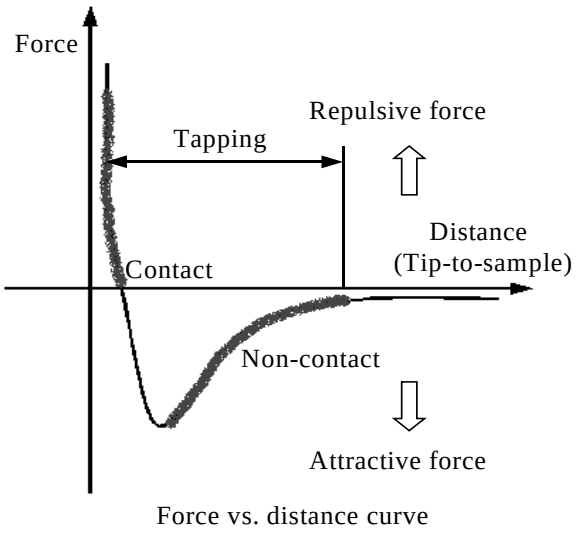

Figure 4.6 The operation region for different modes of AFM.

In contact mode, the tip physically comes in contact with the sample. Atomic resolution can be reached in contact mode; however, there is a risk of damage to soft samples.

During non-contact AFM operation, the cantilever is oscillated at a frequency slightly above the cantilever's resonance frequency. The tip oscillates above the adsorbed fluid layer on the surface. It does not come in contact with the sample surface. The sample is not damaged during non-contact mode; however, the scan speed is much slower, and lower lateral resolution results because of the tip-sample spacing. Non-contact mode is not used very often because of these disadvantages.

During tapping mode, the cantilever is oscillated at or near its resonance frequency. Tapping mode atomic force microscopy is similar to non-contact AFM, except

that for tapping AFM the vibrating cantilever tip is brought closer to the sample so that at the bottom of its travel it just barely hits, or "taps," the sample. For tapping mode AFM operation, the cantilever's oscillation amplitude changes in response to tip-to-sample spacing. An image representing surface topography is obtained by monitoring these changes. Some samples are best handled by tapping mode AFM instead of contact or non-contact mode AFM. Tapping mode AFM is less likely to damage the sample than contact AFM because it eliminates lateral forces (friction or drag) between the tip and the sample. In general, it has been found that tapping mode AFM is more effective than non-contact mode AFM for imaging larger scan sizes, which may include greater variation in sample topography. There is less damage in tapping mode and higher lateral resolution however, there is a slightly slower scan speed than in contact mode. Tapping AFM has become an important AFM technique since it overcomes some of the limitations of both contact and non-contact AFM.

In our studies, we mainly use the tapping mode AFM to get the surface roughness information of magnetic thin films. The AFM tips used in our studies are antimony (n) doped single crystal Si tips with a high resonance frequency of 230~410 kHz.

4.4 Magnetoresistance measurement setup

The magnetoresistance (MR) is the changing in the electrical resistance of MTJs as a function of external applied magnetic field. The MR ration is the ratio of the MR as the magnetization is rotated in direction. The electrical resistance of MTJs can be obtained by sourcing either a constant voltage or a constant current while the magnetic field changes. In our studies, we normally source a constant current from bottom to top electrodes. As

the strength and direction of the magnetic field is changed, the value of the measured voltage between two electrodes will change accordingly. From the measured voltage we can draw the curve of MR ratio vs. magnetic field. Figure 4.7 gives the schematic of MR measurement setup.

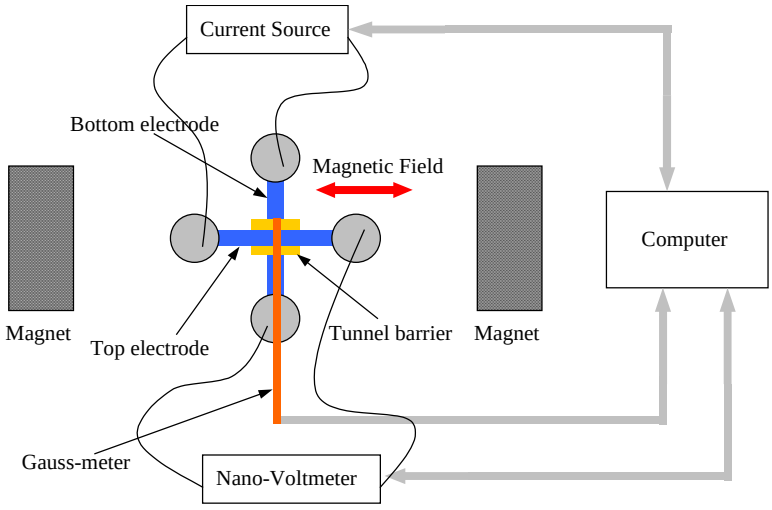

Figure 4.7 Schematics of the 4-probe measurement setup.

It is composed of a computer, a current source (Keithley 236 Source Measure Unit (SMU)), a nano-voltmeter (Keithley 2000), a Lakeshore 450 Gauss-meter and an electromagnet. The computer communicates with these instruments via GPIB cables and collects the measured data during the measurement. The electromagnet was not controlled via GPIB cable. It was controlled by a separated TCR power supply (Electronic Measurement Inc), which does not have a GPIB interface. In order to build a communication between the electromagnet and computer, an Agilent E3631A power supply (with GPIB interface) was used to control the voltage output of the TCR power supply. The Agilent E3631A was also used to control the polarity switching of the electromagnet.

During the measurement process, a constant current is applied to the sample. The sample is placed at the gap of the poles of the electromagnet. The value of the magnetic field is measured by a Guass-meter and transmitted to the computer. As the field changes from positive direction to negative direction, because of the coercivity difference between bottom and top ferromagnetic electrodes, the magnetization directions in two magnetic films starts to switch separately at different value of magnetic field, corresponding to their coercivity. It means that the relative orientation of the magnetization in two FM electrodes will gradually switch from parallel to antiparallel and finally parallel again. The measured resistance as a function of the relative alignment of magnetization directions in two FM electrodes will change accordingly. It is worth noting that choosing the appropriate value of the current is very critical during the measurement. On one hand, the value should not be too small to locate outside the linear region; on the other hand, it should not be too high to introduce the bias voltage effect on TMR ration of MTJs.[8, 9]

4.5 Summary

In this chapter, we gave a brief introduction of the experimental technologies used in our studies. Understanding of the working principles of these techniques is helpful in understanding the experimental results in depth. The AFM (DI 3000 from Digital Instruments) was used to measure the surface roughness of $Ni_{80}Fe_{20}$ thin films. Magnetic properties of thin films and the magnetic response of multiplayer structures were measured by VSM (Digital measurement system (DMS) 1660). Magnetic tunnel junction was measured by using the homemade magnetoresistance measurement setup. The experimental results are presented in following chapters.

[1] D. M. Mattox, *"Handbook of physical vapor deposition processes"*, Lattice press (1998).

[2] R. F. Bunshah, *"Handbook of Deposition Technologies for Films and Coatings"*, Noyes publications (1994).

[3] K. L. Chopra, "*Thin Film Phenomena*", Robert G. Krieger publishing company, Huntington, New York (1979).

[4] K. Wasa and S. Hayakawa, "*Handbook of Sputter Deposition Technology*", Noyes Publications, Park Ridge, New Jersey, (1991).

[5] K. L. Chopra, and I. Kaur, "*Thin Film Device Applications*", New York, Plenum Press (1983).

[6] D. Speliotis, "Getting the most from your vibrating sample magnetometer", *ADE Technologies, Inc., USA*

[7] S. H. Cohen and M. L. Lightbody "*Atomic Force Microscopy/Scanning Tunneling Microscopy*", New York, Plenum Publishers (1998).

[8] J. Zhang, R. M. White, *J. Appl. Phys.* **83**, 6512 (1998).

[9] Y. Lu, X. W. Li, G. Xiao, R. A. Altman, W. J. Gallagher, A. Marley, K. Roche, and S. Parkin, *J. Appl. Phys.* **83**, 6515 (1998).

Chapter 5

Surface Roughness Control and its Effect on MTJs

On the basis of the simulation results obtained in Chapter 3, we conclude that the interfacial roughness in magnetic tunnel junctions could have a great influence on the TMR and IEC in multilayer structures. A smooth surface is very important to achieve MTJs with high TMR ratio and independent switching of two FM layers. In this chapter, the surface roughness of the bottom ferromagnetic layer will be investigated experimentally. The surface roughness of $Ni_{80}Fe_{20}$ thin films as a function of the deposition conditions is investigated. Co thin films and the magnetic multilayer structures were deposited on top of the $Ni_{80}Fe_{20}$ thin films with different surface roughness. The effect of the buffer layer surface roughness on the magnetic properties of the Co thin films and the switching properties of the magnetic multilayer structures have been investigated.

5.1 Surface roughness control and effect on magnetic properties of $Ni_{80}Fe_{20}$ thin films

It is well known that the surface roughness of the thin film depends greatly on experimental parameters used during the deposition. In previous studies, surface roughness of $Ni_{80}Fe_{20}$ thin films was changed by depositing onto the ion milling etched Si substrates and the effect of surface roughness on magnetic properties of $Ni_{80}Fe_{20}$ thin films have been studied. In our study, we propose to improve the surface roughness by

varying different experimental parameters: (1) film thickness; (2) dc sputter power; and (3) rf substrate bias, during the magnetron sputtering process. The effects of experimental parameters on the surface roughness and the coercivity of the $Ni_{80}Fe_{20}$ thin films were investigated.

5.1.1 Experimental procedure

$Ni_{80}Fe_{20}$ thin films were prepared by using dc magnetron sputtering in a high-vacuum deposition chamber. The distance from the target to substrate in the sputtering chamber is about 15 cm. A base pressure of 4×10^{-7} Torr was used. The $Ni_{80}Fe_{20}$ thin films were deposited at 10 mTorr Ar gas pressure onto Si (100) substrates and the film deposition rate calibration was performed for different deposition conditions. The thickness of the films was characterized by α-step profilometer, and the deposition rate was calculated accordingly. The magnetic properties of the $Ni_{80}Fe_{20}$ thin films were measured by VSM. The topography of samples was investigated using a Digital Instruments 3100 AFM in tapping mode. The full average deviation of surface roughness (R_a) of the mean height was measured by scanning a 1μm x 1 μm area. For every sample, the AFM measurement was performed at two different areas. The error bar shown in the figures was based on the AFM measurement throughout the studies.

5.1.2 Results and discussion

The film thickness dependency of the surface roughness was carried out by depositing $Ni_{80}Fe_{20}$ thin films with different thickness under 200 W dc sputter power with 20 W rf bias applied to the substrate. The surface roughness of $Ni_{80}Fe_{20}$ thin films also changes in

a narrow range from 0.164 to 0.220 nm as the thickness of thin films was changed from 3 nm to 10 nm. A minimum value was achieved at film thickness of 8 nm. As to the magnetic properties, the coercivity of the film with the thickness of 3 nm cannot be measured by VSM. This is due to the sensitivity limitation of the VSM in the case of measuring ultra thin magnetic films. There are no significant variations of coercivity for the rest of the samples.

The $Ni_{80}Fe_{20}$ thin films were deposited by using different dc power levels (50~250 W) to the target while the rf substrate bias was kept constant (20 W). For the purpose of comparison, the same film thickness of 8 nm was used. According to the data obtained from AFM images, the surface roughness of $Ni_{80}Fe_{20}$ thin films changes in a narrow range (from 0.197 to 0.376 nm) as the dc sputter power was varied from 50-250 W. The minimum value of surface roughness was obtained with 200 W dc sputter power. The coercivity of $Ni_{80}Fe_{20}$ thin films as a function of dc sputter power shows a small variation from 1.984 to 2.314 Oe.

From the results obtained above, we found that the surface roughness dependence on dc power and the film thickness is very small. However, in general the $Ni_{80}Fe_{20}$ thin films show a smooth film surface. We suspect that the smooth film surface is due to the rf bias applied to the substrate during the sputtering process. In order to reinforce this, six sets of samples were prepared, corresponding to the different rf powers (0, 3, 5, 10, 15, and 20 W) applied to the substrate. $Ni_{80}Fe_{20}$ thin films were deposited by using 200 W dc sputter power and the different rf powers were applied to the substrate during the film deposition. The thickness of the films was kept constant as 8 nm via adjusting the

deposition time for different conditions according to the deposition rate obtained from the thickness calibration results.

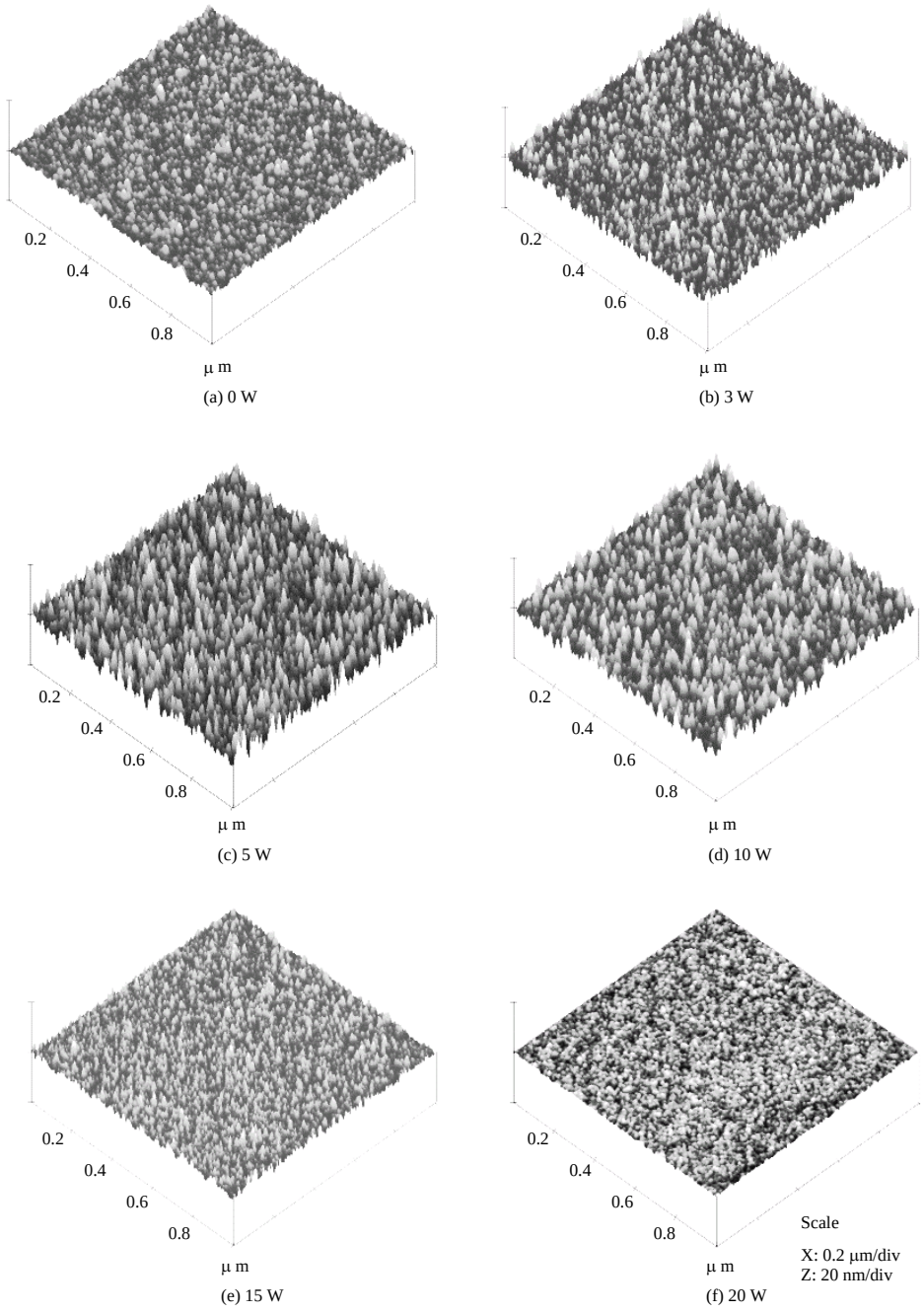

Figure 5.1 AFM images for $Ni_{80}Fe_{20}$ thin films deposited with different rf substrate bias.

The AFM images (a)~(f) in Fig. 5.1 show different surface roughness of $Ni_{80}Fe_{20}$ thin films on Si substrate induced by different strength of rf biases applied to the substrate.

We observed the changes in the surface roughness of the $Ni_{80}Fe_{20}$ thin films as the rf bias was increased from 0~20 W. The surface morphologies show island-like grain features with different heights in the vertical direction corresponding to the changes of the applied rf substrate bias. The average roughness R_a and the coercivity of $Ni_{80}Fe_{20}$ thin films as a function of rf bias were plotted in Fig. 5.2. The surface roughness of $Ni_{80}Fe_{20}$ increased from 0.984 nm to a maximum value of 1.697 nm as the rf bias was increased from 0 to 5 W, then decreased to 0.197 nm as the rf bias was further increased to 20 W.

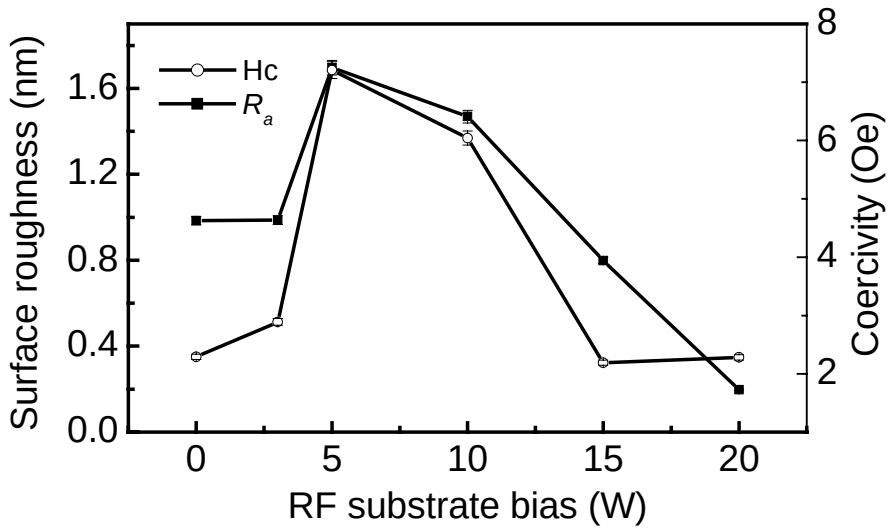

Figure 5.2 The surface roughness and the coercivity of $Ni_{80}Fe_{20}$ thin films as a function of the rf substrate bias.

As shown in Fig. 5.2, the coercivity variation of the $Ni_{80}Fe_{20}$ thin films as a function of rf bias showed a similar trend to that of the surface roughness when the $Ni_{80}Fe_{20}$ thin films have a relatively rough surface of over 1 nm in our studies. When the roughness of the film surface is below 1 nm, the coercivities of the thin films are about 2 Oe. A maximum value in coercivity with 5 W rf bias was achieved. The increase of the coercivity of $Ni_{80}Fe_{20}$ films is attributed to the rough surface for 5 and 10 W rf bias samples. Once the surface becomes rough, the in-plane “magnetic poles” induced by local surface roughness

will result in a demagnetizing field. This surface anisotropy will change the domain wall thickness and domain size of $Ni_{80}Fe_{20}$ films, thereby inducing the domain wall pinning. Such pinning will make the domain wall motion more difficult, thus resulting in the enhancement of the coercivity. Intuitively, the domain wall energy per unit volume is proportional to the roughness-to-thickness ratio. In our case, the average deviation of surface roughness (Ra) of the mean height is 1.6 nm for the sample deposited with 15W rf bias applied to the substrate during the sputtering process, which gives a roughness-to-thickness ratio of 0.2. This value is quite substantial. Therefore, the magnetization reversal is dominated by the domain wall pinning for NiFe thin films with such a high value of Ra.

5.2 Surface roughness effect on properties of magnetic thin films and switching properties of magnetic multilayer structures

On the basis of the results obtained in the previous section, we found that the rf substrate bias is the key factor in determining the surface roughness states of the thin film and the surface roughness of thin films can be modified by the strength of rf bias applied to the substrate. It has been shown that the magnetic properties of thin films depend on the surface roughness of the thin films. If magnetic thin films or magnetic multilayer structures were deposited on top of these $Ni_{80}Fe_{20}$ thin films with different values of surface roughness, the properties of magnetic thin films and the switching properties of the multilayer structures will be significantly influenced.

In this part of the work, samples with the multilayer structures of $Si/Ni_{80}Fe_{20}/Al/Co/Al$ and $Si/Ni_{80}Fe_{20}/Al/Co/Al_2O_3/Ni_{80}Fe_{20}/Al$ (as shown in Fig. 5.3 (a)

and Fig. 5.3 (b)) were deposited with $Ni_{80}Fe_{20}$ underlayer prepared with different rf biases. As the deposition rate of the $Ni_{80}Fe_{20}$ thin films varied when the different rf biases were applied to the substrate, the deposition time for different conditions was adjusted to achieve the same $Ni_{80}Fe_{20}$ film thickness of 8 nm in this part of the work. The Al and Co thin films in the multilayer structures were deposited at 10 mTorr Ar gas pressure with 50 W and 100 W dc sputter power, respectively. There was no substrate heating and magnetic field application during the deposition processes. The tunnel barrier in the multilayer structure was formed by plasma oxidizing a 20Å Al thin film. The plasma oxidation was performed by applying a substrate rf bias at the atmosphere of Ar and oxygen (20% volume fraction) mixture. Although the oxidation conditions for barrier formation may not be the optimal as either over-oxidation or under-oxidation could occur, the oxidation condition was the same for the whole set of samples.

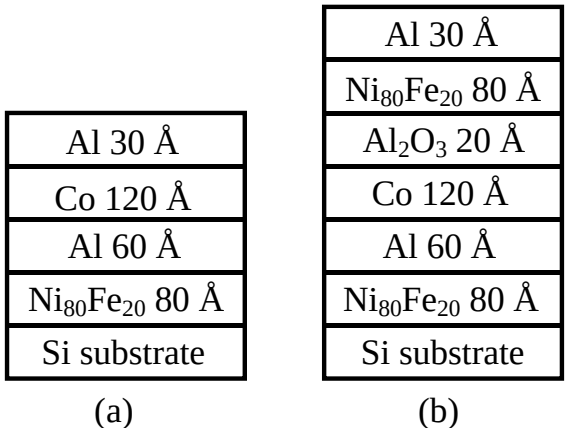

Figure 5.3 Schematic of multilayer structures, (a) $Si/Ni_{80}Fe_{20}/Al/Co/Al$; and (b) $Si/Ni_{80}Fe_{20}/Al/Co/Al_2O_3/Ni_{80}Fe_{20}/Al$.

The rf bias induced surface roughness dependence of the magnetic properties of the Co films and the switching properties of $Co/Al_2O_3/ Ni_{80}Fe_{20}$ multilayer were studied. The Al layer was used to decouple the $Ni_{80}Fe_{20}$ underlayer and the Co layer in both cases. The top Al layer was used to prevent the oxidation of the magnetic thin films. For the purpose

of comparison, the reference samples without $Ni_{80}Fe_{20}$ underlayer for these two structures were deposited as well.

5.2.1 Surface roughness effect on magnetic properties of Co thin films

A set of samples with basic structure of Al/Co/Al on top of Si substrates with and without the $Ni_{80}Fe_{20}$ underlayer was prepared. The $Ni_{80}Fe_{20}$ underlayer was deposited with different values of applied rf substrate bias ranging from 0~20 W. Figure 5.4 shows the hysteresis loops of Al/Co/Al films on top of Si substrates with and without the $Ni_{80}Fe_{20}$ underlayer. Figure 5.4 (a) represents the reference Si substrate without $Ni_{80}Fe_{20}$ whereas Fig. 5.4 (b) and Fig. 5.4 (c) refer to samples with $Ni_{80}Fe_{20}$ underlayer, deposited with 5 W and 20 W rf substrate bias, respectively.

The coercivity of Co thin film without NiFe underlayer is 20 Oe. As the NiFe underlayer is introduced, the coercivity of the stacks varies in the range of 20~24 Oe as the values of the rf substrate bias change from 0~15 W and finally deceases to 15 Oe for the sample with 20 W rf substrate bias. Besides the difference in the coercivity values, the general features of the hysteresis loops also have some differences. Compared to the sample without $Ni_{80}Fe_{20}$ underlayer, the hysteresis loops corresponding to the samples with $Ni_{80}Fe_{20}$ underlayer (deposited without and with 3~10 W bias), demonstrated different features. One of the hysteresis loops (shown in Fig. 5.4 (b)) was selected to make a more detailed description. As the magnetic field changes from the negative direction to positive direction, due to the relative smaller coercivity, the magnetic reversal occurred first in $Ni_{80}Fe_{20}$ thin films. Co film has a higher magnetic anisotropy, only some of the domains in Co film would relax from its saturation state by rotating the

magnetization directions. The magnetic responses in region 1 were mainly due to the domain wall motion of the $Ni_{80}Fe_{20}$ thin films, responding to the combined applied field and the demagnetization field from the Co film.

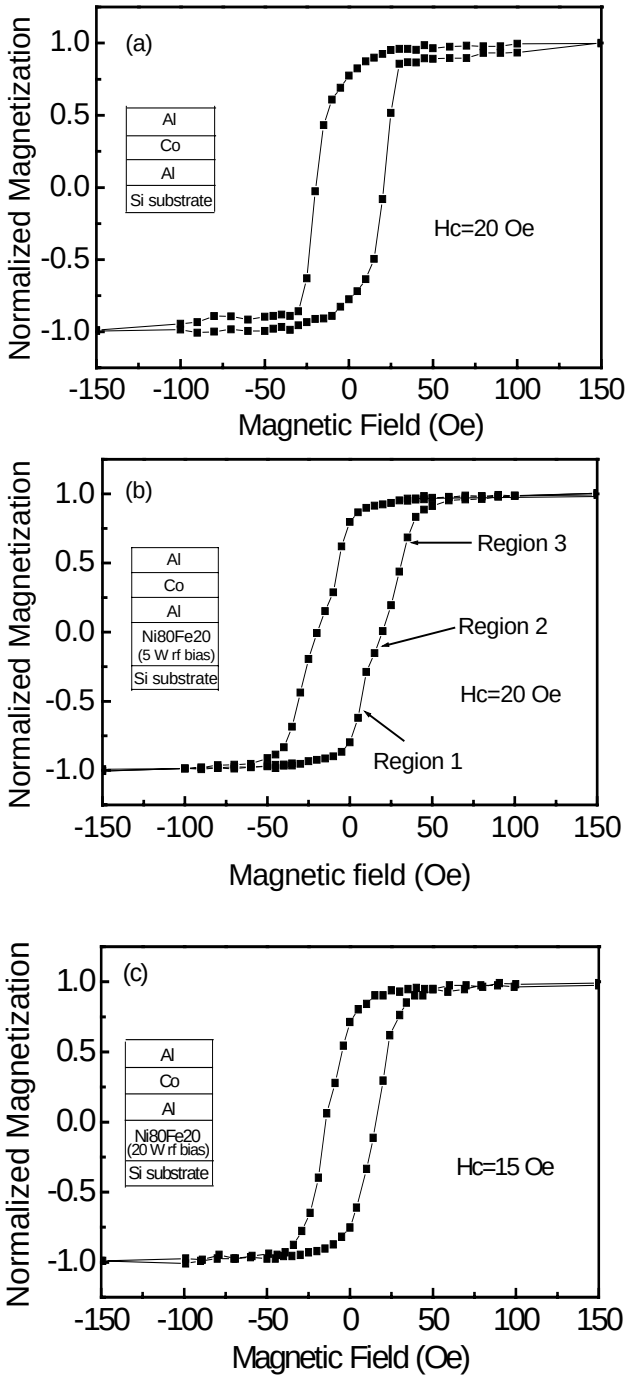

Figure 5.4 The hysteresis loops of Al/Co/Al on top of Si substrate without (a) and with $Ni_{80}Fe_{20}$ underlayers deposited with (b) 5 W rf bias and (c) 20 W rf bias.

The region 2 represents a transition area; a small kink can be seen from the loops. At this point, the $Ni_{80}Fe_{20}$ domain wall motion has completed and most of the domains in the Co still have not started to reverse due to its higher magnetic anisotropy. Over this point, the magnetic reversal in region 3 is dominated by the domain wall motion of the Co thin film. As the further increase of the external field, the magnetization directions in both $Ni_{80}Fe_{20}$ and Co thin films rotate to the external field direction and are eventually saturated. It can be seen from Fig. 5.4 (c) that the kink almost disappears for the sample with 20 W rf substrate bias. We attribute this to the decrease of the coercivity of the Co film due to the smooth surface of the $Ni_{80}Fe_{20}$ underlayer. The thickness of Co thin films in our studies is 12 nm. Domain walls in these thin films usually interact with the top and bottom surfaces of the film,[14] thus the surface roughness has a great influence on the coercivity. Choe *et al.* showed experimentally that the coercivity of films decreased as the surface roughness became smoother.[11] For sample with $Ni_{80}Fe_{20}$ underlayer deposited with 5 W rf substrate bias, the local surface roughness will induce in-plane "magnetic poles", which may result in an in-plane demagnetizing field. Surface roughness-induced magnetic anisotropy will change the domain wall thickness and domain size of Co films, thereby inducing the domain wall pinning. A decrease in freedom in domain wall motion thus leads to the enhancement of coercivity.

5.2.2 Surface roughness effect on switching properties of multilayer structure

In this part of work, we will compare the switching properties of the multilayer structure with $Ni_{80}Fe_{20}$ underlayer (without and with 20 W bias) to the reference sample without $Ni_{80}Fe_{20}$ underlayer.

Figure 5.5 (a) and 5.5 (b) show the hysteresis loops of the multilayer structure Si/Al/Co/Al_2O_3/$Ni_{80}Fe_{20}$/Al and Si/$Ni_{80}Fe_{20}$/Al/Co/Al_2O_3/$Ni_{80}Fe_{20}$/Al on top of Si substrate. The bottom $Ni_{80}Fe_{20}$ thin film in the latter structure acts as an underlayer and the Co/Al_2O_3/$Ni_{80}Fe_{20}$ constitutes a standard magnetic tunnel junction structure. 20 W rf bias was applied to the substrate during the deposition of the $Ni_{80}Fe_{20}$ underlayer.

Five states (1) to (5) are indicated on the hysteresis loop to illustrate the relative magnetic switching of Co and $Ni_{80}Fe_{20}$ films when the field changes from one direction to another. In state (1), the applied magnetic field is strong enough to saturate both $Ni_{80}Fe_{20}$ and Co thin films. As the magnetic field decreases and changes direction from positive to negative, the $Ni_{80}Fe_{20}$ thin film starts to reverse and domain wall motion dominates the reversal features. The domain wall motion of the $Ni_{80}Fe_{20}$ thin films is completed at state (2). The region between state (2) and state (3) illustrates that there are some domains in Co thin film that start to reverse its magnetization direction along to the direction of the external field while the majority domains still remain unchanged because the strength of the external field is not enough to overcome the magnetic anisotropy field in Co thin film. The reversal features between state (3) and state (4) are attributed to the domain wall motion of the Co thin film. Comparison of the reversal features in Fig. 5.5 (a) and Fig. 5.5 (b) demonstrates that the domain wall motion of the Co layer shown in Fig. 5.5 (a) is not as smooth as that shown in Fig. 5.5 (b). The magnetic switching of the multilayer structure with a $Ni_{80}Fe_{20}$ underlayer shows a relatively narrow switching range and a steep slope.

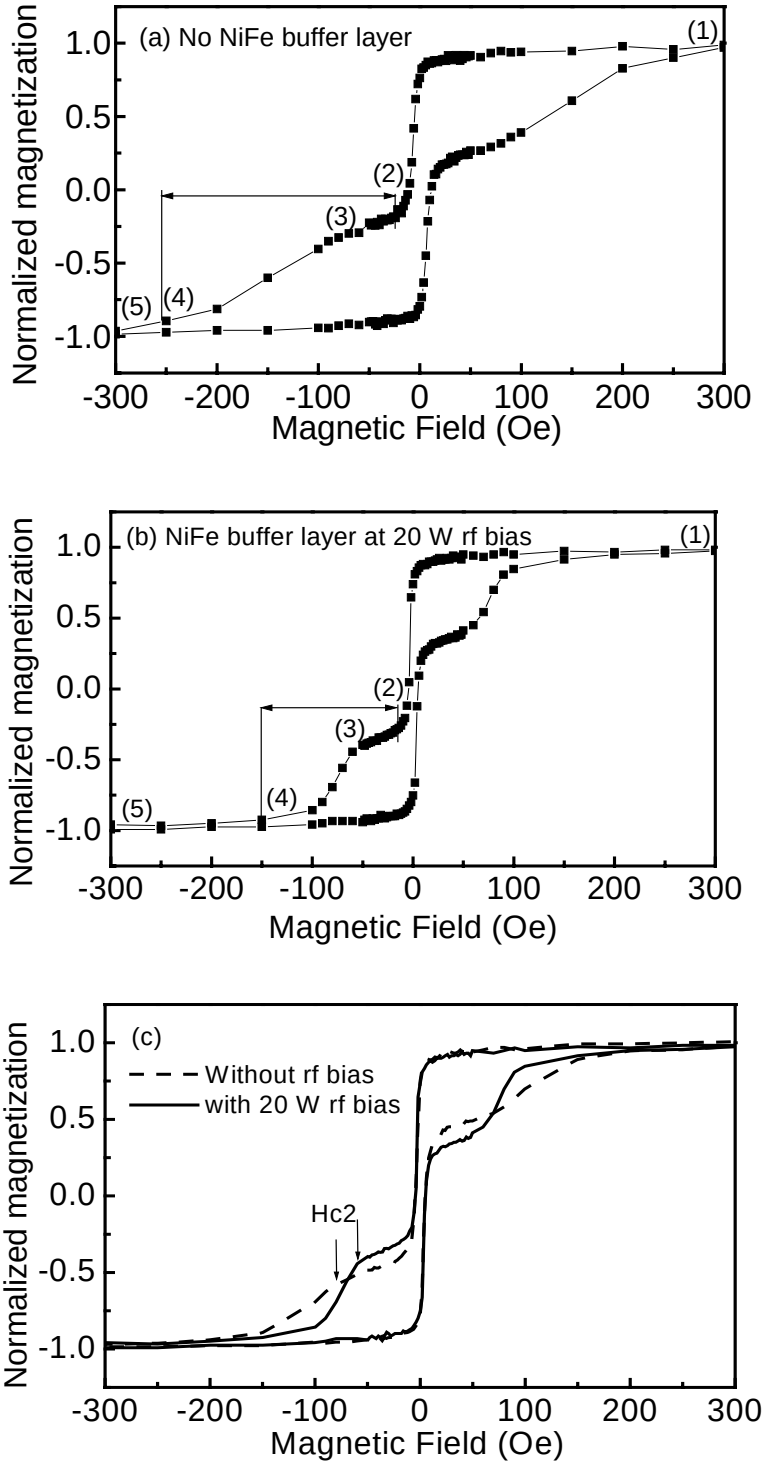

Figure 5.5 Hysteresis loops for multilayer structure without and with $Ni_{80}Fe_{20}$ buffer layer; (a) $Si/Al/Co/Al_2O_3/Ni_{80}Fe_{20}/Al$; (b) $Si/Ni_{80}Fe_{20}/Al/Co/Al_2O_3/Ni_{80}Fe_{20}/Al$; and (c) comparison of multilayer structures with $Ni_{80}Fe_{20}$ underlayer deposited without and with 20 W rf bias.

Furthermore, a comparison of the results between the two samples with different rf substrate bias applied to the $Ni_{80}Fe_{20}$ underlayer shows the similar results, as illustrated by the samples with 0 and 20 W rf substrate bias in Fig. 5.5 (c). The switching process occurs in a narrower range for the sample with a smoother surface (20 W rf substrate bias). The starting points of switching for Co thin films (marked Hc2 in the figure) show that the coercivity of Co is smaller for the case with 20 W rf substrate bias. The result is consistent with the results obtained in the section 5.2.1. However, the values of the coercivity of Co thin films in the section 5.2.1 are different from the switching field of Co thin films in Fig. 5.5. This could be due to the exchange coupling between the Co thin film and the top $Ni_{80}Fe_{20}$ thin film through the Al_2O_3 tunnel barrier. One must also note that in the fig.5.5, the Al_2O_3 is contact with the Co whereas in Fig.5.4, the Al is contact with the Co layer as a cover layer.

The difference in the switching properties of the multilayer structures is attributed to the change of the domain wall structure of the Co thin films, induced by $Ni_{80}Fe_{20}$ underlayers with different surface roughness. In the case of rough surfaces, roughness induced pinning sites for the Co films result in a blockade in domain wall motion. The reversal process is thus dominated by domain wall pinning, causing the magnetization change to be more difficult. As the surface becomes smoother, less pinning occurs in Co film, thus the reversal process occurs in a relatively narrow region. In our studies, we focus on the comparison of the switching behaviors among samples deposited under different conditions. Our descriptions about the switching properties are based on the comparison of the hysteresis loops. To verify the exact reversal process, other measurements such as virgin curve and angular dependence are required.

5.3 Summary

We have studied the effect of dc sputter power, thickness and rf substrate bias on surface roughness and magnetic reversal properties of Co and $Ni_{80}Fe_{20}$ thin films. We conclude that the surface roughness of the thin films depend weakly on dc sputter power and film thickness; however, the surface roughness of the thin films can be well controlled by applying an rf substrate bias during the deposition. The surface roughness and magnetic properties of $Ni_{80}Fe_{20}$ thin films have been greatly modified by the rf bias applied to the substrate. The coercivity change of the $Ni_{80}Fe_{20}$ thin films was attributed to the change of the surface roughness. The rf bias induced surface roughness also has great influence on magnetic properties of Co films on top of the $Ni_{80}Fe_{20}$, with controlled surface roughness, and the switching properties of MTJs stacks. We observed marked changes in the magnetic properties of Co films and switching properties of multilayer structures due to a reduction of the surface roughness by the rf bias applied to the substrate.

The achieved smooth surface of the bottom $Ni_{80}Fe_{20}$ layer makes it possible for us to fabricate the MTJ devices. In the next chapter, MTJ devices will be fabricated by using the experimental conditions for MTJ stacks deposited in this chapter.

Chapter 6

Shadow Mask Fabrication of MTJs

6.1 Introduction

So far, the effects of barrier properties and the interface roughness on TMR ratio of MTJs have been simulated in Chapter 3. Results show that MTJs with a higher barrier height and smoother interface will give higher TMR ratio. In Chapter 5, the control of the surface roughness and the effects of the surface roughness of the buffer layer on the properties of the magnetic thin films and the switching properties of magnetic multilayer structures have been studied based on multilayer thin film structures. The surface roughness of the bottom FM layer was well controlled by applying an rf substrate bias during the deposition. $Ni_{80}Fe_{20}$ bottom electrode with a smooth surface (R_a = 1.97Å) was achieved.

In this part of the work, MTJs were fabricated and the effects of some experimental parameters on the properties and the performance of MTJs were evaluated. It has been mentioned before that one of the most important aspects for MTJs fabrication is the method used to form the tunnel barrier, and its impact on the properties of MTJs such as *RA*, TMR ratio, and *RA* uniformity across a large area. Various oxidation methods have been studied recently, which include natural oxidation,[1-3] glow discharge oxidation, plasma oxidation,[4] UV light assisted oxidation,[5,6] in-situ natural oxidation[7,8] and reactive sputtering oxidation. Comparison of different oxidation methods for barrier formation in MTJs have been studied by Chen *et al.*.[9] They have explored forming the

aluminum oxide tunnel barrier with air; reactive sputtering; plasma oxidation with plasma source; plasma oxidation with power introduced from the target side; and plasma oxidation with power introduced from the substrate side. Results show that all techniques can work. Plasma oxidation is favored due to its simplicity and manufacturing compatibility. Several factors will determine the efficiency of the plasma oxidation, such as the way to generate the plasma, the strength of plasma, the geometric design of the chamber, gas pressure and oxidation time.

As we mentioned in the section 2.4.1.4, the tunnel barrier formed in the Kr and O_2 mixture shows a faster oxidation rate, thus it can efficiently prevent the over-oxidation of the bottom electrode. That is because of the different oxidation rates at the grain boundaries versus the interior of the grains. Their results imply that the quality of the tunnel barrier depends on the microstructure of as-deposited Al thin film for barrier formation.

In our studies, the tunnel barrier was formed by plasma oxidation of Al thin films with rf bias introduced to the substrate. The objectives of this part of our work include: investigating the effects of the oxidation time on barrier properties and the performance of MTJs; studying the effects of the microstructure of as-deposited Al thin film for barrier formation on barrier properties, junction resistance and performance of MTJs; evaluating the effects of the oxidation time and the microstructure of as-deposited Al thin films used for barrier formation on the magnetic properties of the Co top layer and the switching properties of the MTJ stacks. The contribution of these factors to device characteristics will be evaluated in conjunction with rf substrate bias application.

6.2 Fabrication of MTJs

The MTJs were fabricated by using a shadow mask technique. The schematic of the shadow mask design for every single layer and the integrated junction structure are given in Fig. 6.1. It can be seen that the effective size of the bottom electrode is 400 μm and the effective sizes of the top electrode are 100, 200, 300 and 400 μm, respectively. Four cross-geometry MTJs structures with sizes ranging from 400 x 100 to 400 x 400 μm^2 can be fabricated by using shadow masks.

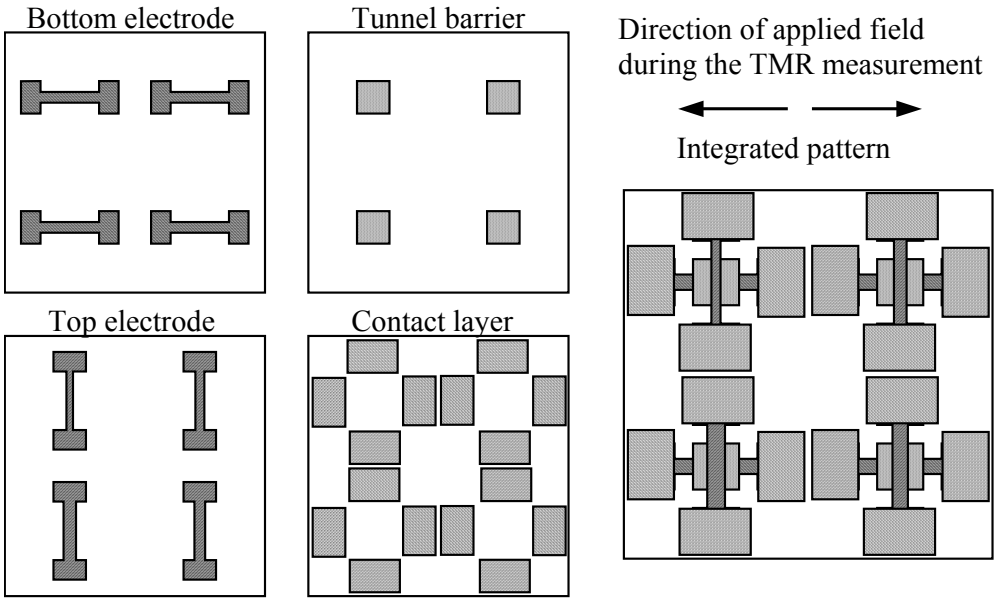

Figure 6.1 Shadow mask pattern for each layer and the integrated pattern.

6.2.1 Experimental procedure

Films were deposited onto a 10 x 10 mm Si or glass substrate in the dc magnetron sputter system. MTJs with basic structure of substrate/ $Ni_{80}Fe_{20}$ 25 nm/AlO_x/Co 30 nm was fabricated by using shadow masks. The tunnel barriers were formed by oxidizing 1.5 nm Al thin films. The deposition was done with a base pressure of 4 x 10^{-7} Torr. The $Ni_{80}Fe_{20}$

bottom electrode was first deposited on top of the Si substrate by dc sputtering through the metal mask to form a narrow stripe onto the substrate with a 20 W rf bias applied to the substrate. Next, the Al thin film was deposited through another mask and then the tunnel barrier was formed by a two-step plasma oxidation method. The first step was to deposit 0.9 nm Al layer and then to oxidize by applying a 6 W rf bias from the substrate side in a 15 mTorr with a mixed gas of argon and oxygen (20% volume fraction). After that, 0.6 nm Al layer was deposited again and oxidized. In this two-step oxidation process, the first oxidation is more critical than the second step. When we carried out the second step oxidation, we need not be so concerned about the oxidation of the bottom ferromagnetic layer, since the previously formed first AlO_x layer will act as a barrier layer. After the formation of the tunnel barrier, the Co top electrode was deposited by dc sputtering through the top electrode mask. Finally, the Al contact pad was deposited for the purpose of the TMR measurement. Two sets of MTJs were fabricated by shadow mask technique to investigate the effects of the oxidation time and the microstructure of the Al thin film for barrier formation on properties of tunnel barrier and the characteristics of MTJs, respectively.

Conditions associated with MTJs for the investigation of oxidation time effect are summarized in Table 6.1 and Table 6.2.

Table 6.1 Deposition conditions for thin films in oxidation time effect investigation.

Material	Deposition power (W)	rf substrate bias (W)	Working gas pressure (mTorr)
$Ni_{80}Fe_{20}$ bottom electrode	200	20	10
Al for barrier formation	30	-	3
Co top electrode	100	-	10
Al for contact pad	200	-	10

Table 6.2 Oxidation conditions for barrier formation.

Sample Name	Thickness of Al thin film (1st step)	Oxidation time (1st step) (Sec)	Thickness of Al thin film (2nd step)	Oxidation time (2nd step) (Sec)
50 s	9 Å	20	6 Å	30
60 s		30		
70 s		40		
80 s		50		
90 s		60		

Al thin films were deposited under different working gas pressures (1, 3, 5 and 8 mTorr) to investigate the effect of the Al thin film microstructure on the characteristics of MTJs. The detailed deposition conditions for every single layer and the plasma oxidation procedures are listed in Table 6.3.

Table 6.3 Deposition conditions for thin films in Ar gas pressure investigation.

Material	Deposition power (W)	Oxidation time (s)	rf substrate bias (W)	Working gas pressure (mTorr)
$Ni_{80}Fe_{20}$ bottom electrode	200	1st 9 Å Al	20	10
Al for barrier formation	30	for 40 s and	-	1, 3, 5, 8
Co top electrode	100	2nd 6 Å Al	-	10
Al for contact pad	200	for 30 s	-	10

After the fabrication of MTJs, 4-probe measurements were performed for every set of sample to obtain the TMR ratio and the I-V characteristics of the MTJs. The direction of applied magnetic field during the measurements was along the length of the $Ni_{80}Fe_{20}$ bottom electrode (as shown in Fig. 6.1). The magnetic switching properties of the MTJ stacks were investigated by performing the VSM measurements on control samples (10 x 10 mm) for each set of MTJs.

6.3 Results and discussion

6.3.1 Effect of oxidation time

One of the critical parameters in the plasma oxidation process is the oxidation time, which has a great influence on barrier properties, thus the characteristics of MTJs. Therefore, it is worthwhile to investigate the effects of the oxidation time on the properties of the tunnel barrier and the performance of MTJs.

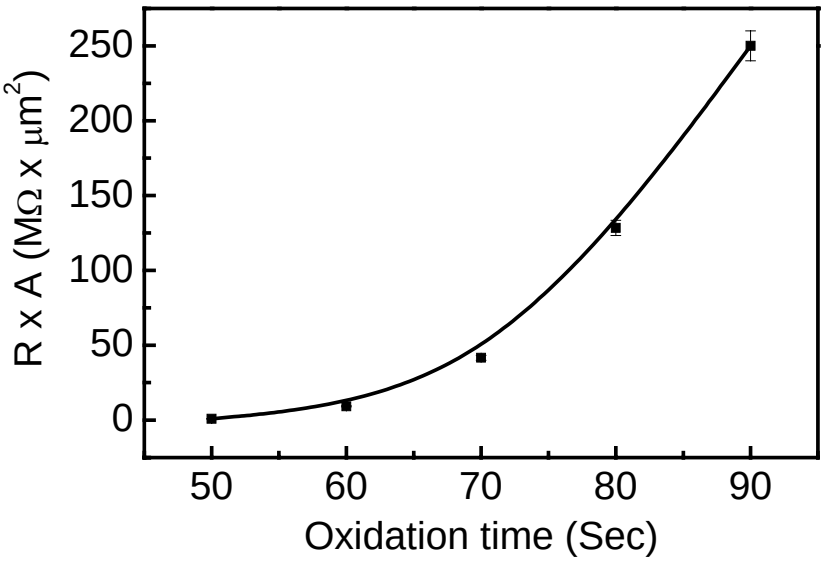

Figure 6.2 Junction resistances as a function of plasma oxidation time (The error bars of lowest three points are too small to be seen due to the large y axis scale).

Figure 6.2 presents the variations of the junction *RA* as a function of oxidation time, for five junctions with total oxidation time of 90, 80, 70, 60 and 50 s respectively. The junction *RA* is based on MTJs with size of 100 x 400 μm^2. For all these samples, the resistances of the bottom and top electrodes are much smaller than the junction resistance. No geometry enhancement of TMR is found. From the curve we can see that the *RA* is 250 $M\Omega \cdot \mu m^2$ for MTJs with barrier formed by oxidizing the Al thin film for 90 s. The

value of the *RA* decreases as the oxidation time decreases. The *RA* further decreases to 0.84 MΩ·μm^2 for short oxidation time (50 s).

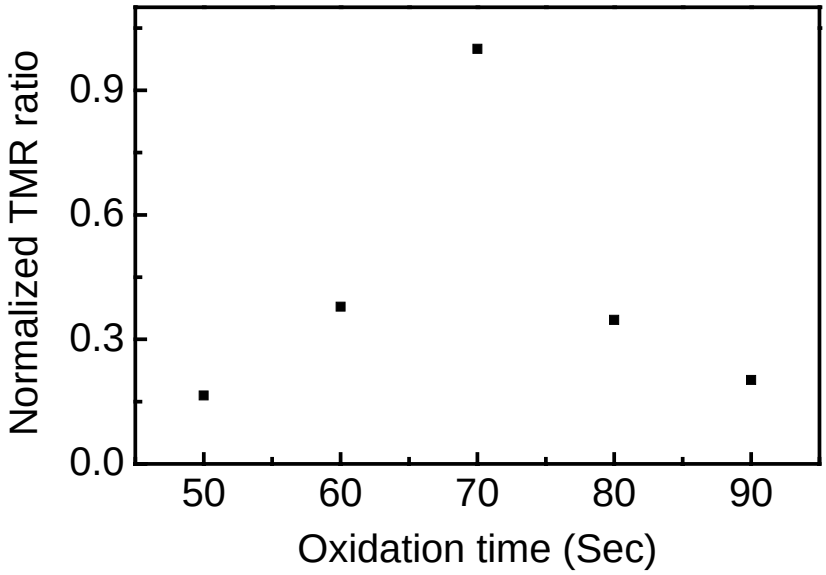

Figure 6.3 Normalized TMR ratios as a function of plasma oxidation time.

The dependence of the normalized TMR on oxidation time is shown in Fig. 6.3. The normalization of the TMR was based on the maximal TMR ratio achieved in MTJs with tunnel barrier formed with 70 s oxidation time. For longer oxidation times, the TMR ratio decreases gradually and the junction resistance increases. This may be attributed to the partial oxidation of the bottom electrode, which results in the reduction of the spin polarization near the interface. For shorter oxidation times, the non-oxidized Al films on top of the bottom electrode will introduce un-polarized electrons or spin scattering at the interface, thus resulting in the decrease of the TMR.[10]

I-V curves of these junctions were fitted using Simmons' tunneling theory[11] to obtain the effective barrier thickness and the effective barrier height. Figure 6.4 shows both the positive and negative bias voltage of the I-V curve of a representative junction

with Al film oxidized for 70 s with size of 400 x 100μm^2. The scatter points represent the measured I-V curve and the solid lines are fitted I-V curves. It can be seen that the measured data and the fitted curve matched very well.

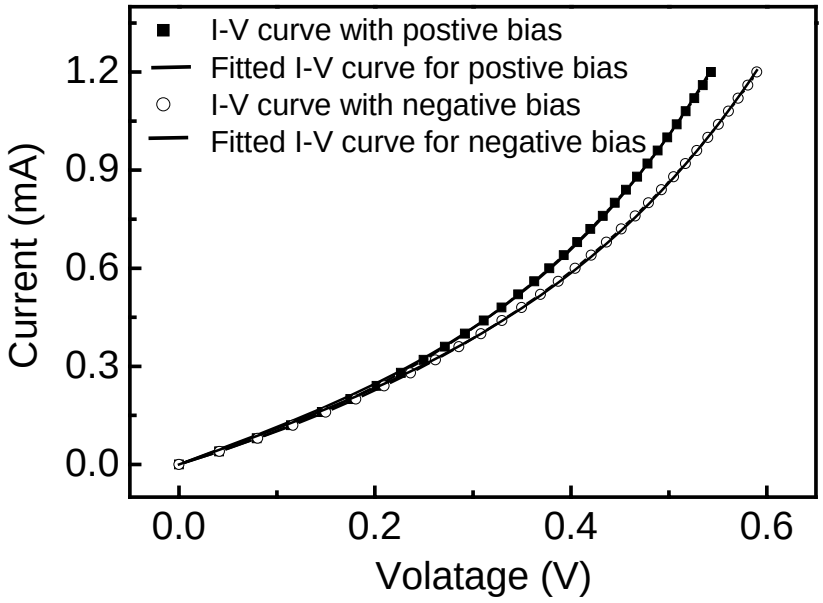

Figure 6.4 Measured and fitted I-V curves for junctions with barrier formed by 70 s oxidation.

A positive bias is defined as the current flowing from the bottom to the top electrode. If we look at the positive and the negative I-V curves for the junction, we find that there is an asymmetry. The observed asymmetry in the I-V curves may result from the barrier height difference on both sides of the junction, which arises from the different FM layer in contact with the tunnel barrier or partial oxidation of the bottom electrode.

The mean effective barrier thickness (t_{eff}) and the mean effective barrier height (ϕ_{eff}) as a function of the oxidation time for MTJs with barrier formed with different oxidation time were investigated based on Simmons' model. The thickness (t) and the barrier height (ϕ) of the tunnel barrier were variables. The tunneling current was calculated by substituting the measured voltage data, values of t and ϕ into Simmons'

model. The calculated current was compared to the measured current data. The t_{eff} and ϕ_{eff} of MTJs were obtained when the minimal misfit between the measured and the calculated current was achieved. The Simmons' model and the program for I-V curve fitting are given in the appendix.

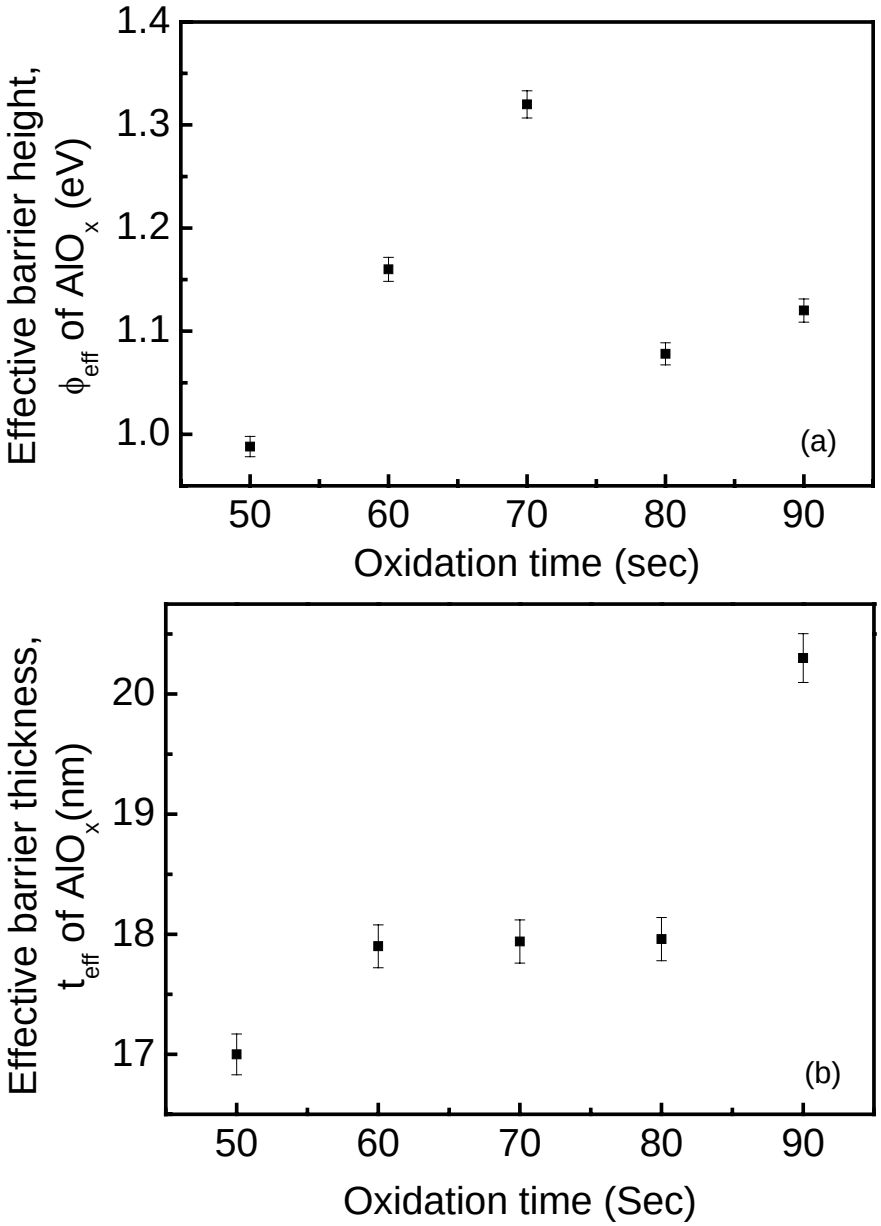

Figure 6.5 Mean effective barrier height (a); and thickness (b) of junctions with tunnel barriers formed with different oxidation time.

Figure 6.5 gives the dependence of the t_{eff} and ϕ_{eff} of MTJs on the oxidation time. The ϕ_{eff} dependence on the oxidation time shown in Fig. 6.5 (a) indicates a maximum value for 70 s oxidation time and decreases for either longer or shorter oxidation time, which may be related to either over oxidation of the bottom electrode or partial Al thin film left after the oxidation. The value of t_{eff} increases generally with oxidation time, similar with the trend of increasing of junction resistance, as shown in Fig. 6.2. From the results above for this set of junctions, we found that the maximum TMR occurs where the tunnel barrier was formed by a 70 s oxidation time. The higher TMR ratio for junction with 70 s oxidation time may be due to the higher barrier height, as predicted by theoretical work.[12]

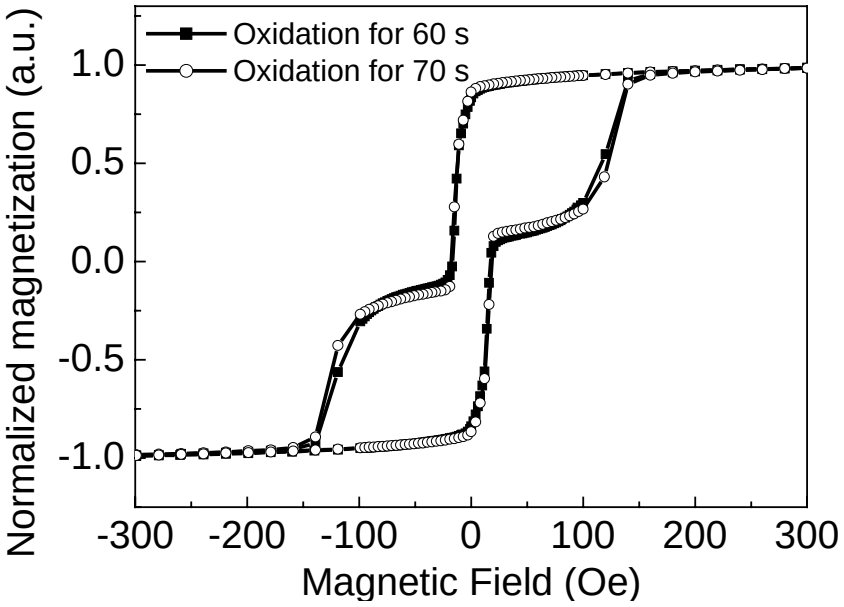

Figure 6.6 Hysteresis loops of junctions with barrier formed by 60 s and 70 s oxidation.

The M-H loop of the reference samples with size of 10 x 10 mm for 60 s and 70 s oxidation MTJs were shown in Fig. 6.6, respectively. It is clear that the hysteresis loops of these two samples almost have the same switching characteristics. When a positive external magnetic field is applied to the sample during the measurement, both $Ni_{80}Fe_{20}$

and Co thin films are saturated if the field is strong enough. The magnetization directions in the two FM layers are consequently parallel to each other. From the saturated state the field is decreased, then increased in the opposite direction. When the field amplitude reaches about –15 Oe, the coercivity of the $Ni_{80}Fe_{20}$ is observed as a kink in the hysteresis loop. The formation of the kink in the hysteresis loop suggests an antiparallel alignment of the magnetization directions in two FM layers. When the magnetic field amplitude reaches about –120 Oe (corresponding to the coercivity of Co thin film), the magnetization directions of the two FM layers become parallel again.

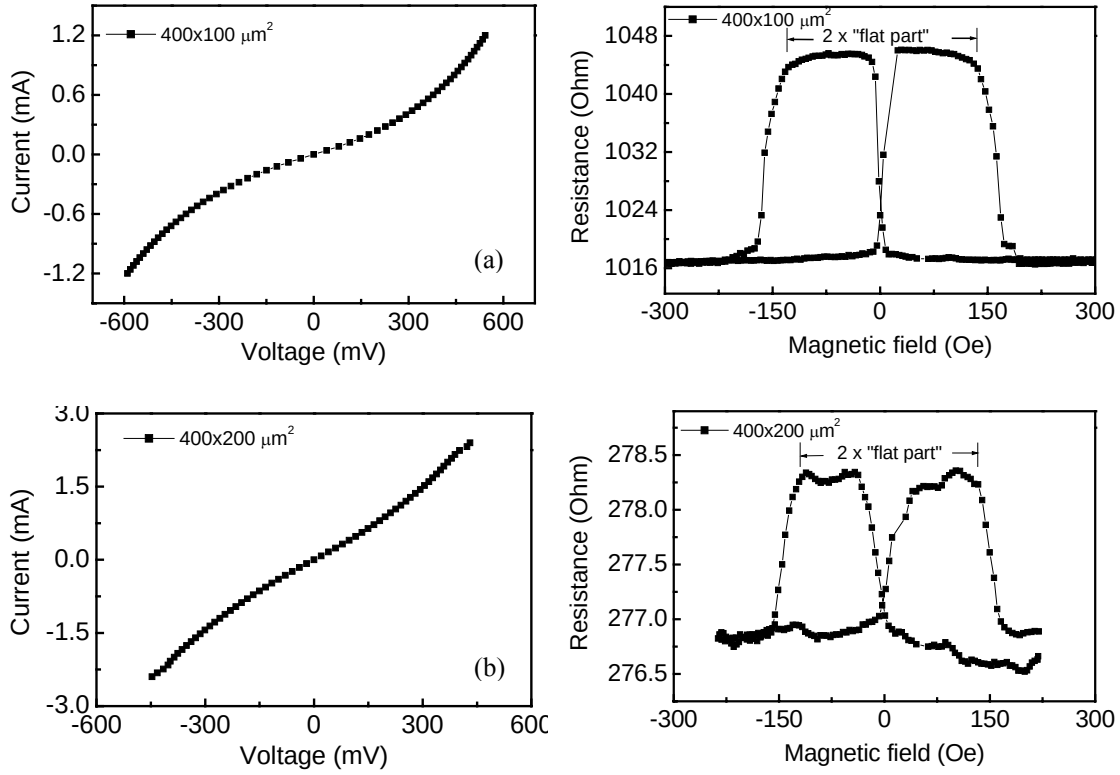

Figure 6.7 I-V curves and TMR curves for junctions with barrier formed by 70 s oxidation: with junction size of (a) 400 x 100 μm^2; and (b) 400 x 200 μm^2.

Figure 6.7 and Fig. 6.8 give the TMR measurement results and I-V curves for junctions of $Ni_{80}Fe_{20}/AlO_x/Co$ with tunnel barrier formed by the two-step plasma oxidation method for 70 s and 60 s, respectively. From the curve we can see two stable and well-defined

resistance states as the applied magnetic field was varied. This indicates an independent magnetic switching of the top and the bottom FM layers, which is consistent with the VSM measurement results.

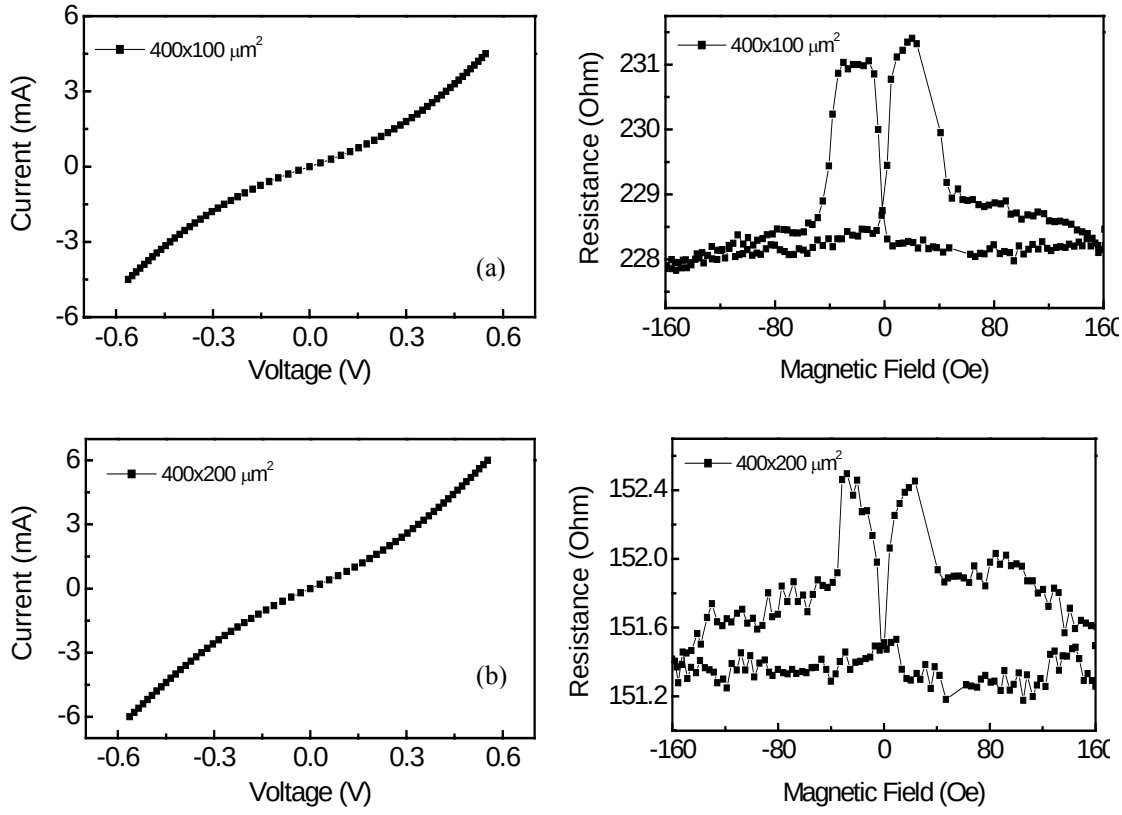

Figure 6.8 I-V curves and TMR curves for junctions with barrier formed by 60 s oxidation: with junction size of (a) 400 x 100 μm^2; and (b) 400 x 200 μm^2.

.

The TMR ratio is around 3% for both sets of MTJs. The flat part in the TMR curves is as defined in Fig. 6.7. When we compare the width of the flat part in Fig. 6.7 and Fig. 6.8, we find that the flatness width of the 70 s oxidation MTJs is about 170 Oe, which is wider than that of the 60 s oxidation MTJs (about 60 Oe). That means that the coercivities of the top Co layer are different in these two cases, which is totally different from the magnetic response of these two sets of MTJs measured by VSM in Fig. 6.6. The possible reason is the AlO_x barrier of 60 s oxidation MTJs is very thin in some spots, which causes the magnetic exchange coupling to the bottom $Ni_{80}Fe_{20}$ electrode. The

absence of magnetic coupling in VSM measurement is probably due to the density of these spots being too small to affect the magnetic response for a large sample size.

6.3.2 The effect of Ar gas pressure

In this part of our work, we will study the effects of the microstructure of as-deposited Al thin film for barrier formation on barrier properties and the TMR performance.

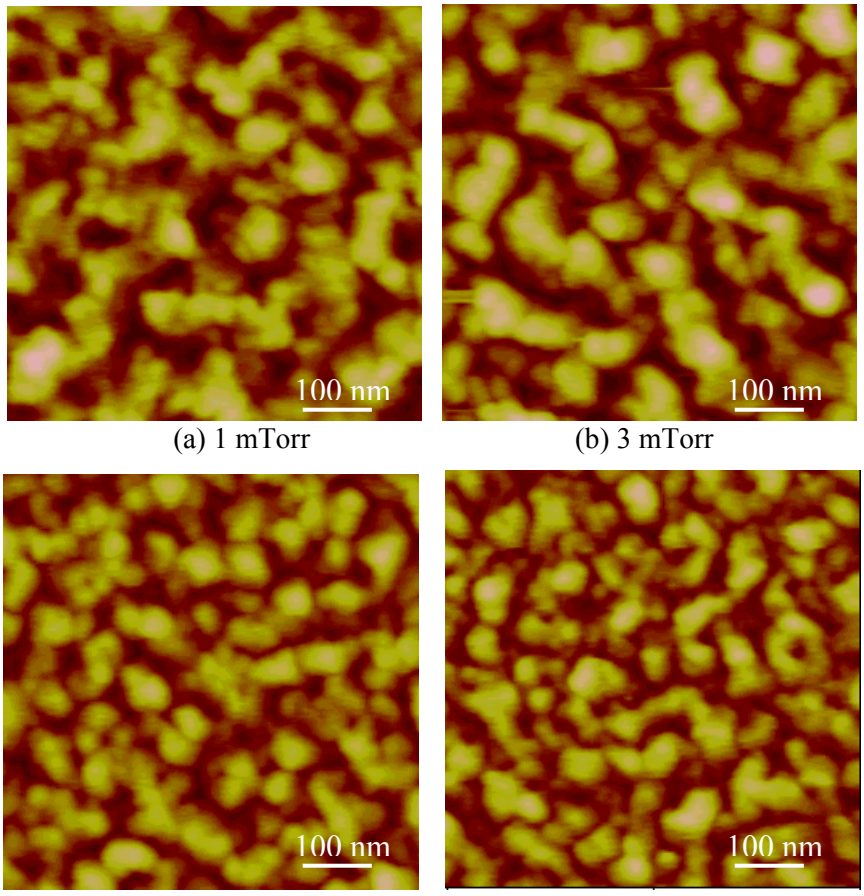

(a) 1 mTorr (b) 3 mTorr

(c) 5 mTorr (d) 8 mTorr

Figure 6.9 Microstructure of Al films deposited under different working gas pressures; (a) 1 mTorr; (b) 3 mTorr; (c) 5 mTorr; and (d) 8 mTorr.

It is well known that the microstructure of thin films depends greatly on the deposition conditions, such as the deposition pressure and the substrate temperature during the

deposition.[11] We studied the microstructure of Al thin films via depositing the metallic Al films under different deposition pressures.

Figure 6.9 gives the AFM images of as deposited Al thin films. It is clear that the grain size of the Al thin films decreases as the working gas pressure increases. One thing we have to keep in mind is that the Al thin film easily oxidized in air; consequently, there is always a thin amorphous AlO_x layer formed to cover the Al thin film below. Therefore, the grain sizes obtained from AFM images are only an indication of the grain size evolution of the Al thin film as a function of deposition gas pressure. The roughness of these Al thin films is about 0.2 nm, which make it possible to fabricate the working MTJs.

MTJs were fabricated with the barrier formed by oxidizing Al thin films which were deposited under different Ar working gas pressures. The detailed deposition conditions for MTJs are listed in Table 6.3. MTJs were obtained for each pressure but we select the 8 mTorr set of samples to perform detail studies and the results were compared to the 3 mTorr set of samples. The reason for choosing 8 mTorr set of samples is that the TMR ratio of this set of samples is comparable to that of the 3 mTorr samples, while the junction resistance is quite small when compared with that of 3 mTorr samples.

Figure 6.10 gives the TMR measurement results and I-V curves for junctions with different sizes. It is clear that all the MTJs show a TMR ratio about 3% and the I-V curves illustrate a nonlinear characteristic. The junction resistance decreases linearly with area as the device size increases. If we look at the junction resistance (R_J) for this set of samples, we find that the value of R_J is far below the value for samples with the barrier formed by oxidation of Al thin film deposited under 3 mTorr working gas pressure, as shown in Fig. 6. 7.

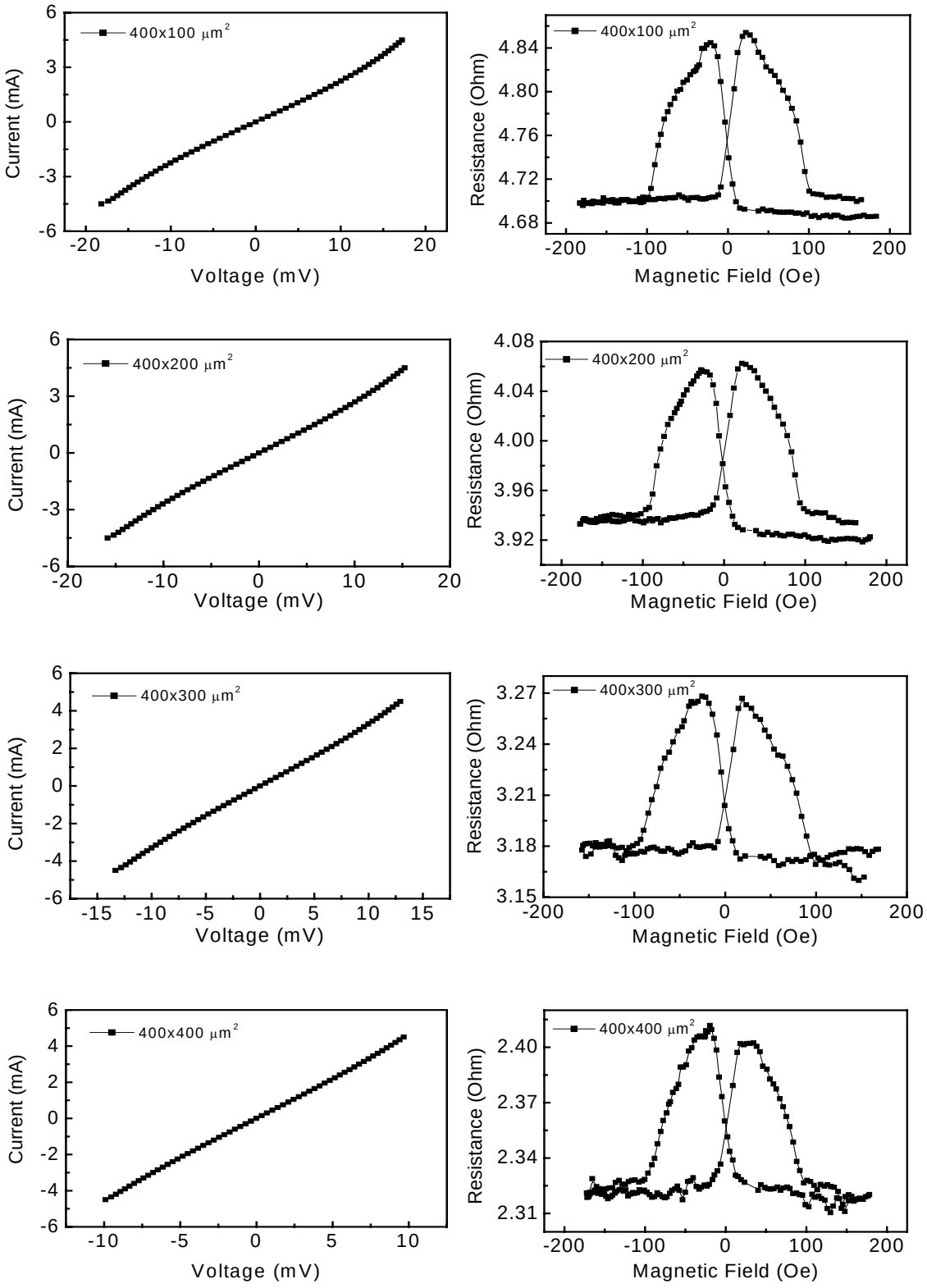

Figure 6.10 I-V curves and TMR curves for junctions with barrier formed by oxidizing Al thin film deposited under 8 mTorr working gas pressure; with junction size of (a) 400 x 100 μm^2; (b) 400 x 200 μm^2; (c) 400 x 300 μm^2; and (d) 400 x 400 μm^2.

The comparison of the mean effective barrier height and the effective junction barrier thickness for Al thin films deposited under 3 mTorr and 8 mTorr Ar working gas pressures are illustrated in Fig. 6.11 (a) and (b).

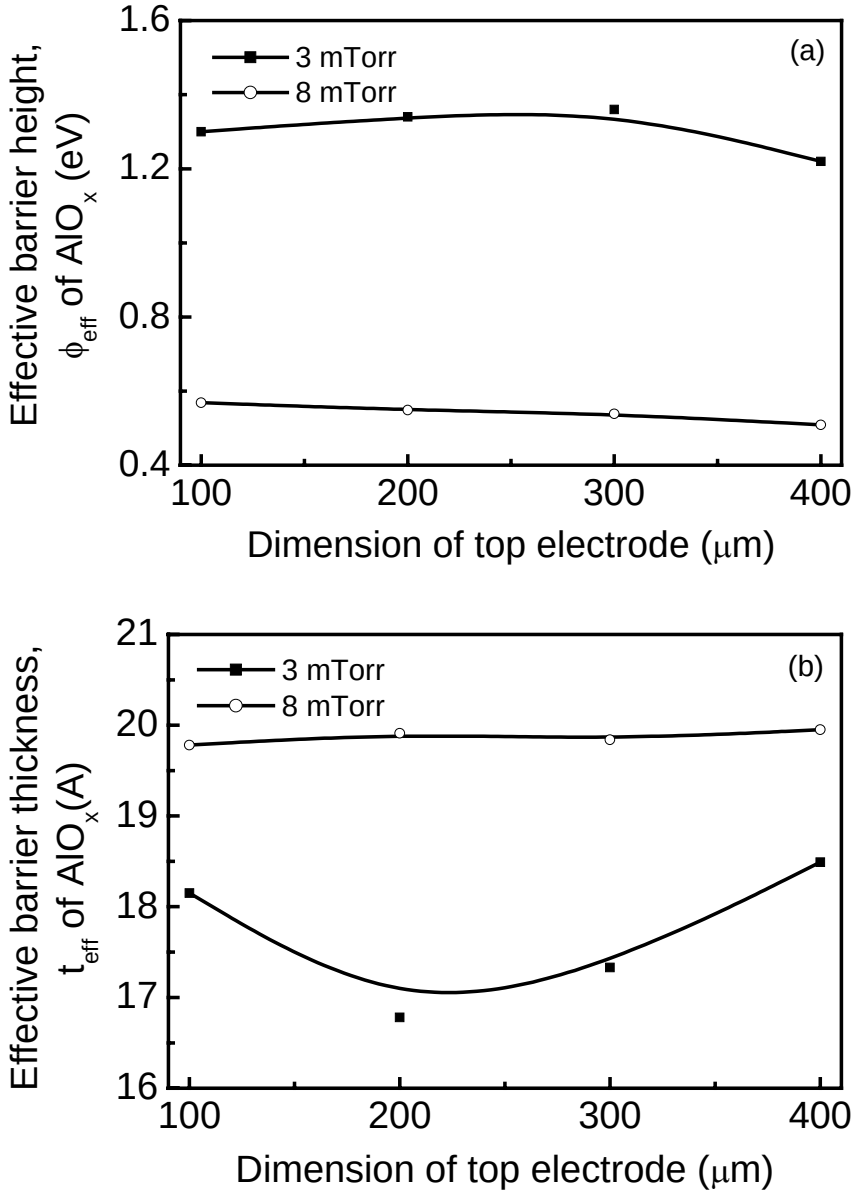

Figure 6.11 Comparison of mean effective barrier height (a); and thickness (b) between junctions with barrier formed by oxidizing Al thin film under different working gas pressures.

It is clear that junctions formed with Al deposited at 8 mTorr working gas pressure have a relative lower effective barrier height and higher effective barrier thickness. The low

barrier height is consistent with the lower junction resistance in this set of samples. Comparisons of junctions with different top electrode dimensions show that the effective barrier parameters for either two sets of samples do not vary much. This data suggests that the uniformity of the tunnel barriers is good.

The oxidation conditions used for barrier formation for the 8 mTorr samples are the same as that for 3 mTorr samples. The plasma oxidation efficiency may not be the same for the Al thin films deposited under different gas pressures. However, the TMR ratio of both 8 mTorr and 3 mTorr samples is around 3%, while the junction resistance of 8 mTorr sample decreases dramatically. This suggests that the junction resistance can be tuned via modifying the microstructure of the Al thin film deposited for barrier formation without sacrificing the TMR ratio.

As we mentioned before, MTJs with low junction resistance is required for applications, such as MRAM and the magnetic read head. Normally, there are two ways to achieve this. One is to decrease the barrier thickness and the other is to use the barrier materials with lower barrier height. Our results clearly demonstrate that the barrier properties depend greatly on the as-deposited microstructure of Al thin films before oxidation. A further important consequence of such dependence is that MTJs with low junction resistance can be achieved by controlling the microstructure of the as deposited Al thin films prior to the barrier formation.

Although the TMR ratio of MTJs achieved in our studies is only about 3%, our intentions in this part of work are not to achieve the highest TMR ratio, but to focus on investigating the effect of certain issues such as, oxidation time, microstructure of the metallic Al thin film for barrier formation, on performance of the MTJs.

6.3.3 Co top electrode property dependency upon barrier layer preparation

It is well known that when a thin film is deposited on top of an underlayer the microstructure of the deposited thin film is strongly influenced by the microstructure of the underlayer.

In our studies, the Co top electrode was deposited on top of the tunnel barrier. Thus, the microstructure of the tunnel barrier may influence the grain size of the top Co layer, which in turn affects the magnetic properties of the Co layer and consequently the switching properties of the MTJ stack. In this section, we will discuss the effect of barrier oxidation time and barrier metal deposition gas pressure on the magnetic properties of the Co top electrode.

The switching properties of MTJ stacks for junctions with barrier formed by oxidizing Al thin films with different time (deposited under 3 mTorr) and junctions with barrier formed by oxidation of Al thin films (deposited under different pressures) for 70 s are shown in the figures below. Figure 6.12 (a) presents the normalized M-H loops of MTJs with Al thin film deposited under the same conditions, but for different oxidation times. From the curves we can see that the M-H loops for sample with 80 s oxidation time is slightly different from the other three samples. Figure 6.12 (b) shows the normalized M-H loops for MTJs with Al thin film deposited under different deposition gas pressures.

We find that the M-H loops of 1 mTorr and 3 mTorr samples are similar and the coercivity of the Co top layer for these two samples is about 150 Oe. The portion of the M-H loop of the 8 mTorr sample due to the $Ni_{80}Fe_{20}$ is similar to these two, while the portion due to the Co top layer has a slightly small coercivity (about 120 Oe vs. 150 Oe).

For the 5 mTorr sample, the coercivity of the Co top layer is significantly smaller, only about 40 Oe. The obvious kink in all of M-H loops suggests that a well-formed tunnel barrier separates the two magnetic electrodes.

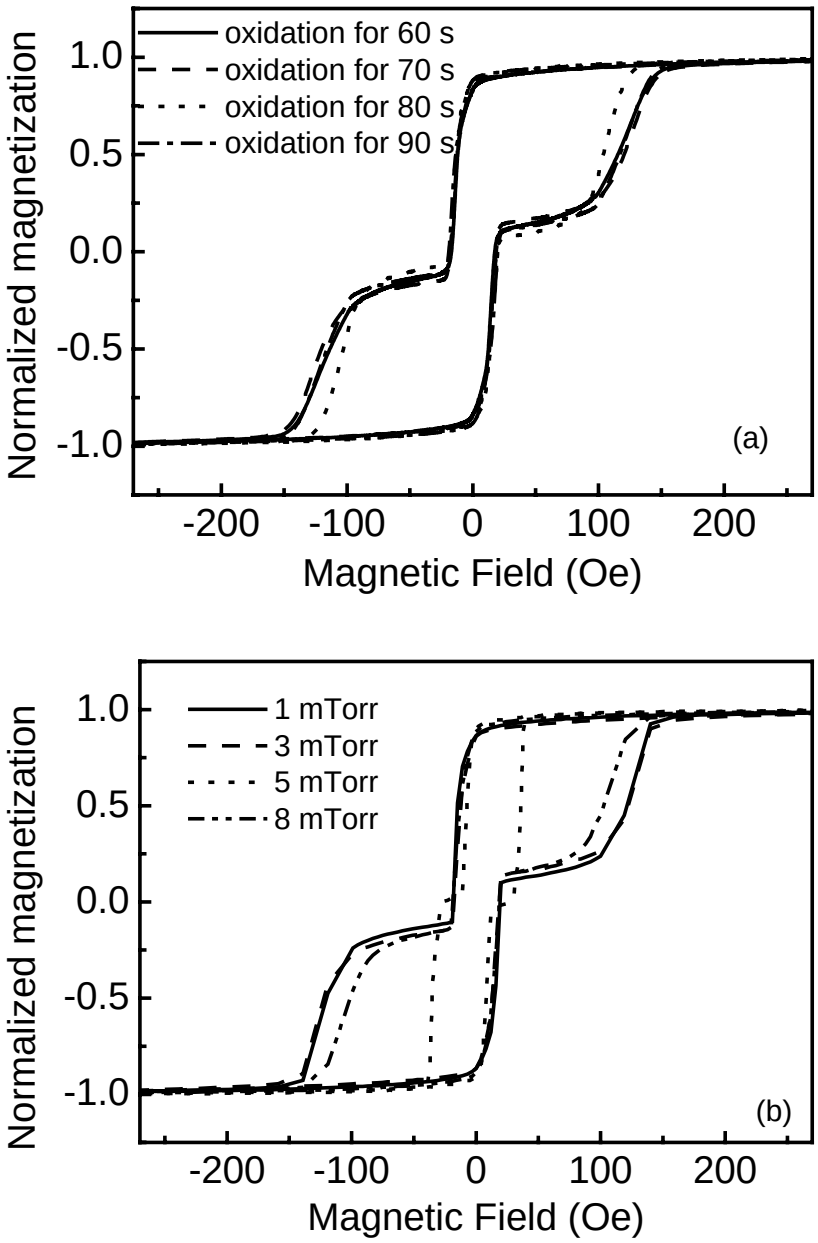

Figure 6.12 Switching properties of junctions with barrier formed by (a) oxidizing Al thin film with different time; (b) oxidizing Al thin film (deposited under different pressures).

Obviously, the switching properties of MTJ stacks vary both due to the oxidation time and the Al thin film deposition pressure. However, clearly the effect of the deposition pressure is most dramatic at 5 mTorr. The data suggests that the magnetic properties of the Co top electrode depend on the microstructure of Al barrier layer thin film.

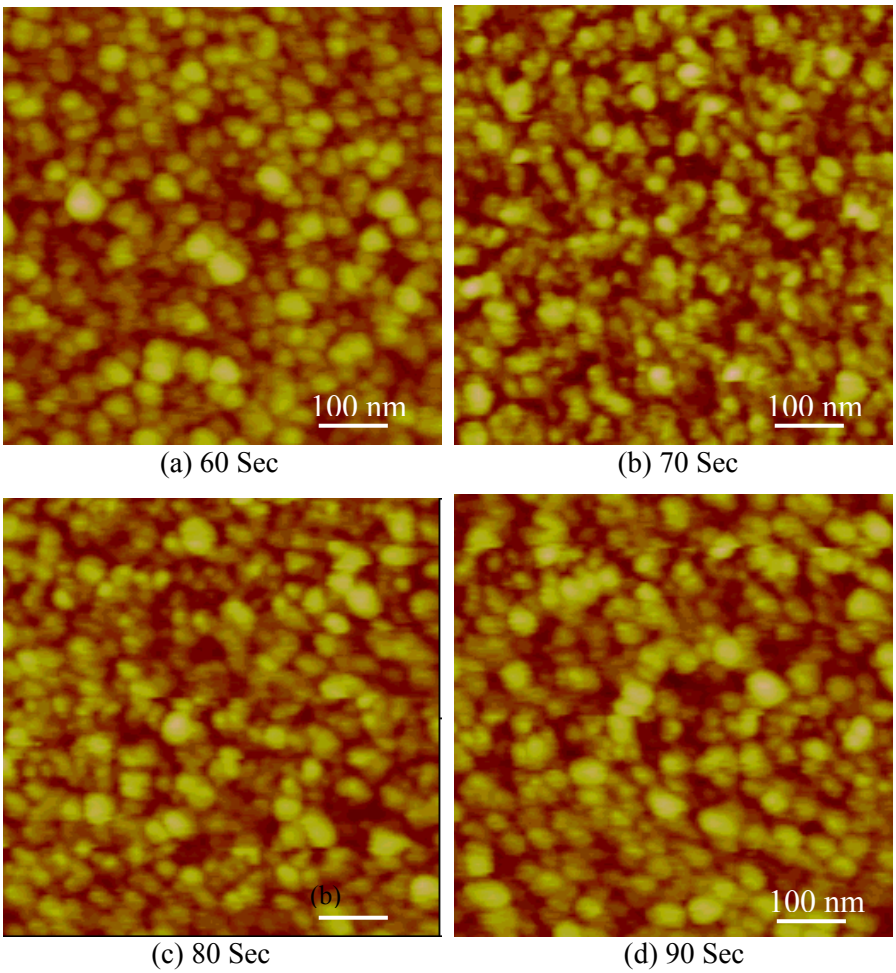

(a) 60 Sec (b) 70 Sec

(c) 80 Sec (d) 90 Sec

Figure 6.13 AFM images of Co film for junctions with barrier formed by oxidizing Al thin films for different time: (a) 60 Sec; (b) 70 Sec; (c) 80 Sec; and (d) 90 Sec.

The evolution of the grain size of the Co top electrodes for these two sets of samples is shown by AFM in Fig. 6.13 and Fig. 6.14. Unlike the small changes of grain sizes of Co thin film in the case of samples with barrier formed by oxidizing for different times (Fig. 6.13), an obvious variation of grain sizes of Co thin film is observed in the case of

samples with barrier formed by oxidizing Al thin films deposited under different pressures (Fig. 6.14). The grain size of Co thin films shows a minimum value in the case of Al thin film deposited under a 5 mTorr working gas pressure. Corresponding to the small grain size of Co thin film, the switching field for this sample also decreases to 40 Oe, which is far below the average value of the switching field (over 100 Oe) for the rest of the samples.

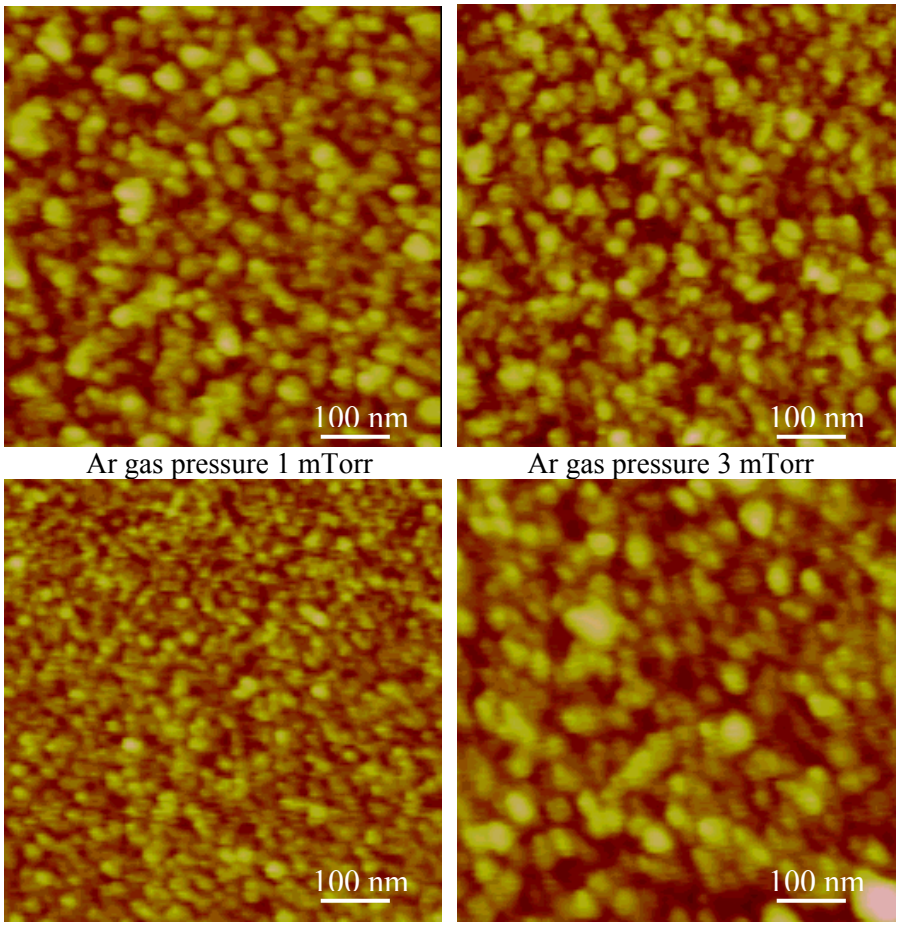

Ar gas pressure 1 mTorr | Ar gas pressure 3 mTorr

Ar gas pressure 5 mTorr | Ar gas pressure 8 mTorr

Figure 6.14 AFM images of Co film for junctions with barrier formed by oxidizing Al thin films deposited under different Ar pressures; (a) 1 mTorr; (b) 3 mTorr; (c) 5 mTorr; and (d) 8 mTorr.

This decrease can be explained as follows. The magnetization is reversed by first nucleating a domain, followed by the rotation of the magnetic spins at the boundary of that domain, which can then be moved through the whole film. If we assume the

magnetocrystalline anisotropy of the film is a constant, films with small grains are easier to be reversed by nucleation. It is known that the grain boundaries in magnetic thin films are effective pinning sites. If the grain size is reduced, the coercivity increases due to the larger number of pinning sites. However, when the grain size becomes smaller or comparable to the width of the domain wall, the grain boundaries become less effective as pinning sites; a further decrease in grain size results in a relative smaller coercivity. It is known that the domain wall width of Co thin film is about tens nanometer, which is larger than the grain size of Co in our studies. Therefore, the decrease of the grain size will result in the reduction of the coercivity. It seems that the grain size of Co thin film depends greatly on the grain size of as deposited Al thin film before oxidation. The oxidation time does not change the grain size of Co top electrode too much.

6.4 Summary

On the basis of rf bias creating a smooth surface of the bottom electrode, we investigated the oxidation conditions for barrier formation in MTJs by using a shadow mask technique. A two-step plasma oxidation was used in our studies. The time for oxidizing the first 9 Å Al thin film was changed from 20 to 60 sec, while the oxidation time for the following 6 Å Al thin film was fixed to be 30 sec. The effects of oxidation time on barrier properties and the performance of MTJs have been studied. The maximum value of the effective barrier height and the maximum TMR occurred where the tunnel barrier was formed by a 70 s oxidation time. The higher TMR for the junction with 70 s oxidation time may be due to the better barrier quality (higher barrier height) compared to others.

We also illustrated that the microstructure of the tunnel barrier depended on the microstructure of the as-deposited Al barrier thin film for barrier formation. The microstructure of tunnel barrier in turn affected the mean effective barrier parameters, as well as the grain size of the Co top layer. The variation of the grain size of the Co top layer will change the coercivity of Co thin film and thus its magnetic switching properties. Various working gas pressures were used to control the microstructure of the as-deposited Al thin films. TMR ratio, junction resistance and the mean effective barrier parameters were evaluated for MTJs with tunnel barrier formed by oxidizing Al thin films deposited under different working gas pressures. Our results demonstrated that the junction resistance and the mean effective barrier parameters of MTJs could be tuned without sacrificing the TMR ratio by controlling the microstructure of the tunnel barrier.

Based on the investigations of the switching properties of the MTJs stacks, it was also found that the microstructure of the formed tunnel barrier affected the grain size and the magnetic properties of the Co thin films growth on top. The grain size of Co thin film depends greatly on the grain size of as deposited Al thin film (deposited under different Ar pressures) before oxidation. The oxidation time does not change the grain size of Co top electrode too much.

Our results clearly demonstrated that the barrier properties depend greatly on the as deposited microstructure of Al thin films before oxidation. Furthermore, our results suggested that the MTJs with lower junction resistance could be achieved by controlling the microstructure of the as deposited Al thin films for barrier formation.

Although the working MTJs were obtained, the TMR ratio of the MTJs is low in our study. The reasons for the low TMR ratio in our study probably due to:

- the limitation of the fabrication equipment. The vacuum break is needed to change the shadow masks, the exposure of the bottom FM layer to air before depositing the barrier layer may cause the oxidation of the bottom FM layer, which results in the decrease of the spin polarization and the status of the interface between the bottom FM layer and the tunnel barrier. The MTJ is very sensitive to the status of the interfaces between the ferromagnetic layer and the tunnel barrier, thus may cause the decrease of the TMR ratio
- the contamination of the bottom FM layer during the mask changing process, which may cause the short-circuit between two FM layers due to the non-uniform coverage of the bottom FM layer by the tunnel barrier
- the shadowing effect caused by the thickness of the mask, which may cause the thickness of the tunnel barrier to be thinner at the edge area of the effective MTJ element. Therefore, the non-uniform current distribution occurred during the measurement, which may cause the deterioration of the TMR ratio in MTJs
- the magnetron sputter system used in our study has only one vacuum chamber, depositing the FM layers and performing plasma oxidation in the same chamber may affect the magnetic properties of the FM layers
- there is no applied magnetic field during the deposition of the FM layers to induce a uniaxial anisotropy in the films

In order to find out the reasons of the low TMR ratio in our work, we give the comparisons of our work to other research groups, where the metal shadow mask technique was used to fabricate the MTJs and the Al layer thickness for barrier formation is around 15 Å. The comparisons are carried out by focusing on the base pressure of the

vacuum system been used, TMR ratio obtained and the detailed fabrication processes. Following issues were considered such as, are there any vacuum breaks during the mask changing process? Whether the easy axis of the FM layer is controlled by applying a magnetic field during the deposition or using suitable underlayer to promote the favorable crystalline orientation? Is there a separated vacuum chamber for barrier formation? The comparison results are given at the table 6.4 below.

Table 6.4 Comparison of our results with other research groups

Parameters / Groups	Base pressure (Torr)	Vacuum break	FM layer easy axis control	MTJ structure	TMR ratio (%)
Moodera et al[13]	10^{-7}	No	No	$CoFe/Al_2O_3/Co$	11.8%
Parkin et al[14]	1×10^{-9}	unknown	Yes	$CrV/CoCrPt/Al_2O_3/Co$	13%
Hughes et al.[15]	1×10^{-7}	No	No	$Co/AlO_x/Ni_{81}Fe_{19}$	12.9%
B. You et al.[16]	8×10^{-8}	unknown	Yes	$CoFe/AlO_x/Co$	6.5 ~ 8.5%
D. M. Jeon[17]	6×10^{-7}	Yes	Yes	$Cr/Co/AlO_x/Co/Ni_{80}Fe_{20}$	7.4%
Our work	4×10^{-7}	Yes	No	$NiFe/AlO_x/Co$	3%

It can be found that the TMR ratio is over 10% when there is no vacuum break during the mask changing processes. In addition, applied a magnetic field during the deposition of the FM layer is also favorable to obtain the higher TMR ratio. The experimental conditions of D. M. Jeon's group and our group is comparable, whereas the TMR ratio obtained in their group is about 7.4%, higher than 3% in our study. One reason maybe the easy axis of the FM layer was controlled by using Cr underlayer in their study. Another reason was the tunnel barrier and the bottom FM layer were formed using the same shadow mask, therefore, the formed tunnel barrier can protect the bottom FM layer to be oxidized during the mask changing process.

[1] Z. G. Zhang, P. P. Freitas, A. R. Ramos, N. P. Barradas, and J. C. Soares, *J. Appl. Phys.* **91**, 8786 (2002).

[2] K. S. Moon, Y. J. Chen, and Y. M. Huai, *J. Appl. Phys.* **91**, 7965 (2002).

[3] Z. G. Zhang, P. P. Freitas, A. R. Ramos, N. P. Barradas, and J. C. Soares, *Appl. Phys. Lett.* **79**, 2219 (2001).

[4] K. S. Yoon, J. H. Park, J. H. Choi, J. Y. Yang, C. H. Lee, C. O. Kim, J. P. Hong, and T. W. Kang, *Appl. Phys. Lett.* **79**, 1160 (2001).

[5] U. May, K. Samm, H. Kittur, J. Hauch, R. Calarco, U. Rudiger and G. Guntherodt, *Appl. Phys. Lett.* **78**, 2026 (2001).

[6] P. Rottländer, H. Kohlstedt, P. Grünberg, and E. Girgis, *J. Appl. Phys.* **87**, 6067 (2000).

[7] H. Boeve, J. De Boeck, and G. Borghs, *J. Appl. Phys.* **89**, 482 (2001).

[8] K. Matsuda, A. Kamijo, T. Mitsuzuka, and H. Tsuge, *J. Appl. Phys.* **85**, 5261 (1999).

[9] E. Y. Chen, R. Whig, J. M. Slaughter, J. Goggin, G. Steiner, and S. Tehrani, *J. Appl. Phys.* **87**, 6061 (2000).

[10] C. H. Shang, J. Nowak, R. Jansen, and J. S. Moodera, *Phys. Rev. B* **58**, R2917 (1998).

[11] J. C. Simmons, *J. Appl. Phys.* **34**, 2581 (1963).

[12] J. C. Slonczewski, *Phys. Rev. B* **39**, 6995 (1989).

[13] J. S. Moodera, L. R. Kinder, T. M. Wong and R. Meservey, Phys. Rev. Lett., 74, 3273 (1995).

[14] S. S. P. Parkin, K. –S. Moon, K. E. Pettit, D. J. Smith, R. E. Dunin-Borkowski and M. R. McCartney, Appl. Phys. Lett., 75, 543 (1999).

[15] N. D. Hughes and R. J. Hicken, J. Phys. D 35, 3153 (2002).

[16] B. You, W. T. Sheng, L. Sun, W. Zhang, J. Du, M. Lu, H. R. Zhai, A. Hu, Q. Y. Xu, Y. G. Wang and Z. Zhang, J. Phys. D 36, 2313 (2003).

[17] D. M. Jeon, J. W. Park, Y. S. Kim, D. H. Yoon and S. J. Suh, Thin Solid Films 435, 135 (2003).

Chapter 7

Conclusions and Future works

7.1 Conclusions

In this dissertation, the spin-dependent tunneling (STD) phenomenon in magnetic tunnel junction (MTJ) elements was investigated theoretically and experimentally.

Based on the free-electron model, simulation works were carried out in a structure of ferromagnet/insulator/ferromagnet (FM/I/FM) tunnel junction with nonmagnetic (NM) metal layer on both sides. The TMR and the exchange coupling as the function of several parameters such as, the thickness of the tunnel barrier, the thickness of the FM layers, the spin polarization of two FM layers, the Fermi wavevectors of two FM layers and the interfacial roughness, were investigated theoretically.

For MTJ stacks with finite thickness of two FM layers, both TMR and the exchange coupling oscillated periodically with the thickness of ferromagnetic layer. The TMR and the exchange coupling were correlated to each other and the maximum TMR occurred when ferromagnetic exchange coupling between two ferromagnetic layers reached the maximum value.

Compared with the structure with perfect interface roughness, both the amplitude and the oscillation period of the TMR and the exchange coupling were changed with the introduction of the interfacial roughness. The TMR ratio decreased and the exchange coupling increased after the interfacial roughness was introduced. The decrease of the TMR with a rough FM layer was attributed to the decrease of spin polarization of FM

layers, which resulted from the spin scattering induced decay of the distribution asymmetry of density of states in FM layers. The increase of the exchange coupling may be attributed to the interfacial roughness induced exchange coupling between two FM layers via the insulator spacer. The difference of the oscillation period of the TMR and the exchange coupling was due to the variation of the Fermi wave vectors induced by the interfacial scattering of the electrons.

As the surface roughness of the bottom FM layer is a critical issue in fabrication of MTJs, this was further investigated experimentally. Our results illustrated that the surface roughness of the bottom $Ni_{80}Fe_{20}$ thin films were weakly dependent on the dc sputter power and the film thickness, however, it could be modified by introducing different strength of rf substrate bias during the deposition. The values of the surface roughness of the $Ni_{80}Fe_{20}$ thin films varied from 0.197 nm to 1.697 nm, the smoothest surface of $Ni_{80}Fe_{20}$ thin film (0.197 nm) was achieved when a 20 W rf bias was applied to the substrate during the deposition. The surface roughness of $Ni_{80}Fe_{20}$ bottom layer also affected the properties of the magnetic Co layer and the MTJ stacks deposited on top of it. The coercivity of the Co top layer changed from the 24 to 15 Oe as the surface roughness of $Ni_{80}Fe_{20}$ bottom layer becomes smoother. Compared to the hysteresis loop of the deposited MTJ stacks without the $Ni_{80}Fe_{20}$ bottom layer, the switching properties of MTJ stacks demonstrated a well-formed kink for the MTJ stacks deposited on top of a smooth $Ni_{80}Fe_{20}$ bottom layer.

Based on the smooth bottom surface roughness achieved and the experimental conditions used for MTJ stacks fabrication, MTJs were fabricated by using a shadow mask technique. The characteristics of MTJs and the barrier properties as a function of

the oxidation time and the microstructure of the metallic Al thin film for barrier formation were investigated, respectively. A two-step plasma oxidation method was used for barrier formation.

The microstructure of Al thin film in our studies was controlled by varying the working gas pressures in the deposition. A set of MTJs was fabricated, in which the tunnel barriers were formed by oxidizing the Al thin films with different microstructure. Comparison of results among these MTJs showed that the low junction resistance MTJs could be achieved by controlling the microstructure of the as-deposited Al thin film for barrier formation. Our results also showed that the effective barrier parameters, the microstructure of the top Co thin film and the switching properties of MTJ devices depended on the oxidation time and the microstructure of Al thin film for barrier formation.

Our results clearly demonstrated that the barrier properties depend greatly on the as deposited microstructure of Al thin films before oxidation. Furthermore, our results suggested that the MTJs with lower junction resistance could be achieved by controlling the microstructure of the as deposited Al thin films for barrier formation.

7.2 Future works

In experimental works, we only concentrated on investigating the dependence of the surface roughness of the bottom FM layer on experimental conditions and its influences on the magnetic properties of thin films and the switching properties of MTJ stacks deposited on top of it. The interlayer effect was not investigated in this dissertation. In the future works, MTJ elements with an interlayer inserted between the FM layer and the

insulator layer can be fabricated and the effects of the interlayer on the performance of the MTJ elements can be studied.

There are some challenges involved in the applications of the MTJ elements. One of the challenges is producing MTJ elements with very low *RA*. As the reduction of the bit sizes, MRAM may require MTJ elements with lower *RA*. In addition, use in hard-disk read heads would also require a much lower resistance. Our results showed that the MTJs with lower junction resistance could be achieved by controlling the microstructure of the metallic Al thin film for barrier formation. Further works still need to be done in the future for application purpose.

List of publications

The research work related to this dissertation has been reported in the following publications.

Journal papers

1. V. Ng, J. F. Hu, A. O. Adeyeye, J. P. Wang and T. C. Chong, "Factors affecting surface roughness and coercivity of $Ni_{80}Fe_{20}$ thin films". *J. Appl. Phys.* 91, 7206 (2002).
2. V. Ng, J. F. Hu, A. O. Adeyeye, J. P. Wang and T. C. Chong, "Radio frequency substrate bias effect on properties of Co thin film and multilayer structures". *J. Magn. Magn. Mater.* 247, 339 (2002).
3. J. F. Hu, V. Ng, J. P. Wang and T. C. Chong, "The effect of interlayers on magnetoresistance and exchange coupling in magnetic tunnel junctions". *J. Magn. Magn. Mater*. 268, 114 (2004).

Conference paper

1. "Factors affecting surface roughness and coercivity of $Ni_{80}Fe_{20}$ thin films". V. Ng, J. F. Hu, A. O. Adeyeye, J. P. Wang and T. C. Chong, *46^{th} Annual conference on Magnetism & Magnetic Materials*. Seatlle, Washington, 2001.

Appendix I

Program for calculation of the TMR and the exchange coupling

Main Program for TMR calculation

```
clear all;
E=0.34;U0=1.2;V1=0;V2=0;
ha=0.20;hb=0.20;
k1=sqrt(2*E);
k2up1=sqrt(2*(E-V1+ha));
k2down1=sqrt(2*(E-V1-ha));
r_p1=sqrt(2*(U0-E));
k4up1=sqrt(2*(E-V2+hb));
k4down1=sqrt(2*(E-V2-hb));
SP=[(k2up1-k2down1)*(r_p1^2-
k2up1*k2down1)]/[(k2up1+k2down1)*(r_p1^2+k2up1*k2down1)];
sp=(k2up1-k2down1)^2/(2*k2up1*k2down1);
N1=100;
for i=1:N1+1
   aa(i)=8+45*(i-1)/N1;
end
b = 20;
N2 = 2;
for ii = 1: length(aa)
   c = aa(ii);
   a = c;
   for i = 1:N2+1
      tt(i) = (i-1)*pi/N2;
   end
   T1 = [];   T2 = [];
   T=[]; G = [];  TMR = [];
   e1=1;
   h_constant=1;

   for i = 1:length(tt)
       T1(i)=Tp710(a,b,c,k2up1,k2down1,k4up1,k4down1,k1,r_p1,tt(i));
       T2(i)=Tp710(a,b,c,k2down1,k2up1,k4down1,k4up1,k1,r_p1,tt(i));
       T(i)=T1(i)+T2(i);
       G(i)=(e1^2/(8*(pi^2)*h_constant))*(r_p1/b)*T(i);
       if G(1)==0
          disp('error, divided by zero!');
          return
       end
       TMR(i) = (G(1)-G(i))/G(1);
   end
   TMR0_180(ii) =  (G(1)-G(length(G)))/G(1);
end
%subplot(2,1,1), plot(tt, G);
%subplot(2,1,2), plot(tt, TMR);
%figure(1), plot(tt, G);
%figure(2), plot(tt, TMR);
%figure(1), plot(pre, TMR0_180);
figure(3), plot(aa, TMR0_180);
```

Sub program Tp710

```
function T = Tp710(a,b,c,k20,k21,k40,k41,k,r_p,theta)

syms  p1 p2 x1 p3 p4 x2

temp1=cos(theta/2);
temp2=sin(theta/2);

A1=[...
1 0 -1 -1 0 0 0 0 0 0 0 0 0 0 0 0
0 -1 0 0 1 1 0 0 0 0 0 0 0 0 0 0
0 0 1 exp(-2*i*k20*a) 0 0 -exp(-i*k20*a) -exp(-i*k20*a) 0 0 0 0 0 0 0 0
0 0 0 0 1 exp(-2*i*k21*a) 0 0 -exp(-i*k21*a) -exp(-i*k21*a) 0 0 0 0 0 0
0 0 0 0 0 0 exp(-2*r_p*b) 1 0 0 -exp(-r_p*b)*temp1 -exp(-r_p*b)*temp1 -
exp(-r_p*b)*temp2 -exp(-r_p*b)*temp2 0 0
0 0 0 0 0 0 0 0 exp(-2*r_p*b) 1 exp(-r_p*b)*temp2 exp(-r_p*b)*temp2 -
exp(-r_p*b)*temp1 -exp(-r_p*b)*temp1 0 0
0 0 0 0 0 0 0 0 0 0 1 exp(-2*i*k40*c) 0 0 -exp(-i*k40*c) 0
0 0 0 0 0 0 0 0 0 0 0 0 1 exp(-2*i*k41*c) 0 -exp(-i*k41*c)
k 0 k20 -k20 0 0 0 0 0 0 0 0 0 0 0 0
0 k 0 0 k21 -k21 0 0 0 0 0 0 0 0 0 0
0 0 k20 -k20*exp(-2*i*k20*a) 0 0 -i*r_p*exp(-i*k20*a) i*r_p*exp(-
i*k20*a) 0 0 0 0 0 0 0 0
0 0 0 0 k21 -k21*exp(-2*i*k21*a) 0 0 -i*r_p*exp(-i*k21*a) i*r_p*exp(-
i*k21*a) 0 0 0 0 0 0
0 0 0 0 0 0 -r_p*exp(-2*r_p*b) r_p 0 0 -i*k40*temp1*exp(-r_p*b)
i*k40*temp1*exp(-r_p*b) -i*k41*temp2*exp(-r_p*b) i*k41*temp2*exp(-
r_p*b) 0 0
0 0 0 0 0 0 0 0 -r_p*exp(-2*r_p*b) r_p i*k40*temp2*exp(-r_p*b) -
i*k40*temp2*exp(-r_p*b) -i*k41*temp1*exp(-r_p*b) i*k41*temp1*exp(-
r_p*b) 0 0
0 0 0 0 0 0 0 0 0 0 -k40 k40*exp(-2*i*k40*c) 0 0 k*exp(-i*k40*c) 0
0 0 0 0 0 0 0 0 0 0 0 0 -k41 k41*exp(-2*i*k41*c) 0 k*exp(-i*k41*c)];

E1=[-1/sqrt(k) 0 0 0 0 0 0 0 sqrt(k) 0 0 0 0 0 0 0];

F1=E1';
X1=inv(A1)*F1;
wave_f1 = p1*exp(-r_p*x1) + p2*exp(r_p*x1);
f1=diff(wave_f1,x1);
tp1=(conj(wave_f1))*f1;
p1=X1(7);
p2=X1(8);
x1=a;
Tp1=subs(tp1);
T=-1/2*i*(Tp1-conj(Tp1));
```

Main Program for the exchange coupling calculation

```
clear all;
E=0.34;U0=1.2;V1=0;V2=0;
ha=0.25;hb=0.25;
k1=sqrt(2*E);
k2up1=sqrt(2*(E-V1+ha));
k2down1=sqrt(2*(E-V1-ha));
r_p1=sqrt(2*(U0-E));
k4up1=sqrt(2*(E-V2+hb));
k4down1=sqrt(2*(E-V2-hb));
N1=100;
for i=1:N1+1
   aa(i)=8+45*(i-1)/N1;
end
b = 15;
theta = pi;
b20 = [];
b21 = [];
b2=[];
J2=[];
for ii = 1: length(aa)
c = aa(ii);
a = c;
b20(ii)=Tp_coupling(a,b,c,k2up1,k2down1,k4up1,k4down1,k1,r_p1,theta);

b21(ii)=Tp_coupling(a,b,c,k2down1,k2up1,k4down1,k4up1,k1,r_p1,theta);
b2(ii) = b20(ii)+b21(ii);
J2(ii) = (U0-E)*b2(ii)/(8*pi^2*b^2);
end
figure(3), plot(aa, J2);
```

Sub program Tp_coupling

```
function b2 = Tp_coupling(a,b,c,k20,k21,k40,k41,k,r_p,theta)

syms  p1 p2 x1 p3 p4 x2

temp1=cos(theta/2);
temp2=sin(theta/2);

A1=[...
   1 0 -1 -1 0 0 0 0 0 0 0 0 0 0 0 0
   0 -1 0 0 1 1 0 0 0 0 0 0 0 0 0 0
   0 0 1 exp(-2*i*k20*a) 0 0 -exp(-i*k20*a) -exp(-i*k20*a) 0 0 0 0 0 0
0 0
   0 0 0 0 1 exp(-2*i*k21*a) 0 0 -exp(-i*k21*a) -exp(-i*k21*a) 0 0 0 0
0 0
   0 0 0 0 0 0 exp(-2*r_p*b) 1 0 0 -exp(-r_p*b)*temp1 -exp(-
r_p*b)*temp1 -exp(-r_p*b)*temp2 -exp(-r_p*b)*temp2 0 0
   0 0 0 0 0 0 0 0 exp(-2*r_p*b) 1 exp(-r_p*b)*temp2 exp(-r_p*b)*temp2
-exp(-r_p*b)*temp1 -exp(-r_p*b)*temp1 0 0
   0 0 0 0 0 0 0 0 0 0 1 exp(-2*i*k40*c) 0 0 -exp(-i*k40*c) 0
   0 0 0 0 0 0 0 0 0 0 0 0 1 exp(-2*i*k41*c) 0 -exp(-i*k41*c)
   k 0 k20 -k20 0 0 0 0 0 0 0 0 0 0 0 0
   0 k 0 0 k21 -k21 0 0 0 0 0 0 0 0 0 0
   0 0 k20 -k20*exp(-2*i*k20*a) 0 0 -i*r_p*exp(-i*k20*a) i*r_p*exp(-
i*k20*a) 0 0 0 0 0 0 0 0
   0 0 0 0 k21 -k21*exp(-2*i*k21*a) 0 0 -i*r_p*exp(-i*k21*a)
i*r_p*exp(-i*k21*a) 0 0 0 0 0 0
   0 0 0 0 0 0 -r_p*exp(-2*r_p*b) r_p 0 0 -i*k40*temp1*exp(-r_p*b)
i*k40*temp1*exp(-r_p*b) -i*k41*temp2*exp(-r_p*b) i*k41*temp2*exp(-
r_p*b) 0 0
   0 0 0 0 0 0 0 0 -r_p*exp(-2*r_p*b) r_p i*k40*temp2*exp(-r_p*b) -
i*k40*temp2*exp(-r_p*b) -i*k41*temp1*exp(-r_p*b) i*k41*temp1*exp(-
r_p*b) 0 0
   0 0 0 0 0 0 0 0 0 0 -k40 k40*exp(-2*i*k40*c) 0 0 k*exp(-i*k40*c) 0
   0 0 0 0 0 0 0 0 0 0 0 -k41 k41*exp(-2*i*k41*c) 0 k*exp(-i*k41*c)];

E1=[-1/sqrt(k) 0 0 0 0 0 0 0 sqrt(k) 0 0 0 0 0 0 0];
F1=E1';X1=inv(A1)*F1;
wave_up1=conj(p1)*exp(-r_p*x1)+conj(p2)*exp(r_p*x1);
wave_down0=p3*exp(-r_p*x2)+p4*exp(r_p*x2);
f11=diff(wave_up1,x1);
f21=diff(wave_down0,x2);
p1=X1(7);
p2=X1(8);
p3=X1(9);
p4=X1(10);
x1=a;
x2=a;
f1=subs(f11);
f2=subs(f21);
wave_up11=subs(wave_up1);
wave_down01=subs(wave_down0);
Txy=i*(f1*wave_down01-wave_up11*f2);
b2=1/2*i*(Txy-conj(Txy))/sin(theta);
```

Appedix II

Simmons' Theory

J. G. Simmons derived a formula for the electric tunnel effect through a potential barrier in a normal metal-insulator-normal metal junction. The formula was applied to a rectangular barrier with and without image forces. Assuming an arbitrary shaped potential barrier, the mean barrier height $\bar{\phi}$ and tunneling current were expressed as below:

$$\bar{\phi} = \frac{1}{\Delta s}\int_{s_1}^{s_2} \phi(x)dx \tag{1}$$

$$J = J_0\left\{\bar{\phi}\exp\left(-A\sqrt{\bar{\phi}}\right) - \left(\bar{\phi}+eV\right)\exp\left(-A\left(\bar{\phi}+eV\right)^{1/2}\right)\right\} \tag{2}$$

where $J_0 = \frac{e}{2\pi h(\beta\Delta s)^2}$, $A = \frac{4\pi\beta\,\Delta s}{h}(2m)^{1/2}$; s_1 and s_2 are the limits of barrier at Fermi lever and $\Delta s = s_2 - s_1$. β is a correction factor close to unity. The thickness of the tunnel barrier is s. For convenience of numerical calculations, J is expressed in A/cm^2, ϕ_0 in V, and s, s_1, and s_2 in Å units. For a rectangular barrier with image force induced. For a voltage V less than the value of ϕ_0, the equation (2) could be expressed as,

$$J = \left(6.2\times10^{10}/\Delta s^2\right)\left\{\bar{\phi}\exp\left(-1.025\Delta s\phi_I^{\frac{1}{2}}\right) - \left(\bar{\phi}+V\right)\exp\left(-1.025\Delta s\left(\bar{\phi}+V\right)^{\frac{1}{2}}\right)\right\} \tag{3}$$

$$\bar{\phi} = \phi_0 - (V/2s)(s_1+s_2) - \left[5.75/K(s_2-s_1)\right]\ln\left[s_2(s-s_1)/(s-s_2)\right] \tag{4}$$

where $s_1 = 6/K\phi_0$ and $s_2 = s\left[1-46/(3\phi_0 Ks + 20 - 2VKs)\right] + 6/K\phi_0$

Substitute the barrier thickness s and barrier height ϕ_0 into the equations (3) and (4) together with the measured voltage data, the J can be calculated and compared to the measured tunneling current. The mean effective barrier thickness and effect barrier height can be obtained once the minimal misfit between the calculated and the measured tunneling current is achieved.

Appedix III

Program for I-V curve fitting

```
clear all
close all
clc
K = 2000;
* Input the experimental data

Data1=...
[0 1. 0096E-5
0.08  0.0202
0.16  0.04016
0.24  0.05979
0.32  0.07886
0.4   0.09735
0.48  0.1153
0.56  0.13265
0.64  0.14937
0.72  0.1657
0.8   0.18149
0.88  0.19664
0.96  0.21136
1.04  0.22564
1.12  0.24016
1.2   0.25398
1.28  0.26621
1.36  0.27972
1.44  0.29349
1.52  0.30521
1.6   0.31697
1.68  0.32756
1.76  0.33835
1.84  0.34934
1.92  0.35885
2     0.36937
2.08  0.37979
2.16  0.38931
2.24  0.40209
2.32  0.42235
2.4   0.4308];

* Input the data into two matrix V and j
V = Data1(:,2);
j = Data1(:,1);

* I-V fitting part
N1=100;
N2=100;
for i=1:N1+1
    phi0(i)=0.6 + 1*(i-1)/N1;
   for t=1:N2+1
    s(t)=15 + 5*(t-1)/N2;
s1 = 3/K/phi0(i);
```

```
s2 = s(t)*(1- 23/K/s(t)*(3*phi0(i)+10/K/s(t) - 2.*V))+s1;
temp = (2.86/K./(s2-s1)) .* (log(s2*(s(t)-s1)./(s1*(s(t)-s2))));
phi_av = phi0(i) - (V/2/s(t)) .* (s1 + s2) - temp;
h = s2 - s1;
g = (6.2*10^10)./(h.^2);
j1(:,i) = g.*(phi_av.* exp(-1.025*h.*sqrt(phi_av))-(phi_av+V) .* exp(-
1.025*h.*sqrt(phi_av+V)));

chr_1 = (j-j1(:,i)).^2;
sum1(i,t) = sum(chr_1)/size(j,1);
end
end
[sum1_min1, Index1] = min(sum1,[],1);
[sum1_min, Index2] = min(sum1_min1);
T = Index2;
I = Index1(Index2);

%Replace the optimal value of barrier height and barrier thickness in
to fit the IV curve!
clear phi_av, h;
i = I; t = T;
s1 = 3/K/phi0(i);
s2 = s(t)*(1- 23/K/s(t)*(3*phi0(i)+10/K/s(t) - 2.*V))+s1;
temp = (2.86/K./(s2-s1)) .* (log(s2*(s(t)-s1)./(s1*(s(t)-s2))));
phi_av = phi0(i) - (V/2/s(t)) .* (s1 + s2) - temp;
h = s2 - s1;
g = (6.2*10^10)./(h.^2);
j1 = g.*(phi_av.* exp(-1.025*h.*sqrt(phi_av))-(phi_av+V) .* exp(-
1.025*h.*sqrt(phi_av+V)));

figure; plot(V, j,'r*');
hold;
plot(V, j1,'b+');
phi0 = phi0(I);
sprintf('phi0 = %12.4f eV;',phi0)
s = s(T);
sprintf('s = %12.4f Å',s)
phi_av = phi_av(1);
sprintf('phi_av = %12.4f eV;',phi_av)
h = h(1);
sprintf('h = %12.4f Å',h)
```